Doctoral Dissertations   Graduate School

12-2013

Experimental and Statistical Techniques to Probe Extraordinary Electronic Properties of Molecules

Byron Hager Smith
University of Tennessee - Knoxville, bsmit125@utk.edu

Follow this and additional works at: https://trace.tennessee.edu/utk_graddiss

Part of the Applied Statistics Commons, and the Biological and Chemical Physics Commons

To the Graduate Council:

I am submitting herewith a dissertation written by Byron Hager Smith entitled "Experimental and Statistical Techniques to Probe Extraordinary Electronic Properties of Molecules." I have examined the final electronic copy of this dissertation for form and content and recommend that it be accepted in partial fulfillment of the requirements for the degree of Doctor of Philosophy, with a major in Physics.

Robert N. Compton, Major Professor

We have read this dissertation and recommend its acceptance:

Stuart Elston, Joseph H. Macek, Adam Petrie

Accepted for the Council:

Carolyn R. Hodges

Vice Provost and Dean of the Graduate School

(Original signatures are on file with official student records.)

Experimental and Statistical Techniques to Probe Extraordinary Electronic Properties of Molecules

A Dissertation Presented for the

Doctor of Philosophy

Degree

The University of Tennessee, Knoxville

Byron Hager Smith

December 2013

To my parents, Eric and Leslie, for all of the love and support offered through this endeavor. To Dale, the light of my life. And to my brother and sister, Elliot and Ginger, who taught me that levity is the key to success.

Acknowledgements

I would like to thank my major adviser, Dr. Compton, for the years of experimental experience that he has endowed me with. I would also like to thank the professors that taught me physics, chemistry, statistics, and humility.

...Our posturings, our imagined self-importance, the delusion that we have some privileged position in the universe, are challenged by this point of pale light. Our planet is a lonely speck in the great enveloping cosmic dark. In our obscurity - in all this vastness - there is no hint that help will come from elsewhere to save us from ourselves. It is up to us. It's been said that astronomy is a humbling, and I might add, a character-building experience. To my mind, there is perhaps no better demonstration of the folly of human conceits than this distant image of our tiny world. To me, it underscores our responsibility to deal more kindly and compassionately with one another and to preserve and cherish that pale blue dot, the only home we've ever known.

Carl Sagan

Abstract

The existence of an additional electron or hole in the presence of an electric monopole is a well understood physical system, but this ideality is far from the true physical properties of many molecules. Examples of such irregular electronic states include the attachment of an excess charge to a molecule's dipole moment, electronic correlation spanning a molecule, or attachment of multiple excess charges. Current theoretical and experimental interpretations widely vary for these states and further elucidation of the nature of extraordinary electronic structure may provide solutions to unexplained observations and the impetus for industrial application. For example, in the case of dipole-bound electrons, it has been proposed that high-dipole moment molecules will attach electrons through the dipole moment which is then captured in to a valence state. In order to test this hypothesis, dipolar electron attachment to *para*-Nitroaniline is investigated. In addition, electron correlation within highly symmetric molecules may play a role in silenced photoionization and provide insight in to so called "super-excited" states or "collective excitations". In pursuit of this electronic character, we use the complex multi-photon ionization of tetrakis(dimethylamino)ethylene to study the possibility of collective electronic excitations. For this purpose, a hemispherical energy analyzer was adapted to acquire photoelectron spectra. Also, the presence of multiple excess charge stabilized on a molecule demands the presence of a stabilizing factor such as the repulsive coulomb barrier. In order to ascertain evidence for such stabilizing factors, we use collisional charge transfer between 7,7,8,8-tetracyanoquinodimethane and sodium for which a threshold would provide a metric of stability (electron affinity). Finally, we

introduce Bayesian methods in the context of non-linear regression of collisional cross-sections (dissociative and charge-transfer) to address stability issues involved in the numerical estimations of partial derivatives. With this series of experiments we hope to shed new light on several types of extraordinary electronic states as well as to introduce the use of novel statistical methods.

Table of Contents

List of Tables

List of Figures

xiii

Chapter 1

Introduction

The presence of ions in a solution or compound play a major role in nearly every dynamic process, bridging nearly all length scales. The logarithm of the concentration of protons, or hydrogen cations, is so pervasive that it has been given its own term (pH). To this end, the reaction of molecules to form new materials is driven by the presence of ions.

In all matter, electrons are used as a currency between atoms. The energy associated with attachment of an electron is called the *electron affinity* (EA). Mathematically put, for a molecule M, this is given by

$$EA = E_M - E_{M^-}. \tag{1.1}$$

Because the attachment of an electron can cause a geometric change in the molecule, the electron affinity is further characterized as either adiabatic (AEA) or vertical (VEA). The former of these refers to the energy difference given that M and M$^-$ are optimized at their respective geometries. The vertical electron affinity, or vertical attachment energy refers to the energy difference only in the geometry of the neutral (Figure 1.1).

On the other hand, the detachment energy is a measure of the amount of energy required to detach an electron. Note that the adiabatic detachment energy is equal to the adiabatic electron affinity. This has been proven in the case of a neutral and a cation as *Koopman's Theorem*. The vertical detachment energy (VDE) then refers to the amount of energy

1
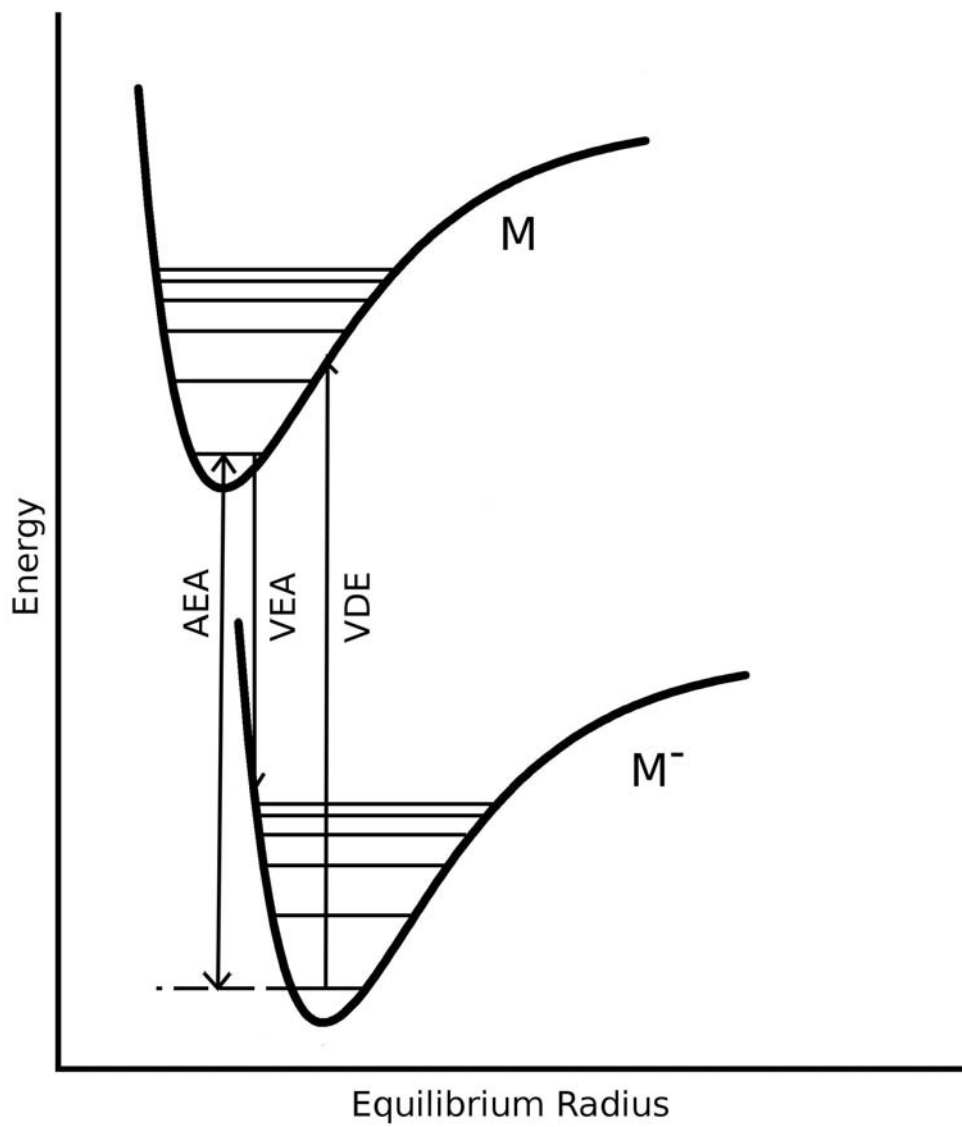
Figure 1.1: Morse potentials describing electronic energies.

required to remove the electron and leave the neutral in the same geometry as the anion (Figure 1.1).

The minimum energy input required to transition from the ground state of a particle to the continuous set of states describing the cation and free electron is called the *Ionization Potential* (IP). Thus, a single photon may ionize an atom or molecule if the energy of the photon is larger than the ionization potential. The most celebrated ionization potential is that of hydrogen (13.6 eV, non-relativistically) given that it is one of the only quantum systems that is analytically solvable. Atomic ionization potentials range from 3.89 eV for cesium to more than 23 eV for neon.

For atoms and Rydberg molecules, interpretation of the binding energy is relatively simple: This binding energy relates directly to the Coulomb interaction between a positive monopole and an orbiting negative electron. But, in the majority of molecules the spatial separation and complexity of multi-atom orbitals provide a experimental challenge for scientists. By focusing our sights on electron binding energy, we implement a variety of ionization methods to study these extraordinary electronic states in three particular examples detailed below.

Several ionization techniques exist which produce gas phase anions; typically these ions start as neutral molecules in the solid or liquid phase and the process of changing phase produces anions. Examples of such instruments include laser desorption ionization (LDI), matrix-assisted laser desorption ionization (MALDI), direct access in real time (DART), and electrospray ionization (ESI). LDI and MALDI utilize a sample in the solid phase placed as a thin film on a metallic plate. A laser is then used to ablate some of the material off of the plate which in turn produces ions. MALDI is distinguished from LDI in the fact that an additional component (the matrix) such as sinapinic acid is added to the sample in order to facilitate the ionization process.

In addition to LDI and MALDI which produce ions in a vacuum, DART is a commonly used ionization source. In this case the ions are created in a collision process upon entering the instrument in a fast beam of carrier gas molecules. Typically, collisions with vibrationally excited gas molecules will transfer enough energy to an analyte which results in electron

detachment and thus the production of cations. This process can be used with solids, liquids, and gasses, but is generally limited by the ionization process to cation detection of small, volatile molecules.

One innovation in particular, typically used in conjunction with time-of-flight mass spectrometry (TOFMS), advanced the study of gas phase molecules more than any other: Electrospray ionization. This ionization technique involves the ejection of an analyte solution with a volatile solvent through a syringe needle tip with an inner diameter on the order of microns. A large voltage is applied to this syringe tip to aid the ionization process. Thus, the presence of a large electric field in conjunction with the rapid vaporization of the solvent results in the soft-ionization of an enormous number of molecules. Prior to the advent of ESI, ionization sources such as the Niel source utilized filaments or free electrons to produce ions. Other methods include surface plasmon assisted laser desorption ionization (SPALDI), electron impact, photoionization, etc.

In order to experimentally investigate some of the more exquisite electronic properties of molecules, several of these ionization techniques may be taken in series. For example, one irregular bound state involves the binding of an electron to the electric dipole of a molecule (Chapter 3). Because the electron affinity associated with the dipole of a molecule is typically on the order of meV, soft ionization techniques must be implemented. Electron transfer between atoms in high Rydberg states and polar molecules is the main method of producing dipole-bound anions.

In the case of Rydberg electron transfer, an alkali atom is accelerated down the first of two flight tubes. While traveling down the tube, the atom is then intercepted with a laser which excites the outer most electron from an s-state to a high Rydberg level. At the end of the trajectory, the electron transfer target is put in to place via super sonic pulsed valve. Upon collision, the electron will be transferred from the Rydberg atom to the molecule which can then be further mass analyzed with a tandem TOFMS. The dipole-bound electron affinity can then be ascertained from the Rydberg state which results in maximal dipole-bound intensity. This technique has been extensively employed by the Compton group (Hammer et al., 2003, 1999) and the French group of Defrançois and Scherman (Defrançois et al., 1994).

From this work, a relationship between dipole-bound electron affinity and dipole moment can be drawn (3.10).

Slow electron attachment has been of limited value in the formation of dipole-bound anions. Nevertheless, electrons which attach to molecular dipole moments must have a low kinetic energy which makes this technique valuable. Typically a molecular anion is created with a convential technique, stripped of its electron during a collision process, and then passed over a heated filament. Based on the heat of the filament, the Fermi-Dirac distribution of electrons on the surface of the metal boil off with low energy. While this process is generally easier to implement, the attachment process does not contain any information about the dipole-bound EA. Instead, the ion source must then be tied to a photoelectron spectrometer to assess binding energies (Smith et al., 2013).

This technique was implemented to study dipole-bound electron attachment to *para*-Nitroaniline (Chapter 3). This molecule consists of a nitro group opposite an amino group on a conjugated six-member ring. Due to the electronegativity of the oxygens on the nitro group, *para*-Nitroaniline possess a large dipole moment which allows us to consider the relationship between dipole-bound electron affinity and dipole moment for larger dipole moments as well as the possibility of "doorway states" which have been shown in nitromethane, nitroethane, and nitrobenzene (Stokes et al., 2008; Compton et al., 1996; Desfrançois et al., 1999). We outline calculations which would suggest that two dipole-bound electronic states exist in this molecule and therefore we expect photoionization to provide information about binding energies and excited states of dipole-bound electrons.

In addition, we supplement detachment with collisional experiments and subsequent modeling. These collisional experiments are pretinent to the study of intra-molecular bonding and can be used to identify transition states based on the fragmentation pattern. The modeling of such experiments has been extensively detailed by the Armentrout group, though the algorithm for fitting is suspect due to instabilities in numerical approximations (Armentrout et al., 2008; Ervin and Armentrout, 1985; Webe et al., 1986; Schultz et al., 1991; Dalleska et al., 1994; Rodgers et al., 1997; DeTuri and Ervin, 1998; Iceman and Armentrout, 2003; Su, 1994; Ervin, 1999; Koizumi and Armentrout, 2003; Koizumi et al.,

2004; Amicangelo and Armentrout, 2001; Armentrout, 2007). For the purpose of robust modeling we introduce Bayesian techniques to circumvent numerical approximations.

The lack of photoionization from a dipole-bound state may be indicative of a "doorway state" in which electrons bind through the dipole moment and relax in to the valence state, but this is not only stabilizing feature of molecules versus photodetachment. The presence of a collective excitation of electrons under the influence of photons may be the cause of a lack of photoionization in highly symmetric molecules such as hexafluorides (Armstrong et al., 1994). Although never explicitly identified in an experiment, theoretical treatments of such states in molecules began in the 1960's (Nicolaides and Beck, 1976). In pursuit of such experimental evidence we consider the photoionization of tetrakis(dimethylamino)ethylene.

This molecule is symmetric with respect to the nitrogen atoms whose lone-pair electrons provide degenerate locations for photodetachment. Furthermore, it has been shown that a large absorption maximum lies about 1 eV above the ionization limit (Hori et al., 1968). Below we use a modified Comstock hemispherical energy analyzer to take photoelectron spectra at a variety of wavelengths in order to explore the possibility of collective excitations on small, symmetric molecules.

Another challenging problem in the world of electron binding involves multiply charged anions (MCAs) (Chapter 5). Only with advances of ionization techniques over the last forty years, have studies of multiply charged anions (MCAs) been performed (Dreuw and Cederbaum, 2002; Schroder and Schwarz, 1999). The investigation of the electric properties of gas phase MCAs has been championed by Wang *et al.*. Their instrument employs an ESI source in conjunction with a magnetic bottle photoelectron spectrometer. This setup allows for a large degree of flexibility as it can measure both positive and negative EDEs; as stated above, ejected electrons from molecules with negative EDEs are measured with larger kinetic energies than the incident photons. While the existence of several negative energy bound states has been predicted, empirical evidence for negative energy states was first observed in phthalocyanine tetrasulfonate tetraanions (Wang et al., 1998).

The existence of negative energy bound states implies that there must be a stabilizing feature that would allow for an electron to remain attached to a molecule. One example of

such a stabilizing mechanism is the *Repulsive Coulomb Barrier* (RCB). In many molecules the presence of several atomic nuclei provides enough Coulomb attraction to bind an electron directly. If this is not the case, it may be possible that a superposition of an attractive (monotonically increasing) Coulomb potential attributed to the series of nuclei on to a repulsive (monotonically decreasing) Coulomb potential attributed to the electrons results in a local minima. Depending on the particular orientation of nuclei and the form of the electron wavefunctions, this minima may lie above or below zero energy (Figure 1.2).

Although this is the only mechanism which results in negative bound electronic states, resonance states provide stability where there would otherwise not be enough to attach an electron. A *Feshbach Resonance* refers to the situation in which motion of multiple bodies can create a bound state. Take for example an electron scattering off of an atomic cation: The scattering may transfer energy to one of the cation's electrons raising it to an excited state. In turn, the projectile electron may then be captured in to a resonant state thus forming a doubly-excited neutral atom. Often these resonances are described in the context of ultracold, colliding atoms (Donley et al., 2002, 2001; Roberts et al., 2001). Experimentally, these resonances can be observed by "tuning" the coupling of two colliding atoms with their bound, molecular counterpart.

In order to further explore the stabilizing mechanisms we chose to study dianions of 7,7,8,8-Tetracyanoquinodimethane (TCNQ). This molecule contains two sets of cyano group pairs spaced symmetrically across a quinone moiety. Given the electronegativity of each cyano group, and the possible isolation of excess charge to opposite ends of the molecule, TCNQ provides a prime example of stable molecular dianions. For this reason, we utilize charge-transfer methods to make a measurement the second electron affinity. Unfortunately this molecule also reacts with many solvents which makes solution based for the production of the dianion difficult. Nevertheless, previous data taken at high colloision energies can be used to predict low-energy threshold for charge-transfer. Again, Bayesian and Frequentist techniques are juxtaposed to assess the utility of novel statistical techniques in the field of Chemical Physics.
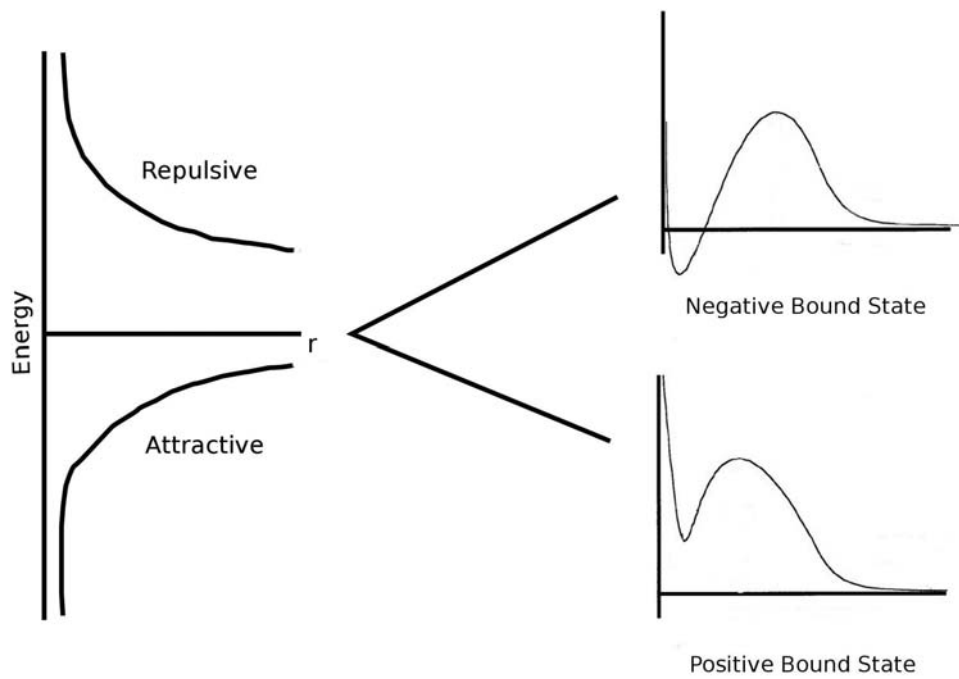
Figure 1.2: The repulsive coulomb barrier resulting positive and negative energy bound states.

By the use of these three specific experiments, we seek to elucidate complexities in the study of extraordinary electronic properties of molecules. Further analyses of these states may provide insight in to the interpretation of currently unexplained phenomena such as the Diffuse Interstellar Band (Sarre, 2000; Cordiner and Sarre, 2007) or the lack of direct photoionization signal in symmetric molecules (Armstrong et al., 1994).

1.1 Statistical Modeling

Modeling of experimental data can be broken into two very general perspectives: Exploratory data analysis and predictive data analysis. In the former, the researcher seeks to understand the full character of the data. This might include grouping data (i.e. cluster analysis and support vector machines), differentiating groups (i.e. discriminate analysis and analysis of variance), or characterizing groups (i.e. principal component analysis and factor analysis). Predictive analysis is more concerned with the prediction of future or unobserved data points; thus, model fitting is more often utilized to estimate where values should lie. Despite this contraction, both of these analysis paradigms use regression techniques to ascertain useful information about a data set. Here we consider the latter set of techniques in order to garner threshold values during collision processes.

All regression techniques follow a simple recipe: Begin with an *objective function* which characterizes the relationship between the independent and dependent variables and then minimize or maximize this function to solve for parameter estimates or other related quantities. When working with continuous data this function is typically the *sum squares error* (SSE):

$$SSE = \sum_{i=1}^{N} [y_i - \hat{y}_i(x)]^2 \tag{1.2}$$

where N is the number of data points. I will also introduce alternative functions which are used in the field of statistics for non-traditional modeling.

Analysis of collisional data requires non-linear modeling of two-dimensional data comprised of an independent variable (collision energy) and a dependent variable (cross-section). From a statistical perspective, non-linearity refers to the relationship between the fit parameters. For example, taking a, b, and c as fit parameters,

$$y = ae^{-x^2} + b\frac{1}{1-x} + c$$

is still a linear model as it is linear in the parameters, whereas

$$y = \frac{a}{b}x + c$$

is not. Linear modeling is preferred to non-linear modeling in all instances because it is more computationally efficient and the minimum error solutions are always analytic. For these reasons, whenever possible, we try to linearize the model by re-parameterizing. This may be done for the second model by replacing $\frac{a}{b}$ with a new parameter a'. When this method is not possible, non-linear regression algorithms must be implemented.

1.1.1 Linear Regression

Linear regression arises from three important assumptions:

1. The true relationship between the dependent variable and the independent variable is linear, i.e.

$$y_i = a_0 + \sum_{j=1}^{m} a_j f_j(x_i) + \epsilon_i$$

   where the ϵ_i are the errors or residuals.

2. The residuals are independent.

3. The residuals are normally distributed with mean zero, i.e. $\epsilon_i \sim N(0, \sigma^2)$.

10

In linear regression we start with the model

$$y = a_0 + \sum_{j=1}^{m} a_j f_j(x) \tag{1.3}$$

where the fit parameters are given by each of the a_i's. The hat is used to indicate that this is an estimator of the true dependent variable observations. Note that the functions $f_i(x)$ need not be linear in x, but must not include any of the fit parameters.

It is often easier to write this in terms of a matrix equation. To do so we first form the *design matrix*, $\mathbf{X}$. This matrix has as its first column a unity vector to represent a_0 while each subsequent column is comprised of the vector $X_{i,(j+1)} = f_j(x_i)$. The fit parameters are then written as a column vector. We can then write equation 1.3 as

$$\mathbf{y} = \mathbf{a}^\mathsf{T}\mathbf{X}$$

and the objective is to minimize the sum squares error given by

$$SSE = |\epsilon|^2 = |\mathbf{y} - \hat{\mathbf{y}}|^2 = (\mathbf{y} - \mathbf{a}^\mathsf{T}\mathbf{X})^\mathsf{T}(\mathbf{y} - \mathbf{a}^\mathsf{T}\mathbf{X}).$$

To minimize we simply take the derivative and set it equal to zero. Solving for this minimizing condition we are left with

$$\hat{\mathbf{a}} = (\mathbf{X}^\mathsf{T}\mathbf{X})^{-1}(\mathbf{X}^\mathsf{T}\mathbf{y}) \tag{1.4}$$

The application of the second and third assumptions are subtle, but can be highlighted when considering the *likelihood* as the objective function rather than the sum squares error. The likelihood is the joint probability distribution of all of the observations. This function is interpreted as the probability that given the independent variable, the dependent variable should arise. Given this interpretation it is clear that this function should be maximized rather than minimized. In this derivation the residuals are all independent, identically

distributed (i.i.d.) as Normal random variables:

$$
\begin{aligned}
\mathscr{L}(\epsilon) &= \prod_{i=1}^{n} \frac{1}{\sqrt{2\pi\sigma^2}} \exp\left(-\frac{\epsilon_i^2}{2\sigma^2}\right) \\
&= (2\pi\sigma^2)^{-n/2} \exp\left[-\frac{1}{2\sigma^2} \sum_{i=1}^{n} (y_i - \hat{y}_i)^2\right]
\end{aligned}
\tag{1.5}
$$

Notice from this formalism that maximizing the likelihood is equivalent to minimizing the sum squares error regardless of the value of σ^2. Using the likelihood instead of the sum squares error allows for another level of generality: We can now violate the normality of the residuals because the likelihood function can be chosen to be based on other distributions such as Gamma, Exponential, etc.

1.1.2 Non-linear Regression

Non-linear regression techniques are used to fit data when the model cannot be expressed in an equation which is linear in the fit parameters. This can be seen by attempting to apply the same techniques used above. As a demonstration I will consider the dependence of photo-electron signal (V) on laser intensity (I):

$$
V = aI^n
\tag{1.6}
$$

where a is a constant of proportionality and n is the order of the photo-ionization process. Note than any observed value will have some associated error, $V_i = aI_i^n + \epsilon_i$.

The sum squares error is then given by

$$
\sum_{i=1}^{N} (V_i - aI_i^n)^2
\tag{1.7}
$$

Taking the derivative of 1.7 with respect to a and n and setting them equal to zero results in two equations:

$$\sum_{i=1}^{N} -2I_i^n(V_i - aI_i^n) = 0 \tag{1.8}$$

$$\sum_{i=1}^{N} -2I_i^n \ln(I_i)(V_i - aI_i^n) = 0. \tag{1.9}$$

Except for the trivial solution $n = -\infty$, one can see immediately that these equations are not simultaneously solvable.

An easy solution to this problem would be utilizing a transformation in order to linearize the regression equation. In this case one would simply redefine some of the variables as $V_i' = \ln(V_i)$, $I_i' = \ln(I_i)$, and $a' = \ln(a)$:

$$V_i = aI_i^n \rightarrow V_i' = nI_i' + a'. \tag{1.10}$$

After this transformation it is easily seen that the regression techniques used above can be applied.

If a simple transformation is not possible, as is often the case, the previous optimization techniques are not useable and the problem must be tackled with less straightforward approaches. Conventional regression analysis can be viewed from two paradigms: A frequentist approach where the data are a representation of a population that was sampled from and a Bayesian approach where the data were observed and are therefore fixed so we seek to fit a population to it. The nuance between these interpretations is not immediately apparent, but the difference in the theory speaks much louder. I first begin with the frequentist approach as it is the most traditional.

Note that all approaches to non-linear regression are numerical optimization techniques and thus much more computationally expensive than linear regression. The first and most widely used non-linear regression strategy is to linearize the predictive function by the use of Taylor expansions in the parameters (Seber and Wild, 1989). Suppose the function is

13

written as $y = f(\mathbf{x}|\theta)$ for observation values x_i and parameter values θ_j for $j = 1, 2, 3, ..., m$. A first order linear expansion of this function in the parameters is then written as

$$f(\mathbf{x}|\theta) \approx f(\mathbf{x}|\theta^*) + \sum_{j=1}^{m} \frac{\partial f}{\partial \theta_j}|_{\theta_j=\theta_j^*}(\theta_j - \theta_j^*)$$

or in vector notation,

$$f(\mathbf{x}|\theta) \approx f(\mathbf{x}|\theta^*) + (\nabla f)|_{\theta=\theta^*} \cdot (\theta - \theta^*)$$

where θ^* is the true value of the parameter. The notation can be simplified by writing $\mathbf{F} = \nabla f|_{\theta=\theta^*}$ where $F_{ij} = \frac{\partial}{\partial \theta_j} f(x_i|\theta)|_{\theta=\theta^*}$. The sum squares error is then given by

$$SSE = [\mathbf{y} - f(\mathbf{x}|\theta^*) + \mathbf{F}^{\mathsf{T}}(\theta - \theta^*)]^2.$$

Rewriting this equation with $\mathbf{z} = \mathbf{y} - f(\mathbf{x}|\theta^*)$ and $\beta = (\theta - \theta^*)$ we return to the normal least squares regression form

$$SSE = |\mathbf{z} - \mathbf{F}^{\mathsf{T}}\beta|^2.$$

Once again, this error is minimized when

$$\beta = (\mathbf{F}^{\mathsf{T}}\mathbf{F})^{-1}\mathbf{F}^{\mathsf{T}}\mathbf{z}.$$

Clearly this solution cannot be directly implemented because θ^* is unknown; nevertheless it provides a recipe to arrive at the solution using numerical methods. The following regression method is called the *Gauss-Newton* algorithm.

1. Begin with an initial estimate of the parameter values, $\theta^{(0)}$.

2. Calculate the vector of the residuals as $\mathbf{r} = \mathbf{y} - \mathbf{f}(\theta^{(0)})$.

3. The parameter estimation step is then given by $\delta^{(1)} = \theta^{(0)} - \theta^{(1)} = (\mathbf{F}^{\mathsf{T}}\mathbf{F})^{-1}\mathbf{F}^{\mathsf{T}}\mathbf{r}$.

4. Update the parameter estimation as $\theta^{(1)} = \theta^{(0)} + \delta^{(1)}$.

5. Repeat steps 2 through 4 until a chosen level of convergence is reached.

14

Note that this updating process is driven by the residuals. A modified version of the Gauss-Newton algorithm called the *Marquardt-Levenburg Algorithm* is used when the square of the derivative matrix, $\mathbf{F}^\mathsf{T}\mathbf{F}$, is not well-behaved(invertible) (Seber and Wild, 1989). Consider first using the derivatives of the estimate residuals instead:

$$\mathbf{J} = \frac{\partial \mathbf{r}}{\partial \theta_j} = \frac{\partial[\mathbf{y} - \mathbf{f}(\theta)]}{\partial \theta_j} = -\mathbf{F}.$$

In order to produce a step in the iterative process of error minimization, the value

$$\delta^{(i)} = -(\mathbf{J}^{(i)\mathsf{T}}\mathbf{J}^{(i)} + \eta^{(i)}\mathbf{D}^{(i)})^{-1}\mathbf{J}^{(i)\mathsf{T}}\mathbf{r}^{(i)}$$

where $\eta^{(i)}$ is a parameter which "directs" the Gauss-Newton stepping with a steepest decent search and $\mathbf{D}^{(i)}$ is a diagonal matrix. Often, for simplicity, $\mathbf{D}^{(i)}$ is taken to be the identity matrix. Note that if $\eta^{(a)} = 0$ this formalism is identical to the Gauss-Newton Algorithm. With this in mind, the choice of $\eta^{(i+1)} = \eta^{(i)}/10$ is frequently used so that the influence of the steepest decent step is decreased throughout the iterative process.

The Marquardt-levenburg Algorithm is quite robust to initial conditions, but there are a plethora of $\eta^{(i)}$ constraints that can be implemented and any specific choice is generally subjective. By far the biggest challenge in implementing these algorithms comes from analytically evaluating the derivatives of the non-linear function. A clear example of these shortcomings is presented in the context of collision induced dissociation (Chapter 3).

1.2 Bayesian Modeling

In the Bayesian paradigm, a *posterior probability distribution*, or *posterior*, of the parameters is used as the objective function. At the heart of this thought process is the notion that the parameters are not fixed, but are distributed in some probability space. This is constructed by modifying the likelihood using Bayes' Rule: Given a parameter space dimensionality of

M, we begin with Bayes' Rule.

$$P(\theta|\mathbf{X}) = \frac{P(\mathbf{X}|\theta)P(\theta)}{\int P(\mathbf{X}|\theta)P(\theta)d^M\theta} \tag{1.11}$$

where the $P(\theta)$ are called *priors* or *prior probability distributions* and they represent *a priori* knowledge about the distribution of the parameters. The choice of these distributions presents a similar problem to the choice of the $\eta^{(i)}$ from the Marquardt-Levenburg Algorithm but with one catch - they are distributions rather than constants. Thus, they may be chosen to be diffuse so that they do not strongly influence the sampling procedure. In this case they are said to be *non-informative* in that there is no prior information about the parameters. In the limit that each prior is extremely diffuse and does not constrain the parameter space, the sampling procedure can be shown to be equivalent to randomly sampling the likelihood.

Typical choices for the prior distributions are those which result in a posterior of the same functional form; these are titled *conjugate priors*. The advantage to conjugate priors is that they leave the posterior in an analytical form so that random sampling is simplified. A few examples are listed in Table 1.1. When no conjugate is available typical choices include the Normal distribution or the Uniform distribution as they are symmetric and easily parameterized.

Table 1.1: Bayesian conjugate prior distributions.

Sampling Distribution	Conjugate Prior	Posterior
$x_i \sim Pois(\lambda)$	$\lambda \sim \Gamma(\alpha, \beta)$	$\lambda|x_i \sim \Gamma(\alpha + \sum_{i=1}^{n} x_i, \beta + n)$
$x_i \sim N(\mu, \sigma)$	$\mu \sim N(\mu_0, \sigma_0)$	$\mu|x_i \sim N((\frac{\mu_0}{\sigma_0^2} + \frac{\sum_{i=1}^{n} x_i}{\sigma^2})/(\frac{1}{\sigma_0^2} + \frac{n}{\sigma^2}))$
$x_i \sim N(\mu, \tau)$	$\tau \sim \Gamma(a, b)$	$\tau|x_i \sim \Gamma(a + \frac{N}{2}, b + \frac{1}{2}\sum_{i=1}^{N}(x_i - \mu)^2)$

Furthermore, prior probability distributions can be selected to constrain the parameter space. For example, if each of the model parameters must take a positive value (a

frequent requirement for physical interpretation), a convenient prior distribution would be the truncated Normal distribution, the Gamma distribution, the Log-Normal dsitribution, etc.

Distributions of regression parameter estimates then result from a sampling procedure called a *Markov Chain Monte Carlo Simulation* (MCMC). The ultimate goal of a Markov Chain Monte Carlo Simulation is to utilize a sampling procedure based off of Markov Chains in order to create a Monte Carlo sample which approximates the a sample from the posterior distribution of the parameters. Suppose that the set of all possible states forms a space, S_θ. Point-estimates of the parameters will then be given by the mean of the posterior distribution:

$$\hat{\theta} = E_{S_\theta}[\theta] \approx \frac{1}{N} \sum_{i=1}^{N} \theta_{MC}^{(i)} \tag{1.12}$$

where N is the number of Monte Carlo samples, $\theta_{MC}^{(i)}$. Monte Carlo samples asymptotically approach the true distribution of the states in S_θ. In a continuous state space the probability that any state is sampled more than once is zero and thus this asymptotic convergence can be visualized easiest via binning to form a histogram. Therefore, this mean represents the parameter estimates because each value (or value's neighborhood) will only be sampled asymptotically as often as the posterior distribution dictates. It is then necessary to produce a method of sampling from a distribution which is unknown.

A *Markov Chain* is a transition process which maps a state space to itself. The transition probability from any particular state i to another state j is labeled as P_{ij}. In a discrete state space the transition probabilities may form a matrix $\mathbf{P}$. In a continuous space this transition probability will take the form of some probability distribution, $P_{ij} = f(j|i)$. Thus, if the full conditional distribution of each parameter can be specified one can use the *Gibbs Sampler*:

1. Begin with an initial estimate of the parameters, $\theta^{(0)} = \{\theta_1^{(0)}, \theta_2^{(0)}, ..., \theta_M^{(0)}\}$ and some user chosen value N.

2. Sample the first parameter value $\theta_1^{(1)} \sim P(\theta_1|\mathbf{x}, \theta^{(0)})$.

3. Sample the second parameter value $\theta_2^{(1)} \sim P(\theta_2|\mathbf{x}, \{\theta_1^{(1)}, \theta_2^{(0)}, ..., \theta_M^{(0)}\})$.

17

4. Continue this sampling method for θ_i for $i = 3$ to M as

$$\theta_i^{(1)} \sim P(\theta_2 | \mathbf{x}, \{\theta_1^{(1)}, \theta_2^{(1)}, ..., \theta_{i-1}^{(0)}, ..., \theta_M^{(0)}\}).$$

5. Repeat this procedure N times. If the chain converges to a steady-state approximation of the posterior, the parameter estimates are then given by 1.12.

In most cases the full conditional probabilities are not available and so another method must be used to create the Monte Carlo sample. This is done using the *Metropolis Algorithm*:

1. Begin with an initial estimate of the parameters, $\theta^{(0)}$.

   For each parameter θ_i,

2. Sample a candidate parameter value, θ_i^*, using a symmetric random walk distribution (Normal, Uniform, etc.), $\theta_i^* \sim f(\theta_i)$.

3. Sample a random uniform number between 0 and 1, $u \sim Unif(0,1)$.

4. If $u \leq \frac{P(\{\theta_1^{(0)}, \theta_2^{(0)}, ..., \theta_i^*, ..., \theta_M^{(0)}\})}{P(\{\theta_1^{(0)}, \theta_2^{(0)}, ..., \theta_i^{(0)}, ..., \theta_M^{(0)}\})}$ then accept the value such that $\theta_i^{(1)} = \theta_i^*$ otherwise reject the value, $\theta_i^{(1)} = \theta_i^{(0)}$.

5. Repeat this procedure N times in order to get a sample of size N for each parameter. The parameter estimates are then given by 1.12.

In addition to the point estimates of the parameters we can use the Monte Carlo samples to directly calculate estimates of the correlation between the model parameters, confidence intervals at any level of confidence, prediction intervals, etc. This is particularly useful because in non-linear regression, the Frequentist interval estimates require the analytical derivatives. Approximations to these derivatives require similar computational techniques in addition to those used to arrive at the point estimates.

There are many alternatives to the non-linear regression techniques presented here. All of these techniques follow the same basic strategy: Identify an objective function and optimize it. A grid search for an optimized objective function can be implemented in order to find the prarmeter values of a non-linear regression. Ordering these values by the log-likelihood may

present some information on the confidence bands of the estimates as well. In this case the estimates are limited to the grid points; thus, more advanced searching algorithms can be utilized such as the genetic algorithm or simulated annealing. The objective function is not limited to the error, likelihood, or posterior either. Several other objective functions have been proposed such as Akaike's Information Criterion (AIC), Schwarz's Bayesian Criterion (SBC or BIC), or Information Complexity (ICOMP).

1.2.1 Bayesian Linear Regression

In order to contrast Bayesian and Frequentist methods of regression, simple (one independent variable) linear regression is presented within the Bayesian paradigm below. The regression model is then given by

$$y_i = \beta_1 x_i + \beta_0 + \epsilon_i = \beta^\mathsf{T} \mathbf{X} + \epsilon. \tag{1.13}$$

Based on the assumptions that were listed previously, each ϵ_i is Normally distributed with mean 0 and variance σ^2. Note again that the observed variables, x_i are fixed and thus have zero variance while the model parameters are random variables. It is easy to see then that the distribution of the dependent variable is Normal with mean $\beta_1 x_i + \beta_0$ and the likelihood is the product of each of these distributions:

$$\mathscr{L}(\epsilon) = (2\pi\sigma^2)^{-n/2} \exp\left[-\frac{1}{2\sigma^2}(\mathbf{y} - \beta^\mathsf{T}\mathbf{x})^2\right] \tag{1.14}$$

The following analysis is simplified greatly through the use of conjugate prior probability distributions for each of the model parameters:

$$f(\beta_0) = \frac{1}{\sqrt{2\pi\sigma_0^2}} \exp\left[-\frac{(\beta_0 - \mu_0)^2}{2\sigma_0^2}\right] \tag{1.15}$$

$$f(\beta_1) = \frac{1}{\sqrt{2\pi\sigma_1^2}} \exp\left[-\frac{(\beta_1 - \mu_1)^2}{2\sigma_1^2}\right] \tag{1.16}$$

19

The posterior distribution is the normalized product of the likelihood with the priors:

$$\pi(\beta_0, \beta_1 | \mathbf{y}, \mathbf{x}, \sigma^2, \mu_0, \sigma_0^2, \mu_1, \sigma_1^2) = N \frac{1}{\sqrt{4\pi^2 \sigma_0^2 \sigma_1^2}} (2\pi\sigma^2)^{-\frac{N}{2}}$$

$$\times \exp[-\frac{1}{2\sigma^2} \sum_{i=1}^{N} (y_i - \beta_1 x_i - \beta_0)^2 - \frac{(\beta_0 - \mu_0)^2}{2\sigma_0^2} - \frac{(\beta_1 - \mu_1)^2}{2\sigma_1^2}] \qquad (1.17)$$

Note that the form of the likelihood lacks separability of the model parameters. In this case the posterior is then a joint probability distribution given by a Multivariate Normal Distribution. Parameter estimates are then generated by using either the Gibbs Sampling Algorithm or the Metropolis Algorithm. In order to implement the Gibbs Sampling Algorithm, one must solve for the full conditional distributions:

$$\pi(\beta_0 | \mathbf{y}, \mathbf{x}, \sigma^2, \mu_0, \sigma_0^2, \mu_1, \sigma_1^2, \beta_1) \qquad (1.18)$$

$$\pi(\beta_1 | \mathbf{y}, \mathbf{x}, \sigma^2, \mu_0, \sigma_0^2, \mu_1, \sigma_1^2, \beta_0). \qquad (1.19)$$

In many circumstances this is not possible as the form of the conditional distributions are often not analytic. For this reason, I will demonstrate only the Metropolis Algorithm here. Let $F(\beta_1, \beta_2) = \pi(\beta_0, \beta_1 | \mathbf{y}, \mathbf{x}, \sigma^2, \mu_0, \sigma_0^2, \mu_1, \sigma_1^2)$.

- Begin with an initial set of parameter values $\beta_0^{(0)}$ and $\beta_1^{(0)}$. For $j = 1...S$ iterations,

- Sample a candidate β_0^* from the Normal distribution.

- Sample a random uniform number $u \sim U(0, 1)$.

- If $u < \frac{F(\beta_0^*, \beta_1^{(j-1)})}{F(\beta_0^{(j)}, \beta_1^{(j-1)})}$, accept the point as a new sample of the posterior: $\beta_0^{(j)} = \beta_0^*$ otherwise $\beta_0^{(j)} = \beta_0^{(j-1)}$.

- Sample β_1^* from the Normal distribution.

- Sample a random uniform number $u \sim U(0, 1)$.

- If $u < \frac{F(\beta_0^{(j)}, \beta_1^*)}{F(\beta_0^{(j)}, \beta_1^{(j-1)})}$ accept the point as a new sample of the posterior.

Example code is included in Appendix A.

1.2.2 Advantages and Disadvantages of Bayesian Analysis

Throughout this dissertation, the largest advantage of Bayesian statistics that we exploit comes from the lack of a need to evaluate the partial derivatives of a model. In frequentist techniques, partial derivatives also enter the algorithm through constraint equations via the Implicit Function Theorem. Therefore, issues involved in numerical approximations of derivatives used to constrain the parameter space as well as the modeling itself can be circumvented using Bayesian analysis. But, these are not the only advantages in using Bayesian tools.

By far the biggest accomplishment of the Bayesian school of thought comes from hierarchical modeling in which level upon level of complexity can be introduced in to the model. This has been shown to be useful in many fields, such as ecology (Clark, 2005) and may find some relevence in more complex processes in Chemical Physics. Additionally, imputation and agglomeration of modeled data can be performed simply with Bayesian tools by use of priors formed from previous posterior distributions.

These advantages come with a cost though, specifically a computational cost. Each simulation requires a large number of iterations to assure that convergence to a posterior probability distribution is achieved. Once there is an acceptable convergence, the primary iterations should be truncated. The number of iterations to be truncated is called the *burn-in* and can generally be assessed graphically. An example of this convergence is given in Figure 1.3 where convergence occurs roughly around 5000 iterations.

While a typical Marquardt-Levenburg optimization will run for less than 100 steps, a Bayesian analysis should run for more than 100,000 iterations. This is due to the large auto-correlation between sequentially sampled points which violates a random sampling assumption used to form the Monte Carlo estimate. An estimate of the true number of randomly sampled points can be drawn from the *effective sample size*, given by the number of iterations times one minus the auto-correlation in the sample. All modeling performed in this dissertation use effective sample sizes larger than 1000 for each of the parameters in the model.
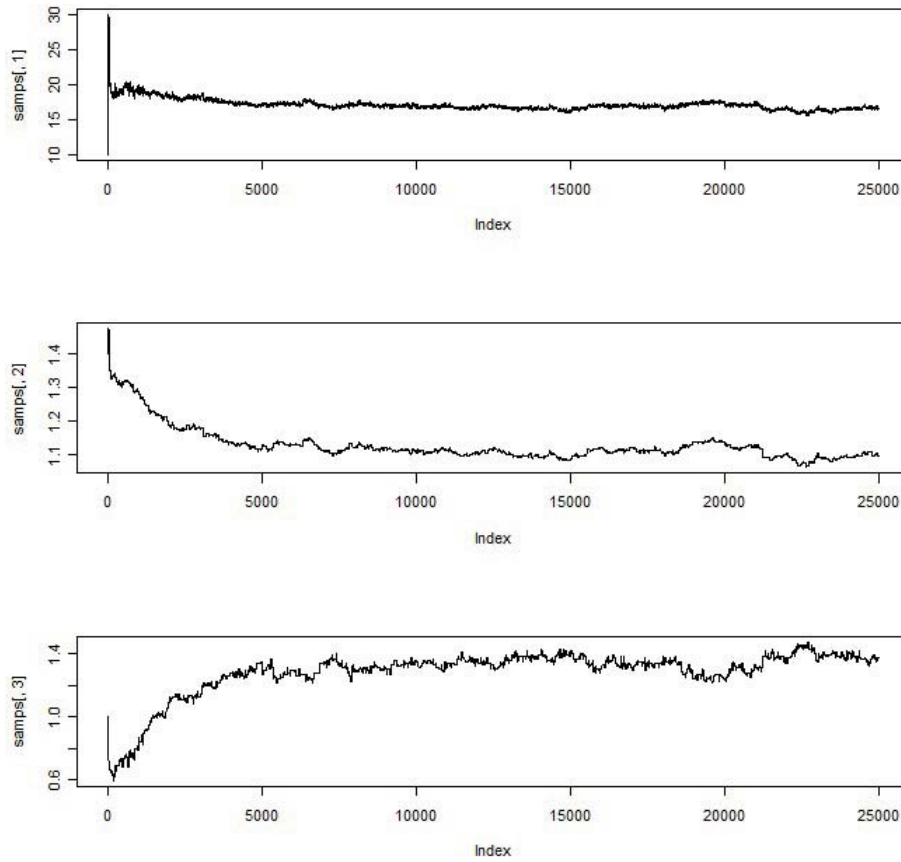
Figure 1.3: A graphical assessment of convergence to the posterior probability distribution during a Bayesian MCMC.

In both examples, inherent correlation between the model parameters may drive the estimation process. This can be seen clearly in Figure 1.3 between the second and third parameters as an increase in one of the parameters can be matched with a decrease in the other parameter. In a Marquardt-Levenburg optimization process, the partial derivatives of the model are functions of the other parameters which in turn drives each step of the optimization as well. One benefit of Bayesian computations allows a variety of tuning parameters that can be modulated while the inter-parameter correlation may be monitored so as to choose a particular value in order to minimize the effects of this situation throughout the simulation.

Chapter 2

Experimental Apparatus

Ion and electron energy analysis has been largely developed in the context of photoelectron spectroscopy (PES). Some current electron energy analyzers include time-of-flight mass spectrometers, Faraday cups, magnetic bottle mass spectrometers, and hemispherical or cylindrical shell energy analyzers. The predominant method of energy analysis follows from the first of these instruments, the time-of-flight mass spectrometer (TOF-MS).

The first type of detector that was used in photoelectron spectroscopy was a simple retarding grid set up. This used an applied voltage to gather electrons and recorded the resultant current. Because the signal monotonically increases, the final spectrum is then constructed from the derivative of the current vs. retarding voltage. Although this setup is straightforward and simple, the data recorded were of poor resolution and typically unstable.

In cases where data clarity is not as important, a similar instrument design has been implemented; this is the Faraday Cup. Instead of a simple plate, a conductive "cup" is used to gather incident ions. Again, this instrument style suffers from poor resolution. Examples where this may still be used are during preliminary analysis or cases in which simple detection is more important than measurement.

The TOF-MS has been the archetypical energy analyzer over the past few decades. Due to the ease of use and construction, this instrument provides a powerful tool. In addition, the

collection efficieny at low energies is excpetional provided proper focusing. Also, TOF-MS instruments can pass charged particles of all energies simultaneously.

In order to investigate product energy using a TOF-MS, a mass is assumed to be fixed so that only one product is being analyzed whether it is electrons or ions; typically this may be done with mass gating. After an initial charged particle packet is created, the packet is accelerated down a flight tube. The initial energy of each electron or ion is then expressed as a time-of-flight:

$$E = \frac{1}{2}mv^2 \Rightarrow t = \sqrt{\frac{mL^2}{2E}} \tag{2.1}$$

for mass m, flight tube length L, and kinetic energy E. One pitfall of this kind of analysis is that the time resolution is limited by the initial energy of the electron or ion. This is easily seen by simply considering the absolute value of the time differential:

$$dt = \frac{1}{2}\sqrt{\frac{mL^2}{2E^3}}dE. \tag{2.2}$$

Thus, the resolution of the instrument decreases significantly with higer energies.

Addtionally, the acceleration and focusing along the time-of-flight axis can convolute the initial energies in the direction of propagation. In order to utilize TOF-MS and preserve resolution at higher energies, one can adapt the detector to use ion imaging. This method utilizes the intial transverse motion or the charged particles in order to create an image. The axis of propagation for the ion packet is no longer measured, rather the transverse distance that the ions or electrons have travelled contains the information about the initial energy.

Because the locus of ion creation is relative small, we can approximate all charged particles as being created from a point. The initial motion of electrons or ions is then radially outward, with particles of the same energy forming spherical shells. The ion packet is then accelerated down a flight tube and collides with a detector, most often microchannel plates. The electron cascade from the channel plates is then accelerated on to a phosphorescent screen which illuminates a CCD detector. A landmark advancement in this field came from a focusing condition called *Velocity Map Imagaing (VMI)*. In this case, the charged particle

packet is then distorted along the propagation axis in order to focus particles of like velocity (and therefore kinetic energy) to the same point.

Resulting images give blurred, concentric rings whose radii reflect the ion energies. In order to acquire all of the information from the images an inverse Abel transformation is applied to the resulting data. This transformation is applied because the incident ion packet is essentially a three-dimension sphere being projected onto the microchannel plate detector. This is then transformed to "unfold" the sphere into a cylindrical shell. This method is particularly powerful because it allows one to acquire information on the initial energy and the photoangular distributions (under the condition or a polarized light source). A down side is that the focusing required to attain high transverse resolution comes at the cost of reducing the resolution along the axis of propagation.

The magnetic bottle spectrometer is similar to the TOF-MS, except that magnetic fields are used in order to corral electrons or ions toward the dift tube prior to analysis. While this increases the capture efficiency, the introduction of magnetic fields around the ionization region effects the initial energy distribution of the charged particle packet. This in turn is reflected in the spectrum. Also, the strong magnetic field can often be a part of the physics being studied.

In contrast to each of these, a cylindrical or hemispherical energy analyzer provides good resolution at low and high electron energies. In most cases a hemispherical energy analyzer is preferable to a cylindrical shell due to the flexibility of the sample insertion. In a hemispherical shell, electrons or ions which enter the energy analyzer at an angle may still reach the detector by following a path with a different azimuthal angle. For this reason, this type of electron energy analyzer has become widely used in commercial and home-built instruments for the purpose of low-energy photo-electron spectroscopy, x-ray photoelectron spectroscopy, and collisional-charge transfer experiments.

2.1 Energy Analyzer

In order to measure electronic binding energies throughout this dissertation, an ES-101 (Comstock) hemispherical sector energy analyzer was used. The instrument shell was transferred from the Oak Ridge National Laboratory to the University of Tennessee, after which we modified the electronics, detection system, and installed a computer-based acquisition system. Outlined below are each of these modifications in the context of the principles behind its usage.

The instrument used to record the data in this dissertation is depicted in Figure 2.1. Ionization and focusing occurs in a stainless-steel ante-chamber. This ionization processes studied here involve either multi-photon ionization, resonantly enhanced or otherwise, or collisional charge transfer. Following ionization, the charged particle of interest (electrons or ions) enter an electrostatic lens system. While being focused by the lens, the ions pass through a voltage difference dictated by the top of the lens system and a plate which the energy analyzer is mounted to. The hemispherical sector energy analyzer used here consists of two concentric, conducting hemispheres of radii equal to 3 inches for the inner hemisphere and 5 inches for the outer hemisphere. As stated previously, the energy analyzer works by establishing spherical equipotential surfaces over which charged particles of specific energies may travel. Once the path is complete, the impact of each charged particle with the detector prompts a voltage spike.

The first theory concerning the feasibility of hemispherical energy analyzers was presented by Purcell (Purcell, 1953). Given a conducting hemisphere with an applied voltage Φ_0, solving Poisson's Equation ($\nabla^2 \Phi = 0$) results in a voltage around the hemisphere of the form

$$\Phi(\mathbf{r}) = \Phi(r) = \frac{a}{r} + b \text{ for } r \leq r_0 .$$

where $r = |\mathbf{r}|$. Under boundary conditions given by the constant surface at any two radii r_1 and r_2

$$\Phi(r_1) = \Phi_1 \text{ and } \Phi(r_2) = \Phi_2$$

27
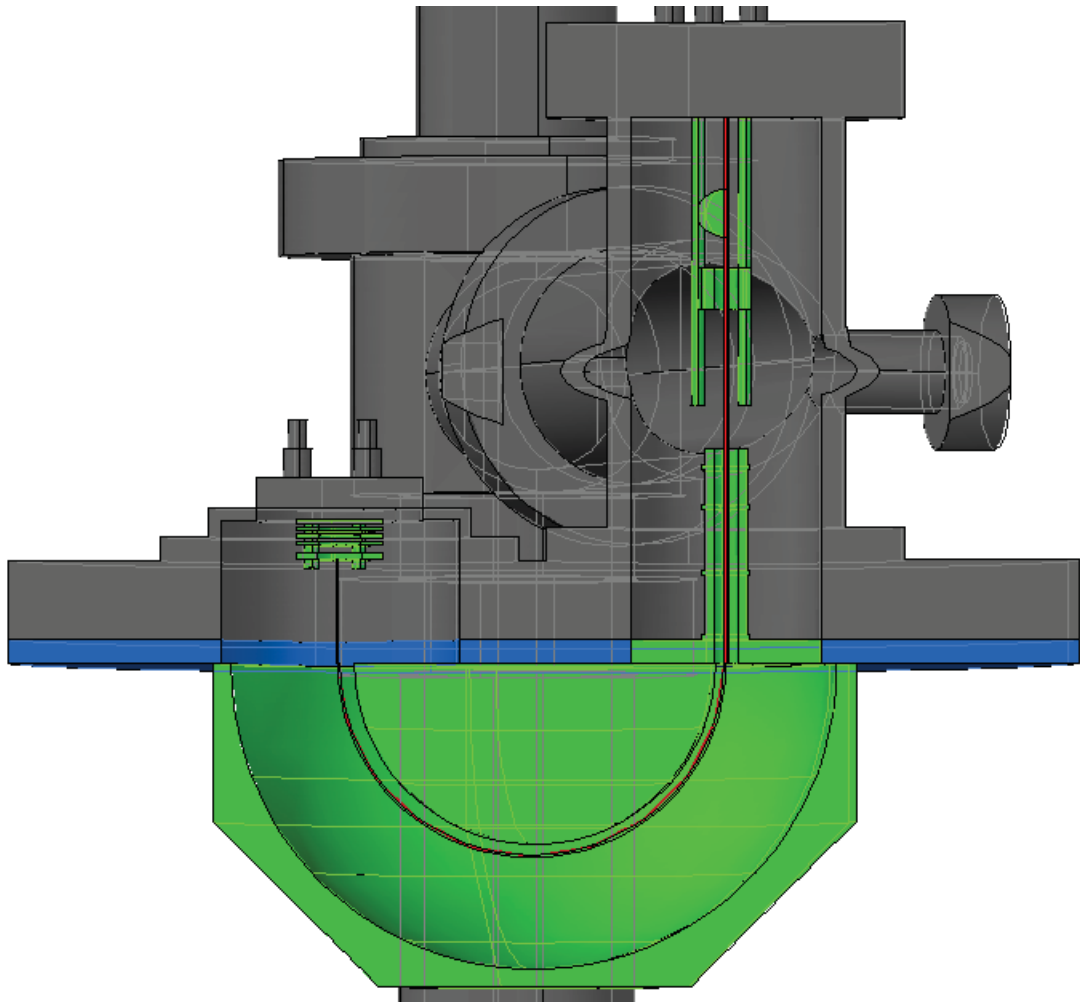
Figure 2.1: A 3-dimensional schematic of the hemispherical sector energy analyzer. The charged particle trajectory is shown in red.

one can solve for the constants as

$$a = \frac{r_1 r_2 (\Phi_1 - \Phi_2)}{r_2 - r_1} \tag{2.3}$$

$$b = \frac{r_1 \Phi_1 - r_2 \Phi_2}{r_1 - r_2}. \tag{2.4}$$

Thus, given two target constants one could solve for the potentials necessary to transmit electrons through the hemispherical energy analyzer.

These two target constants come from matching the radial force on the electron with the centripetal force associated with the circular motion. The centrifugal force on an electron traveling through the energy analyzer is given by

$$\mathbf{F}(r) = \frac{mv^2}{r} \hat{r} = \frac{2TE}{r} \hat{r}$$

for transmission energy $TE = \frac{1}{2}mv^2$. The electric field in the energy analyzer is given by the gradient of the potential:

$$\mathbf{F}(r) = -\frac{\partial \Phi}{\partial r} \hat{r} = \frac{a}{r^2} \hat{r}. \tag{2.5}$$

Equating the corresponding electrostatic force to the centrifugal force gives

$$e\frac{a}{r^2} = \frac{2TE}{r} \Rightarrow a = 2r\frac{TE}{e}. \tag{2.6}$$

Basic operation of the energy analyzer insists that an electron will have a given energy when ionization occurs which is subsequently accelerated or retarded to a select energy. Thus, any electron entering the analyzer will have some initial energy, KE. The voltage required to accelerate the electron is then given by $\frac{TE-KE}{e}$. The potential isosurface at the entrance of the energy analyzer must match this, i.e.

$$\frac{a}{r} + b = \frac{TE - KE}{e}$$

29

Plugging in the solutions to the constants from 2.3 and 2.4 we arrive at the equation

$$\frac{r_1 r_2(\Phi_1 - \Phi_2)}{r(r_2 - r_1)} + \frac{r_1\Phi_1 - r_2\Phi_2}{r_1 - r_2} = \frac{TE - KE}{e}. \tag{2.7}$$

Combining Equations 2.6 and 2.7 and simplifying gives that

$$\Phi_1 = \frac{1}{e}[TE(2\frac{r}{r_1} - 1) - KE] \tag{2.8}$$

$$\Phi_2 = \frac{1}{e}[TE(2\frac{r}{r_2} - 1) - KE]. \tag{2.9}$$

Taking the difference of equations 2.8 and 2.9 gives

$$\Delta\Phi = \frac{2TE}{e}(\frac{r}{r_1} - \frac{r}{r_2}). \tag{2.10}$$

It is readily apparent that the transmission energy of the energy analyzer is thus fully specified by the difference in potentials between the inner and outer hemispheres and the choice of radial pass surface, r. This pass surface is then given by the radial plane which intersects the position of the electron detector in the analyzer.

In many applications the pass surface is defined by the detector as the mean radius of the instrument

$$r = \frac{r_1 + r_2}{2} \Rightarrow \Delta\Phi = \frac{TE}{e}(\frac{r_2}{r_1} - \frac{r_1}{r_2}).$$

Two methods can then be implemented in order to measure the energy of incident electrons: Scanning one of the hemispheres or scanning an accelerating/retarding potential prior to entrance. The former method utilizes the relationship given above by scanning over $\Delta\Phi$. Practically, this can be done by holding either the inner or outer hemispheres at a constant voltage and scanning the other hemisphere over a range of voltages. This method modulates TE until the matching condition on $\frac{TE-KE}{e}$ is met. Notice that this can be done only because the pass energy is independent of the initial charged particle kinetic energy KE.

The second method is the one used to perform energy analysis throughout this dissertation. The transmission energy remains constant and a voltage is applied to the plate

just prior to entrance into the analyzer. This voltage then accelerates or decelerates the incident electron/ion so that the matching condition is once again met. This is equivalent to fixing TE and scanning the plate voltage until $\Phi_{plate} = \frac{TE-KE}{e}$. Note that implementation of this method fixes the voltages of the hemispheres relative to the plate voltage so that the equipotential surface does not change while scanning. In addition, this is prefered to scanning one of the hemispheres because the systematic error is a function of the pass energy; by changing the pass energy, the experimental error will scale as the energy of the molecule rather than being fixed.

As an example, suppose that we want to pass electrons with an energy of 1 electron-volt and the pass surface is defined by the mean radius. The voltages on the hemispheres are then given by

$$\Phi_1 = \frac{TE}{e}\frac{r_1}{r_2} + \Phi_{plate} \tag{2.11}$$

$$\Phi_2 = \frac{TE}{e}\frac{r_2}{r_1} + \Phi_{plate} \tag{2.12}$$

One can see that during any scan, the plate voltage is modulated directly and the hemispheres are scanned linearly with an offset. For an electron of energy 2 eV, $\Phi_{plate} = -1V$ and

$$\Phi_1 = \frac{1eV}{e}\frac{5}{3} - 1 \tag{2.13}$$

$$\Phi_2 = \frac{1eV}{e}\frac{3}{5} - 1. \tag{2.14}$$

2.1.1   Analysis of Performance

For a photoelectron spectrometer, the theoretical transmission is given by

$$\frac{\Delta E_{1/2}}{E} = \frac{w}{2r} + \alpha^2 \tag{2.15}$$

where $\Delta E_{1/2}$ is the full-width half-maximum, w is the average entrance slit width, r is the pass radius, and α is the angular velocity spread as they enter the energy analyzer (Kuyatt

and Simpson, 1967). Thus, the larger the pass radius of the instrument, the smaller the full-width half-maximum, and ultimately the better the resolution.

Ideally the size of the instrument can be increased indefinitely for perfect resolution. Practically, the size is limited by several factors, the most important being the presence of magnetic fields. In this case the effect of external magnetic fields such as Earth's are mitigated by mu-metal shielding. This may not be effective at much larger sizes though.

In general there are two quantities with which one can evaluate the performance of a hemispherical energy analyzer: The dispersion and the trace width. The former of these refers to the ability of the instrument to spatially separate ions of different kinetic energies. In other words, for a given pass energy E_0, the dispersion is given by

$$D = \Delta x \frac{E_0}{\Delta E} \tag{2.16}$$

For a 180 degree hemispherical sector energy analyzer this has been shown to be $2R_0$ (Wannberg et al., 1974).

The trace width is a measure of the size of the electron impact spot given that the electrons have some angular spread, $\Delta \alpha$ upon entering. Given in terms of a spread in pass radius, this is then given by

$$R_0(1 + \delta) = R_0 \frac{\cos^2(\Delta \alpha)}{1 + \sin^2(\Delta \alpha)} \tag{2.17}$$

where the radial displacement caused by $\Delta \alpha$ is given by $R_0 \delta$ (Hafner et al., 1968). It has been shown that this can be reduced to

$$\delta = -2(\Delta \alpha)^2 \Rightarrow R_0(1 + \delta) = 2(\Delta \alpha)^2 R_0. \tag{2.18}$$

A figure of merit that is often used to assess the resolving power of a hemispherical energy analyzer is the ratio of the dispersion to the trace width, i.e. $(\Delta \alpha)^2$.

2.2 Electrostatic Lens

Electrostatic lenses are used in order to focus charged particles based off of radial electric fields. Often times this lens is a three element *Einzel Lens* with alternating polarity of voltages. The first and third element will have the same voltage so as to not incur a change of charged particle energy. The voltage differences between each lens element causes focusing by first spreading any charged particle beam and then focusing. The initial broadening of the charged particle beam is differential; in other words, those charged particles which are least centric are spread the most initially. The subsequent focusing is differential as well.

In many applications one wishes to accelerate charged particles while focusing. If this is the case, the potential topography must be changed to incorporate a voltage difference between the first and last lens element. The lens system can then be though of as a series of drift tubes similar to those used in particle accelerators. The electrostatic lens used in this instrument is a tiered, three element lens with each segment larger than the last (Figure 2.2) (Wannberg and Skollermo, 1977).

The ideal voltages applied to each of the lens are given by

$$
\begin{aligned}
V_1 &= 0 \quad\quad\quad\quad\quad\quad\quad\quad\quad\quad\quad\quad\quad\quad (2.19)\\
V_2 &= \frac{0.22}{e}E_i + V_r \\
V_3 &= \frac{15.1}{e}E_i + V_r \\
V_4 &= V_r
\end{aligned}
$$

where E_i is the energy of the incident electron and V_r is the accelerating or retarding potential provided by the plate. Again, due to the existence of contact potentials the optimum coefficients of E_i must be arrived at empirically. In the case of photoelectron spectroscopy
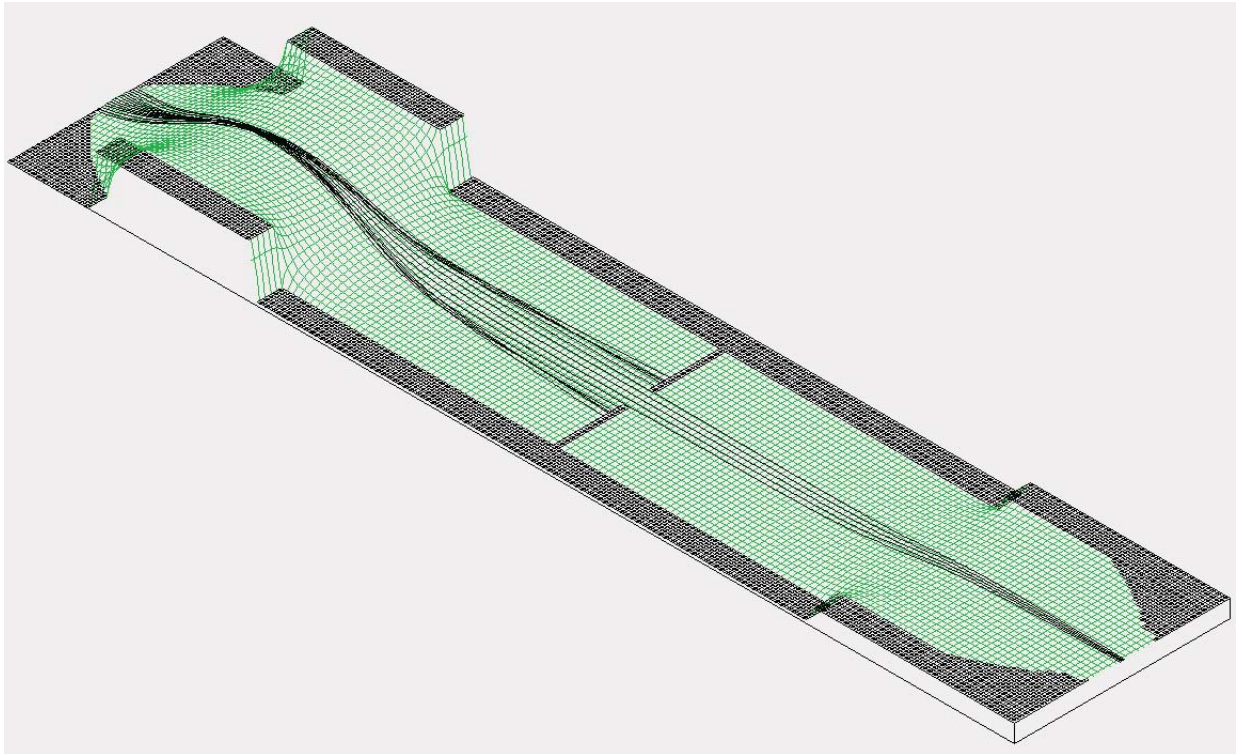
Figure 2.2: SIMION simulation of electrostatic lens using 1 eV electrons dispersed about the entrance aperture.

(Chapter 4), signal was sufficient to use cosntant potentials given by

$$V_1 = 0 \hspace{4cm} (2.20)$$
$$V_2 = 4.15\text{V}$$
$$V_3 = 49.50\text{V}$$
$$V_4 = V_r.$$

2.3 Signal Detection and Processing

In order to detect the charged particles which traverse the experiment, a series of chevron stacked channel plates are placed on the other side of the entrance hole (Del Mar Photonics). Each plate consists of a mesh of micron sized glass holes bored through at an angle between 5 and 15 degrees relative to the facial plane and coated with a metal (often a nickel-chromium alloy). A chip from the border indicated the channel slant direction on each plate so that plates in series may be positioned to maximize the amplification. A manufacturer suggested voltage of 900 V is applied across each channel plate in order to bias the electron flow direction towards a collection plate (2.1). Throughout the experiment this value is modulated to allow for an appropriate signal to noise ratio.

The channel plates are mounted between thin cylindrical shell, stainless steel plates with an inner diameter appropriate for the active area of the channel plates. In front of the channel plate stack a gold mesh grid is used to homogenize the electric field at the exit of the energy analyzer. Finally, collection of the electrons leaving the second channel plate are collected on a stainless steel plate, directed by a bias voltage. Signal was then collected through a capacitor which acted to set a time constant of the outgoing signal as well as zeroing the voltage offset. All voltages were applied via resistive voltage dividers (2.3).

Given that each channel plate has a resistance of approximately 100 MΩ, proper voltage division is attained by using the following resistances: $R_1 = 1230\Omega$, $R_2 = 9.97\text{M}\Omega$, and $R_3 = 9.95\text{M}\Omega$. The capacitor has a capacitance of 1.067 nF and thus the voltage spike time scale is set to be $C \times R_3 \approx 1.2\mu s$.

The post-production signal was amplified by a factor of approximately 45 using an Ortec 474 Timing Filter Amplifier. The amplified signal was then integrated using an SRS Gated Boxcar Integrator with between 30 and 300 averages. The specific number of averages was chosen to balance the signal-to-noise ratio and the acquisition time which directly relates to the drift of laser power.

One of the main advantages of the modifications made to this instrument was the dramatic increase in acquisition speed due to computer integration. While previous scans would take on the order to hours to run, these improvements reduced scan time to about 15 minutes. In order to acquire the data, the National Instruments Labview v8.1.0 programming suite was used in accord with a National Instruments Data Acquisition Board (DAQPad6020E). A sample image of the front panel and block diagram are shown in figures 2.4 and 2.5. Through the program, four of the BNC connections were used to (1) Output a scanning voltage, (2) Trigger data acquisition concomitant with laser pulses, (3) measure the output scanning voltage, and (4) measure the signal voltage. The third BNC connection used here was deemed necessary because the output precision used in the scanning voltage was not precise enough. For example, if the output voltage target was 1.010 Volts, the DAQPad may output 1.010 ± 0.007. For target Full-Width Half-Maximums (FWHMs) on the order of 10 meV, this inaccuracy must be accounted for.

A number of data points (25 to 250) were recorded from each of the two input channels at a rate of 10 kHz. The final recorded value was taken to be the average of these points as a method of minimizing the noise produced from errant signals in the DAQPad. A delay of approximately 5 seconds between each acquisition was used to let the boxcar integrator complete the averaging process. Given a smaller delay, the averaging can be seen prominently within each peak as an exponential relaxation to the baseline.
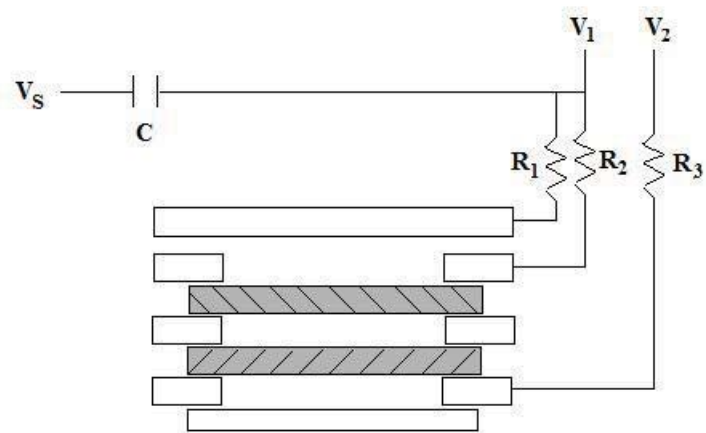
Figure 2.3: Circuit schematic for channel plates.
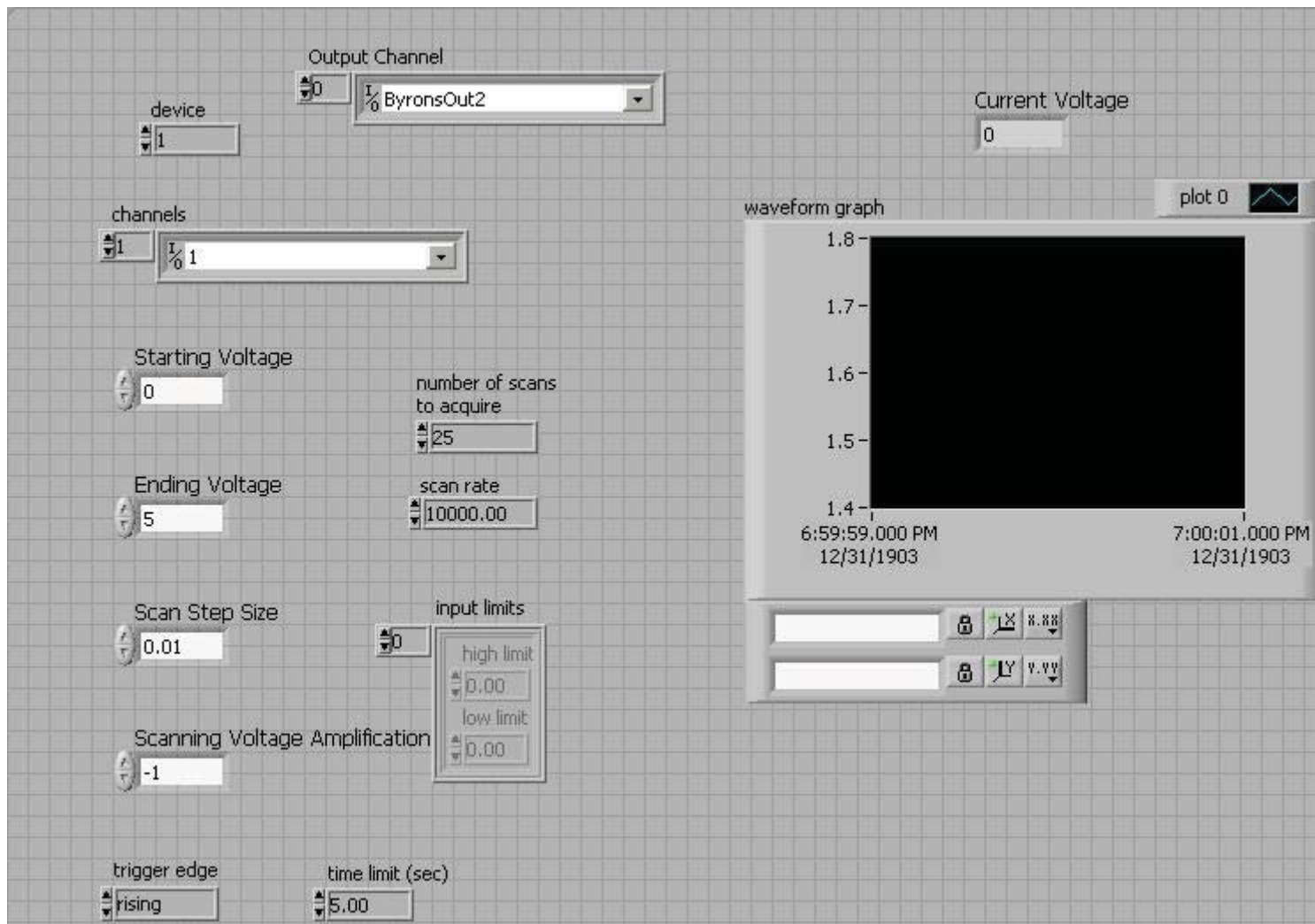
Figure 2.4: Labview front panel used to scane energies with the energy analyzer.

38
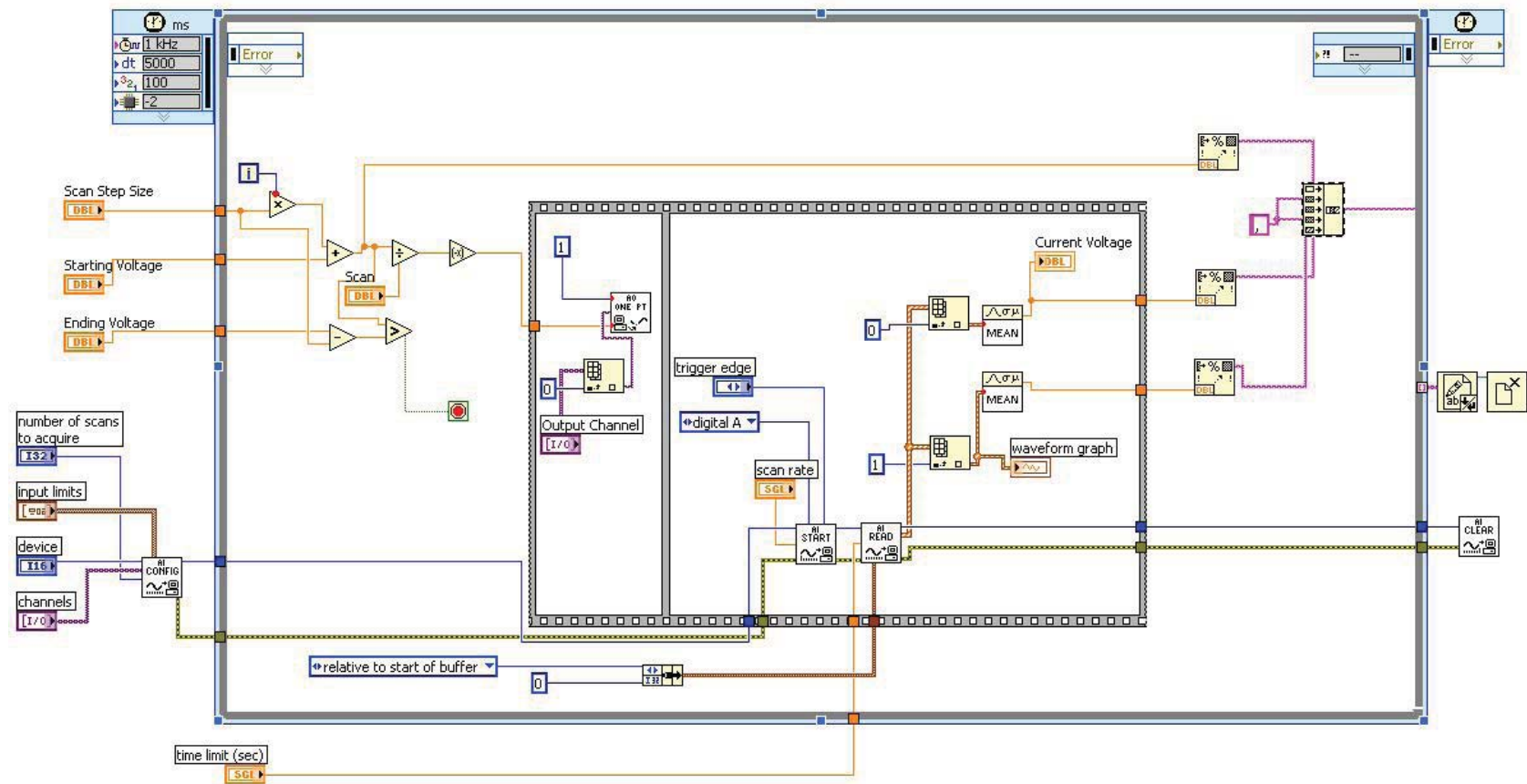
Figure 2.5: Labview block diagram used to scan energies with the energy analyzer.

Chapter 3

Collision-Induced Dissociation of p-Nitroaniline

The minimum dipole moment required to bind an electron has been a historical problem, beginning to take form in the late 1960s when a series of calculations resulted in a minimum dipole moment of $0.693a_0$ where a_0 is the Bohr radius. Unbeknownst to these scientists, Teller and Fermi had arrived at an identical value in 1947 (Fermi and Teller, 1947). During the 1970's, Garrett and Crawford identified the fact that a real, rotating dipole moment depends on the moment of inertia and initial length (Garrett, 1970, 1971; Crawford, 1971; Garrett, 1972; Carwford and Garrett, 1977; Garrett, 1978, 1979a,b, 1980, 1982). With this fact, they find that the minimum dipole moment will increase with rotational quantum number. Therefore, they conclude that the minimum dipole moment for binding an electron is about 2.5 Debye.

In order to elucidate the relationship between electric dipole moment and electron binding energy for state bound to that moment, we chose to explore *para*-Nitroaniline (pNA). The structure of pNA is a benzene ring with an amine group (NH_2) and a nitro group (NO_2) in the *para*- position (Figure 3.1). This allows for a "push-pull" electronic structure in which the electron accepting nitro group will pull electron density from the electron donating amine group. The separation of an electron donating group and electron accepting group across a
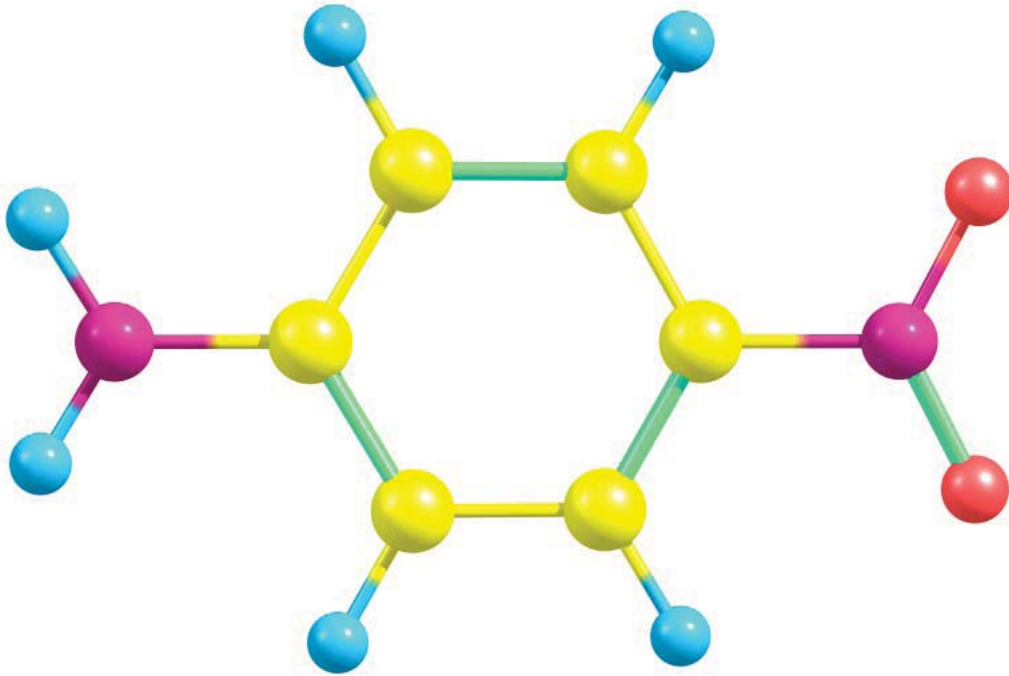
Figure 3.1: Molecular structure of pNA.

benzene ring also implies that the molecule has a large dipole moment. This dipole moment has been measured as 6.2 Debye (Cheng et al., 1991) in acetone and has been calculated to be between 7.0 and 8.1 Debye (Soscún et al., 2006). Further, the dipole moment of an excited state of the molecule has been measured to be as large as 13.35 Debye (Kawski et al., 2006).

3.1   Computational Analysis

Because the dipole moment of pNA is much larger than the critical value, it would seem that the molecule should form a dipole bound anion. In order to explore this concept more the electronic states were computationally explored using a variety of basis sets and levels of theory. Vibrational motion in pNA causes a wagging motion of the amino group which causes any optimized geometry to be a superposition of a planar geometry with C_{2v} symmetry and a "bent" geometry with C_s symmetry. This is also responsible for instabilities in the geometric optimization procedure using second order Møller-Plesset perturbation theory. In order to rectify this problem, the TPSS density functional was used to validate any optimization (Tao et al., 2003). The basis set used in each of these calculations was Ahlrich's redefined triple-ζ set augmented with a minimal set of diffuse functions (ma-Def2-TZVP) (Weigend and Ahlrichs, 2005; Papajak and Truhlar, 2010).

Electronic states were then calculated using the equation-of-motion coupled-cluster method with single and double excitations for electron affinities (EA-EOM-CCSD). Due to spin contamination in Hartree-Fock calculations for the anion, coupled-cluster calculations were performed using the orbitals of the neutral (QRHF coupled-cluster calculations). The basis sets used were Dunning's correlation consistent double-ζ (Aug-cc-pVDZ) and triple-ζ (Aug-cc-pVTZ) sets. Based on the geometry used, the results show that there are 3 predicted dipole-bound states (Table 3.1).

Table 3.1: Vertical Detachment Energies (in eV) for dipole bound states in pNA

	C_{2v} symmetry		
	1st $^2A_1$	2nd $^2A_1$	1st $^2B_1$
Aug-cc-pVDZ+	104	2.0	47
Aug-cc-pVTZ+	107	2.0	208
	C_s symmetry		
	1st $^2A'$	2nd $^2A'$	3rd $^2A'$
Aug-cc-pVDZ+	110	80	1.5
Aug-cc-pVTZ+	261	96	1.5

3.2 Photoelectron Spectroscopy

In order to generate the photoelectron spectrum, ions were first created using slow electron attachment. The sample of pNA entered the instrument via supersonic expansion through a pulsed valve with a carrier gas of argon. Electrons are then produced from a hot thoriated iridium filament and freely attach to pNA. A beam of the negative ions is then crossed perpendiculary with a 488 nm Ar-ion laser for photodetachment. After passing through a series of ion optics, electron energy is then evaluated in a hemispherical energy analyzer.

Dipole-bound electrons manifest themselves as very low energy electrons in the photoelectron spectrum. It can be seen that no dipole bound character is seen in this spectrum (Figure 3.2) The lack of dipole-bound signal is somewhat expected due to the unusually large dipole moment resulting in electronic states which show a superposition of dipole-bound and valence characters. The case may be that those electrons which are captured in to dipolebound states quickly stabilize by transitioning into a valence bound anionic state, similar to what has been seen in nitroethane (Stokes et al., 2008), nitromethane (Compton et al., 1996), and nitrobenzene (Desfrançois et al., 1999).

Photoionization occurs on very fast time scales implying that any photoelectron spectrum will be peaked at vertical ionization. Most experiments assume that the initial anion
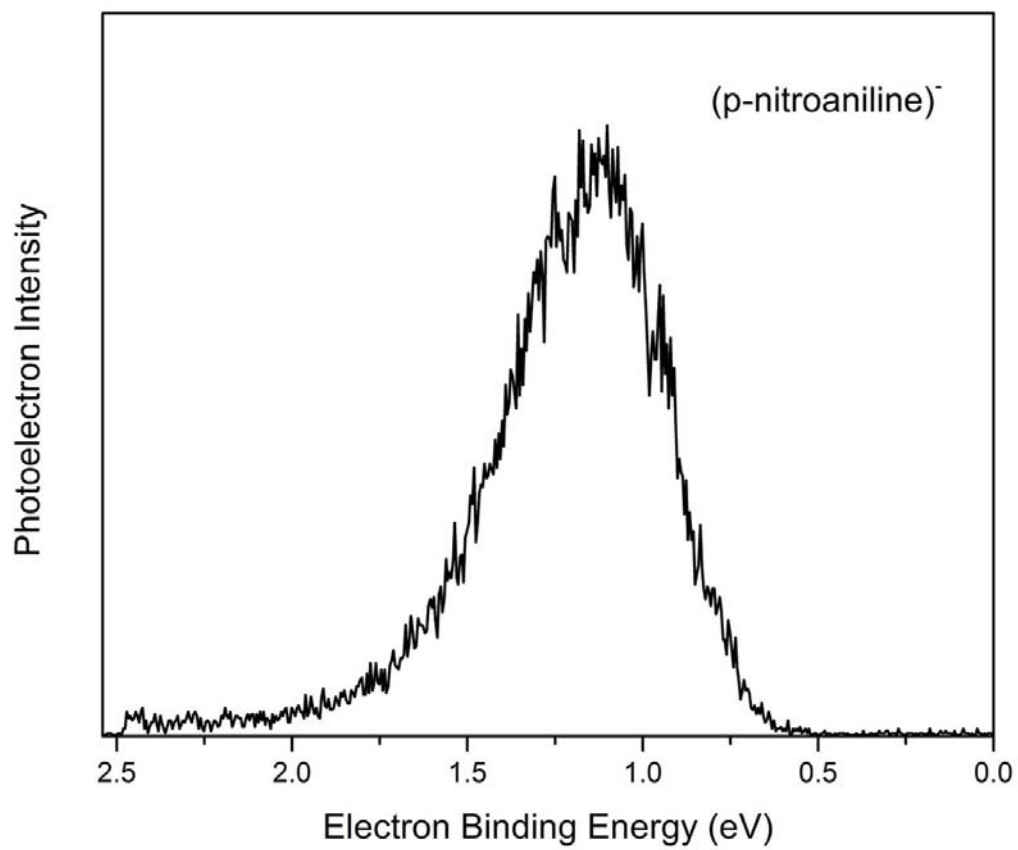
Figure 3.2: Photoelectron spectrum of pNA.

or neutral state is a ground state implying that the low energy onset of photoionization represents ionization from the groud state of the target to the ground state of the electron-detached target species. For this reason, inference on adiabatic electron affinities and ionization potentials can be supplemented charge-transfer processes which show a threshold at the difference between the adiabatic ionization potential of a target and the adiabatic electron affinity of the projectile. For this reason, tandem mass spectrometry techniques were used to look for charge-transfer signal. Unfortunately no such signal could be seen due to a preference for dissociation. Nevertheless, information about collision-induced thresholds hold important information about molecular stability and bond strengths. Furthermore, the modeling process of such thresholds provide the impetus for more robust statistical techniques such as the Bayesian modeling described below.

3.3 Collision Induced Dissociation

All collision-induced dissociation experiments were carried out with a QStar Elite triple-quadrupole system (ABSciex) using argon as the collision target. Ions are produced in solution (methanol) and enter the instrument through an electrospray ionization (ESI) source in a curtain gas of nitrogen. After passing through a series of electronstatic elements, the ions are spatially separated from any contaminant in the first of three quadrupoles. The second quadrupole is then used to mass select the parent ions to be collided. Prior to collisions, the ions are then accelerated or decelerated through a potential difference to a target collision energy. Collisions then occur in the final quadrupole (Figure 3.3).

The pressure of the collision target was held at approximately 3.5×10^{-5} torr, consistent with previous experiments (Lynden-Bell et al., 1998; Khan et al., 1993; Muntean and Armentrout, 2001; Amicangelo and Armentrout, 2001; Armentrout et al., 2008; Dalleska et al., 1994; Rodgers et al., 1997). The collision cell in the QStar Elite system is 21.2 cm long, slightly longer than other CID experiments.

Calibration of the energy scale was first carried out using a retardation analysis in which the collision energy was reduced to the point of vanishing signal. The signal dropped below
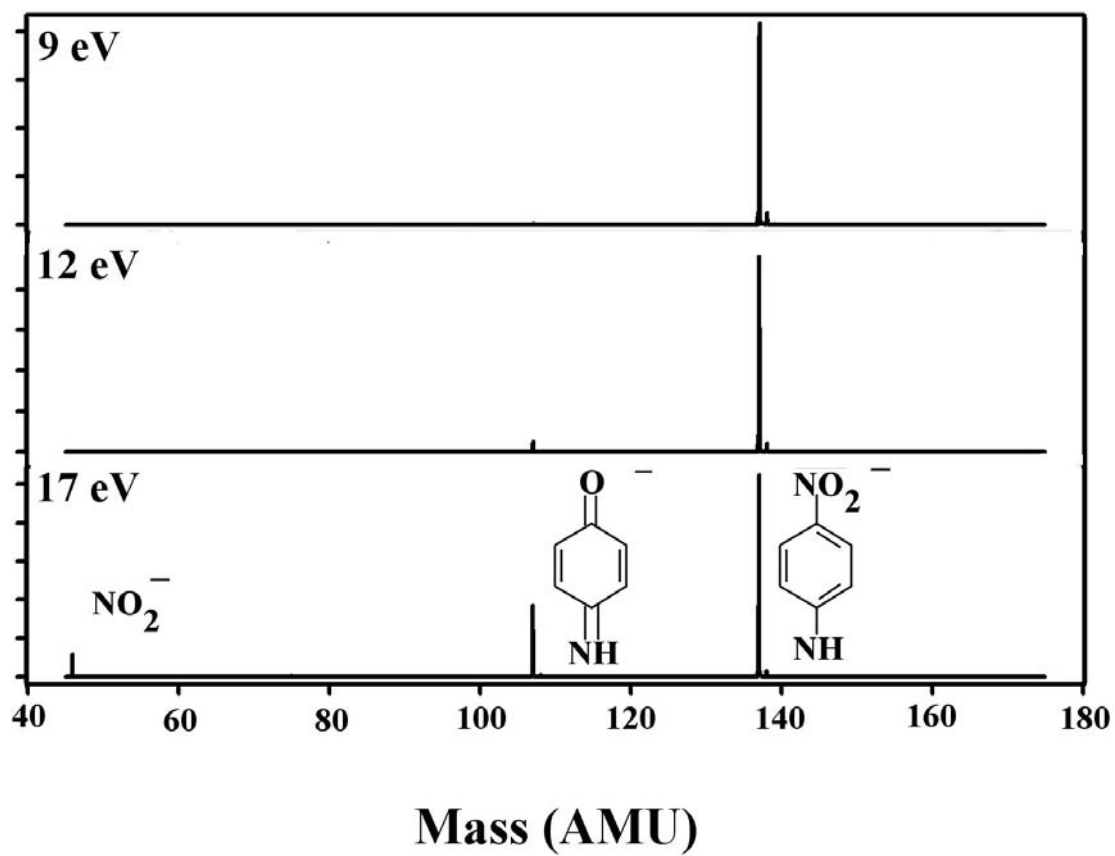
Figure 3.3: Fragmentation of pNA under a collision energies of 9 eV, 12 eV, and 17 eV in the lab frame.

the noise level at a setting of 0 ± 0.5 eV in the lab frame as expected. A stronger calibration was also included in which ions of tri-iodide were dissociated:

$$I_3^- \rightarrow I_2 + I^- \tag{3.1}$$
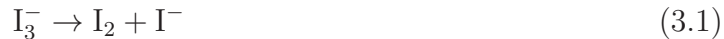
which has been shown to occur at an energy of 1.31 ± 0.06 eV (Do et al., 1997; Hoops et al., 2004; Lynden-Bell et al., 1998). Collisional dissociation and subsequent fitting detailed below result in a value of 1.32 ± 0.069 eV validating the energy scale.

Suppose that an N-atom molecule, M, is colliding with a target. The target is usually atomic, but the formalism here relates only to the molecule of interest. The molecule will have $3N$ associated degrees of freedom corresponding to three translational modes, 3 rotational modes, and $3N - 6$ (assuming that the molecule of interest is non-linear). In phase space each degree of freedom will have two affiliated dimensions - one for the "position" and one for the "momentum". Thus, the total system can be described classically using a $6N$ dimensional phase space. Within this phase space energy is conserved and thus a constant energy hyper-surface of $6N - 1$ dimensions. The transition will typically follow
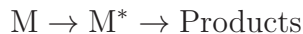
$$M \rightarrow M^* \rightarrow \text{Products}$$

so that an intermediate excited state has been passed through which will then dissociate into the products. This dissociation will occur only if the excited state is of a particular (threshold) energy or larger. Then, the threshold energy surface defines another $6N - 1$ dimensional hyper-surface. Thus, the intersection of these two hyper-planes assures the existence of the process of interest and will itself form a hyper-plane of $6N - 2$ dimensions. The unimolecular reaction rate is then given by the ratio of the number of states available to incur dissociation divided by the total number of states:

$$k_{uni} = \frac{N^t(E - E_0)}{h\rho(E)} \tag{3.2}$$

where $N^t(E-E_0)$ is the number or degeneracy of states with energy $E-E_0$ in the transition state and $\rho(E)$ is the density of states of the colliding molecule and atom. From this reaction rate the cross-section of any reaction is then given by

$$\sigma(E) = \int_0^{E-E_0} f_d(E')(1 - e^{-k_{uni}\tau})dE' \tag{3.3}$$

where $f_d(E)$ is an empirical amplitude function and τ is the time scale over which the unimolecular reaction could take place (for time of flight mass spectrometry this is on the order of 10^{-4} seconds). The empirical function used in the fitting procedure was conceptually derived from step function threshold of dissociation by Armentrout *et al.* and is given by

$$f_d(E) = \sigma_0 \sum_{i=1}^{M} g_i(E + E_i - E_0)^n/E \tag{3.4}$$

where the sum is evaluated over ro-vibrational energies, E_i, E_0 is the threshold energy, σ_0 is a scaling parameter, and n is a smoothing parameter (Armentrout et al., 2008; Ervin and Armentrout, 1985; Webe et al., 1986; Schultz et al., 1991; Dalleska et al., 1994; Rodgers et al., 1997; DeTuri and Ervin, 1998; Iceman and Armentrout, 2003; Su, 1994; Ervin, 1999; Koizumi and Armentrout, 2003; Koizumi et al., 2004; Amicangelo and Armentrout, 2001; Armentrout, 2007). The fitting procedure should then maximize likelihood over the parameter space spanned by values of E_0, σ_0, and n.

The unimolecular reaction rate is not only highly non-linear, but it usually does not have a functional form and is often discretely defined. This is because the density and sum of states is often calculated with a direct counting. Given the modern advances in computational power and the incredibly efficient Beyer-Swinehart Algorithm, the process of counting simply requires a discretization of the energy scale called *graining* (Beyer and Swinehart, 1971). Approximate methods of arriving at the density and sum of states such as a thermally motivated steepest decent approach or semi-empirical modeling have been suggested by some (Klots, 1996). Nevertheless, these fail to simplify the fitting procedure

which often require numerical methods of approximating the derivatives which have been shown to be unstable (Narancic et al., 2007).

Before fitting began, the collision energy must be corrected for thermal motion in the collision target. Ostensibly this correction can be taken through a transformation to the center of mass frame in which motion of the center of mass is not considered because it is separable from the relative motion responsible in the collision. If the projectile ion has an intial momentum $\mathbf{p}_p = m_p\mathbf{v}_p$ and energy $E_p = \frac{1}{2}m_p|\mathbf{v}_p|^2$ and the target has a momentum $\mathbf{p}_t = m_t\mathbf{v}_t$ and energy $E_t = \frac{1}{2}m_t|\mathbf{v}_t|^2$ then it is simple to show that the collision energy is given by

$$E_c = \frac{m_t}{m_p + m_t}E_p + \frac{m_p}{m_p + m_t}E_t - \frac{1}{2}\frac{m_p m_t}{m_p + m_t}\mathbf{v}_p \cdot \mathbf{v_t}. \qquad (3.5)$$

Often it is assumed that $\mathbf{v}_p >> \mathbf{v}_t$ implying that $E_c \approx \frac{m_t}{m_t + m_p}E_p$. In the case that there is a distribution of projectiles and targets, this transformation takes the form of a convolution over the two distributions (Lifshitz et al., 1977). If the target distribution is taken to be a Boltzmann distribution in three dimensions, the resulting cross-section will take the form:

$$\sigma_{obs} = \frac{1}{\sqrt{\pi}}\int_0^\infty (\frac{1}{S^2 + 4E'/a})\exp[\frac{-(E_p - E')}{S^2 + 4E'/a}]\sigma(E')dE' \qquad (3.6)$$

where $a = \frac{m_t}{m_p k_B T}$ and S is the FWHM of the projectile distribution.

Alternatively, the velocity transformation to the center of mass frame can be expressed as an expected value of a convoluted distribution Nalley et al. (1973). This results in the transformation:

$$v_c \rightarrow v_c' = \int_0^\infty v_R F_R(v_R)dv_R$$

for

$$F_R(v_R) = \int_{-\infty}^\infty \frac{v_R}{\sqrt{\pi}vv_c}\{\exp[-\frac{(v_R - v_c)^2}{v_c^2}] - \exp[-\frac{(v_R + v_c)^2}{v_c^2}]\}F(v)dv \qquad (3.7)$$

where v_c is the mean of the projectile velocity distribution, $F(v)$, interpreted as the user set lab-frame collision energy.

49

3.4 Modeling

A group out of Switzerland has provided an alternative fitting procedure to the non-linear regression techniques described above. They term the entire modeling procedure *Ligand Collision Induced Dissociation* (LCID) (Narancic et al., 2007). As stated previously, almost all regression techniques require the provision of an objective function which is then minimized or maximized. In addition to the Gauss-Newton and Marquardt-Levenburg linear stepping approaches, quadratic stepping has been implemented. LCID utilizes a very robust genetic algorithm search to minimize the sum squares error. While this method is very successful, it fails to provide an approach to models with highly correlated parameters. A simplistic strategy can be implemented by forming a grid over the parameter space and evaluating the objective function at each grid point. Then, simply take the maximum or minimum value to be the best estimate. This overcomes the correlation problem when random stepping is used to search for the maximum, but the estimates are limited to the precision of the grid. Another alternative is provided below which arises from the Bayesian school of statistics.

The model by Armentrout *et al.* showed unusually high parameter estimate correlation between the parameters σ_0 and E_0. Given that E_0 is the threshold energy which is the parameter of interest, this is a most unsatisfactory result. This can be seen clearly by constructing a three dimensional contour plot of the negative log-likelihood versus each of these two parameters (Figure 3.4).

A "ridge" in this figure would demonstrate that there is high correlation between the two parameters given that there are a variety of different values which result in similar log-likelihoods. The point estimate of the fit parameters given by the frequentist fitting procedure results in only the highest likelihood point. The ridge in this case has some depth to it and thus there is a subset of parameters which forms a "plateau" of similar likelihood. While there is no single solution to every problem which involves highly correlated models, a more complete strategy is to form a large sample of the parameter space which follows the likelihood or posterior distribution. In this way the average of the Monte Carlo sample
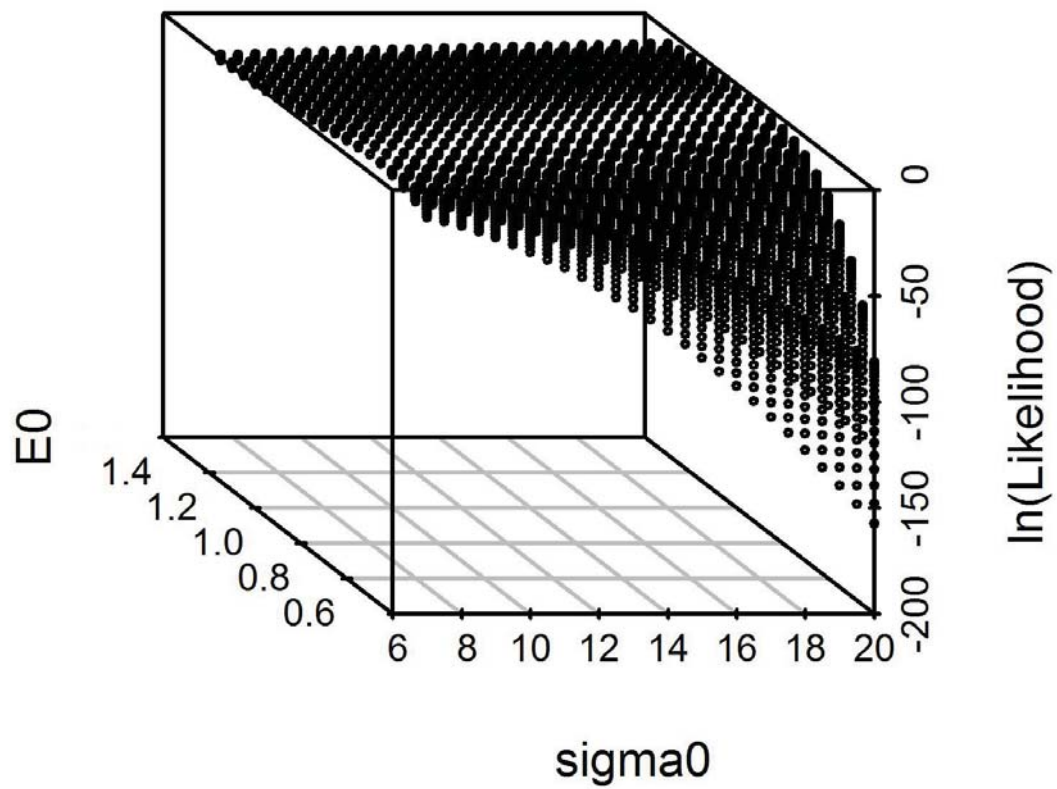
Figure 3.4: A plot of the log-likelihood versus the σ_0 and E_0 parameters. Notice the plateau of high likelihood formed due to parameter correlation.

will result in a posterior-weighted mean estimate of the parameters. A similar likelihood weighting technique has been demonstrated in simple linear regression which shows inherent correlation between the parameter estimates (Myers, 1986).

Once the collision energies were transformed through their velocities, the data could be fit according to the model

$$\sigma_j = \hat{\sigma}_j + \epsilon_j = \sigma_0 \sum_{i=1}^{M} g_i (E + E_i - E_0)^n / E + \epsilon_j \tag{3.8}$$

where it is assumed that the errors, ϵ_j, are identically and independently Normally distributed with a mean of zero and a precision of τ. The likelihood then takes the form

$$\mathscr{L}(\sigma | \mathbf{E}, \sigma_0, E_0, n) = (\frac{\tau}{2\pi})^{N/2} \exp(-\frac{\tau}{2} \sum_{j=1}^{N} (\sigma_j - \hat{\sigma}_j)^2). \tag{3.9}$$

Because each of the parameters loses physical interpretation if they are negative, the priors that were used in the analysis were given as

$$\tau \quad \sim \quad \Gamma(a, b) \tag{3.10}$$

$$\sigma_0 \quad \sim \quad Exp(c) \tag{3.11}$$

$$E_0 \quad \sim \quad truncN(d_1, e_1) \tag{3.12}$$

$$n \quad \sim \quad truncN(d_2, e_2) \tag{3.13}$$

where the parameters are chosen to reflect values given by a preliminary grid search for maximum likelihood. For example, the parameters d_1 and d_2 were chosen to be equal to the maximum likelihood point estimates for E_0 and n, respectively, as derived from the grid search. For the precision, the mean of a gamma distribution is given by ab which was set to equal the point estimate of the SSE at this grid search point estimate. The subjective parameter choices such as e_1 and e_2 were chosen so as to minimize the auto-correlation and inter-parameter correlation throughout the Markov Chain Monte Carlo simulation.
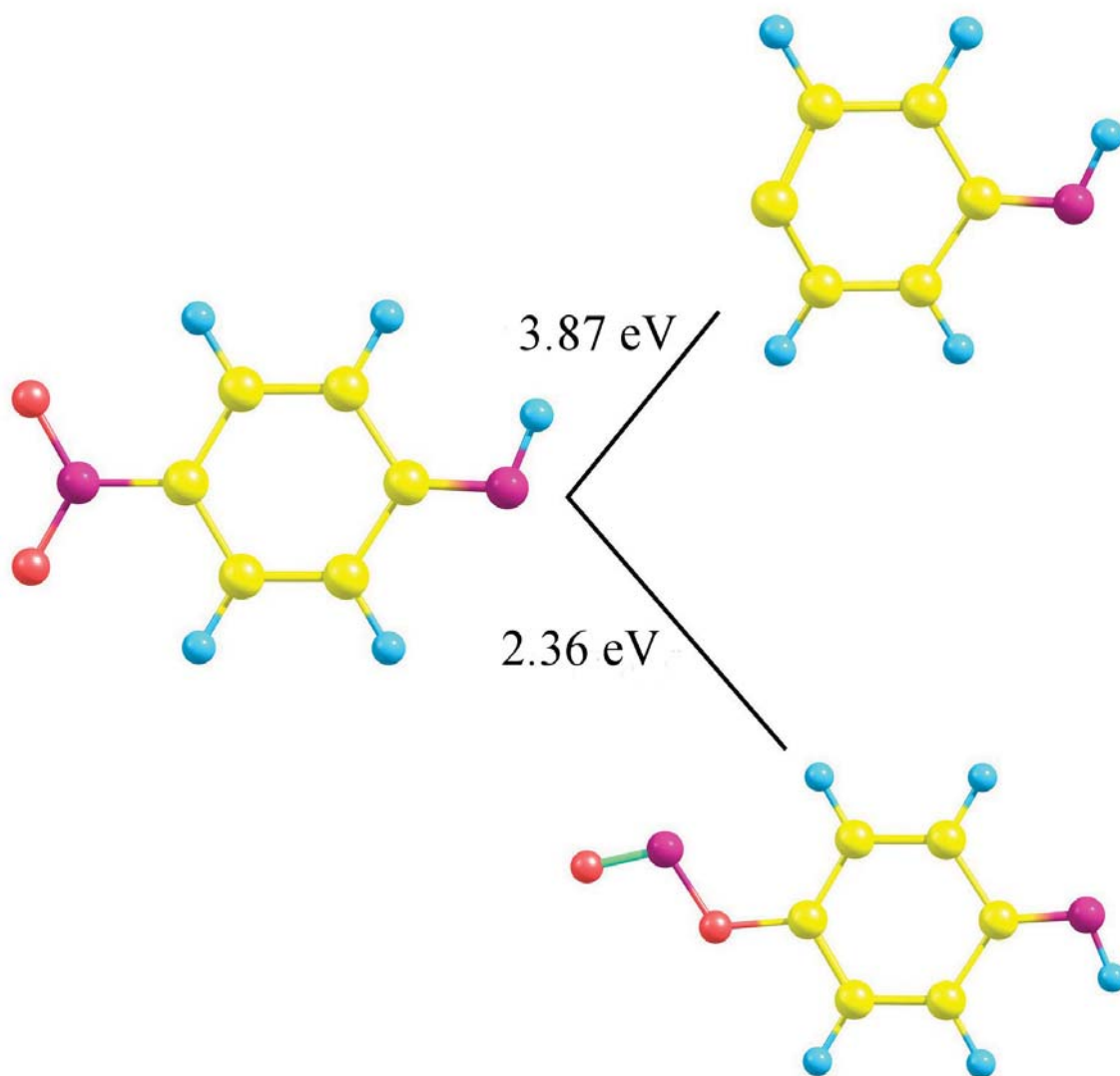
Figure 3.5: Fragments and transition states used in the the modeling of CID cross-sections.

Initially all values were drawn using the Metropolis-Hastings Algorithm utilizing a truncated Normal distribution as the random walking proposal distribution. This resulted in an unusually large correlation between the parameters (> 0.9 for each). In order to overcome this correlation, the precision hyperparameter, τ, and scaling factor, σ_0, were Gibbs sampled. This reduced the interparameter correlation to below 0.7 for each parameter pair. Finally, each Bayesian simulation was run with enough iterations (typically 150,000) to assure that the effective sample size for each parameter was over 1000 (Figures 3.6 and 3.7).

The assumption of Normally distributed residuals can be assessed graphically by superimposing a scaled Normal distribution on a histogram of the residuals. An example is given in the case of the collision induced dissociation of the tri-iodide molecule (Figure 3.8). It can be seen that there is a skew to the left side and that the centroid is over sampled. Furthermore, the assumption of independence can be examined graphically as well (Figure 3.9). Note that the residuals are not randomly distributed about a horizontal line, but rather oscillating with a large tail at higher energy.

Although the assumptions are violated in the strictest sense, the curve can be well-explained by the model. In this case, model misspecification likely drives the violation of the i.i.d. Normal assumptions. One source of error may lie in an underestimate of the collision cell pressure; higher cell pressures would result in multiple collisions. Furthermore, the Armentrout model asymptotically approaches infinity as energy increases which does not follow a real situation - at some point the collision energy will be so large that the parent is completely depleted and the first-order approximation to the Beer-Lambert Law.

In order to compare frequentist and Bayesian methodologies, the CRUNCH program developed by the Armentrout group was used (Armentrout et al., 2008; Ervin and Armentrout, 1985; Webe et al., 1986; Schultz et al., 1991; Dalleska et al., 1994; Rodgers et al., 1997; DeTuri and Ervin, 1998; Iceman and Armentrout, 2003; Su, 1994; Ervin, 1999; Koizumi and Armentrout, 2003; Koizumi et al., 2004; Amicangelo and Armentrout, 2001; Armentrout, 2007). It should be noted that the CRUNCH sofware includes weighting options during the fitting procedure. The default option is a "statistical" weighting scheme which
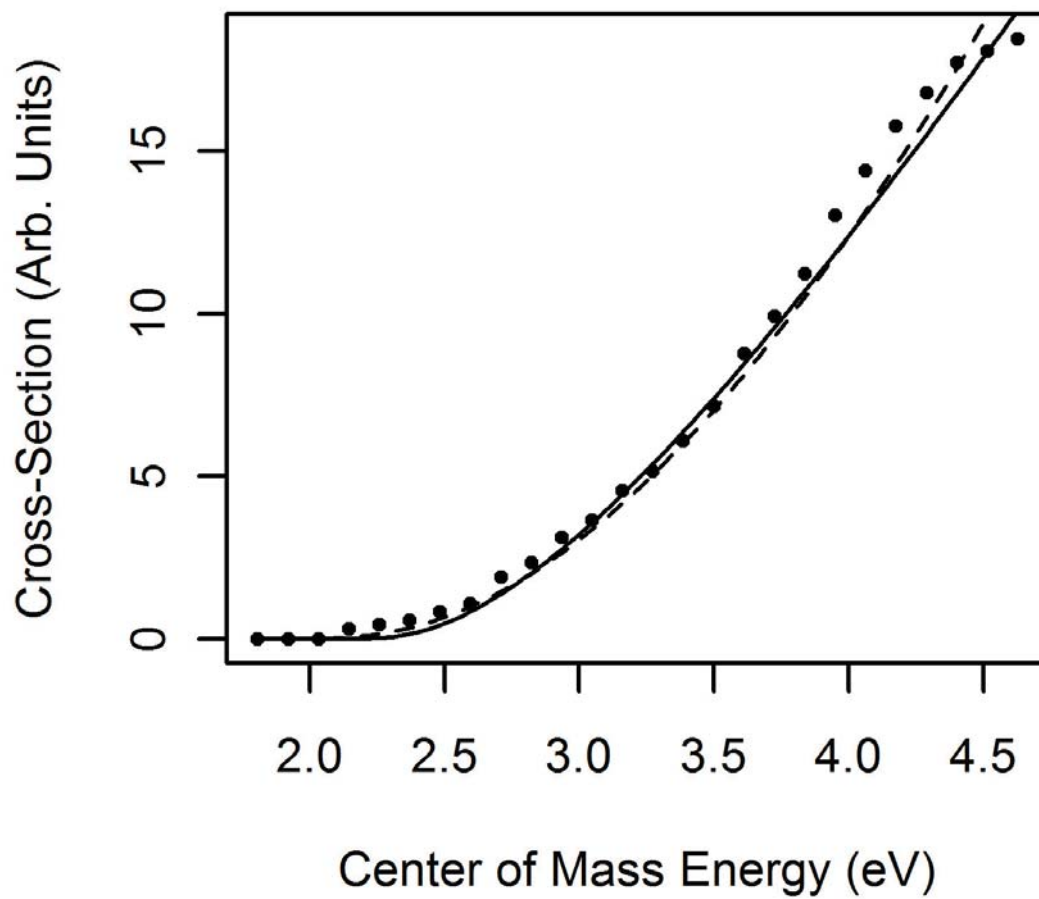
Figure 3.6: Non-linear fit of the first fragmentation peak. The fit given by CRUNCH is given as a dashed line.
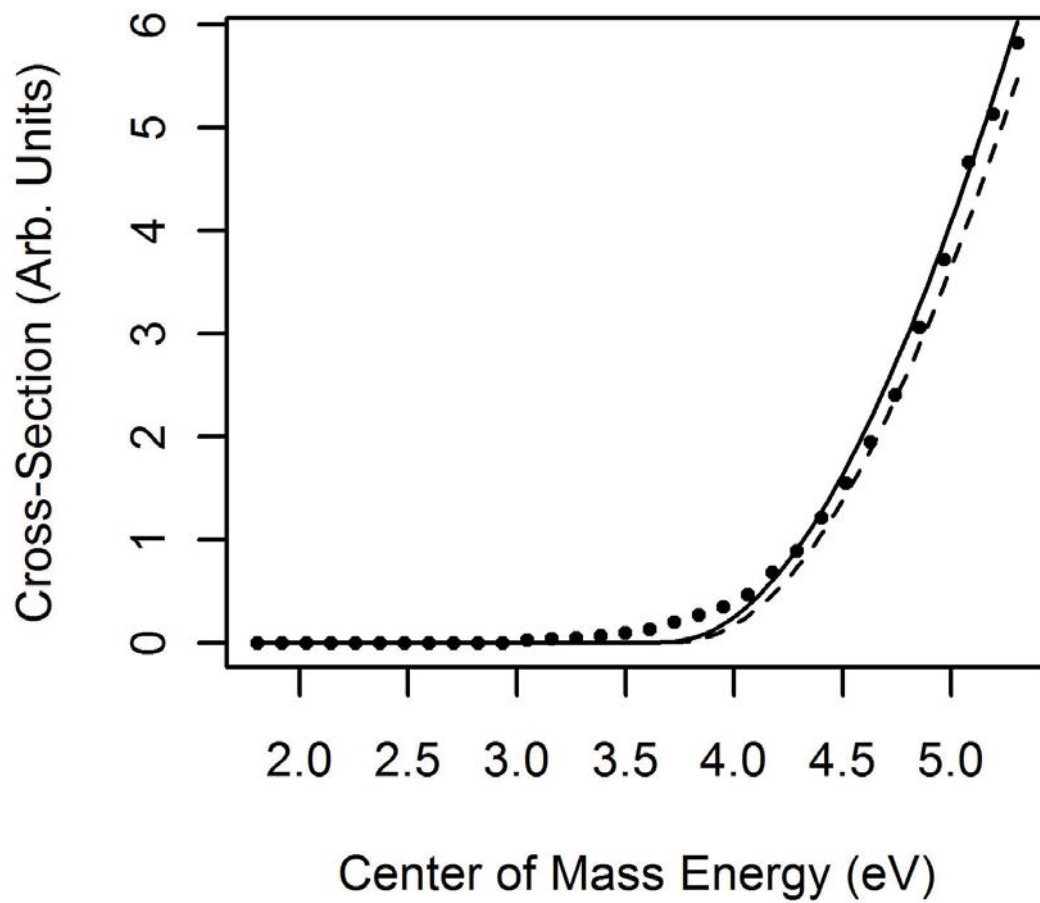
Figure 3.7: Non-linear fit of the second fragmentation peak. The fit given by CRUNCH is given as a dashed line.
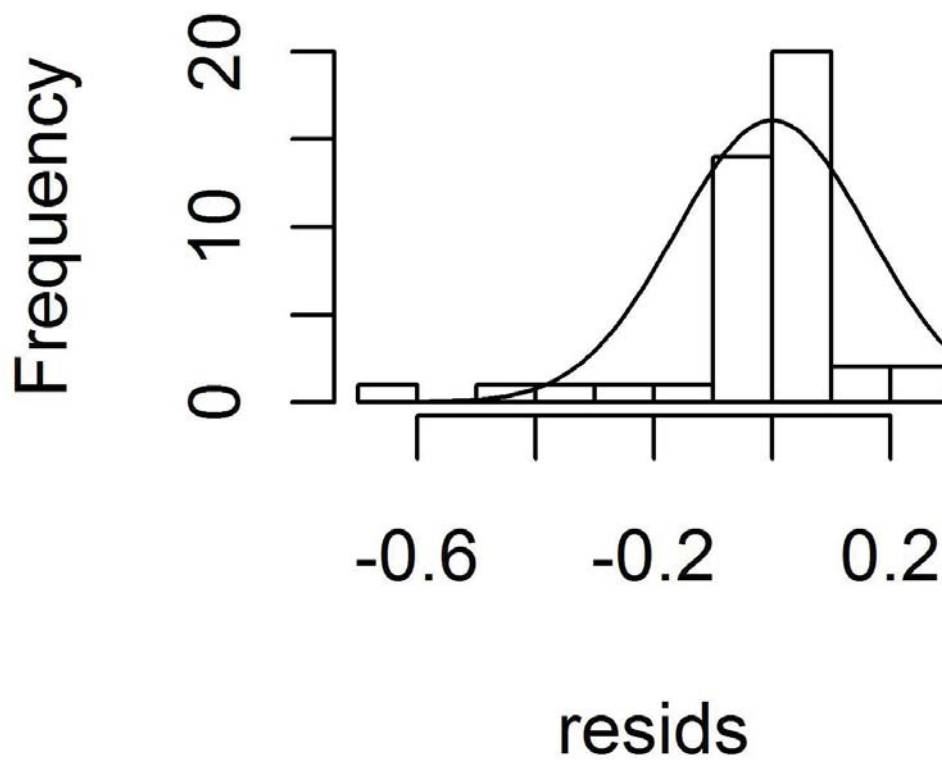
Figure 3.8: A histogram of the residuals of the fit with a superimposed Normal distribution.
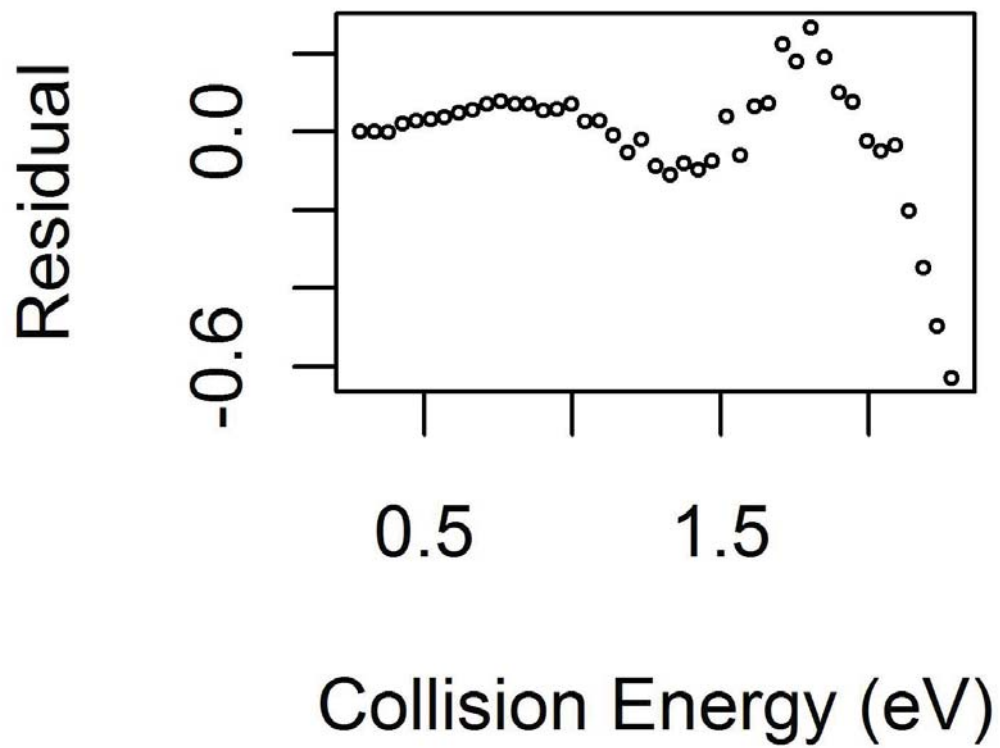
Figure 3.9: Residuals of the fit versus collision energy.

applies Gaussian weights to each term in the sum squares error, i.e.

$$\sum_{i=1}^{N}(\sigma_i - \hat{\sigma}(x_i))^2 \rightarrow \sum_{i=1}^{N}(\sigma_i - \hat{\sigma}(x_i))^2 e^{-x_i^2}. \tag{3.14}$$

Any weighting scheme can be adapted for use in Bayesian analysis by making a similar transformation in the likelihood function. The motivation to weight the errors in the modeling of collision induced dissociation comes partly from a desire to have a tight fit at low energy values so as to characterize the threshold completely. Nevertheless, this weighting is statistical only in name and does not seem to have any mathematical validity. Therefore these weights were not used in the modeling presented here.

Table 3.2: Comparison between CRUNCH and Bayesian fits

Dissociation Channel	Fit Method	σ_0	E_0	n	SSE
NO Loss	Bayesian MCMC	17.30	2.36	1.91	4.74
	CRUNCH	9.71	2.16	2.40	7.68
NO_2^- Loss	Bayesian MCMC	11.41	3.82	2.14	0.44
	CRUNCH	10.99	3.87	2.15	1.14

The error bars were easily accessible here by the 2.5% and 97.5% percentiles of the Monte Carlo sample. In addition, the correlation between σ_0 and E_0 may be estimated from the Markov Chain as 1.12. Despite the plethora of information that can be ascertained from a Markov Chain Monte Carlo simulation, several downsides exist; the most prevalent being the number of degrees of freedom available during the analysis.

3.5 Conclusion

In order to investigate the possibility of dipole-bound anions of pNA, we have used photoelectron spectroscopy of anions. Although no dipole-bound signal was seen, dipole-bound electronic states of pNA may act as "doorway" states which enable the molecule to attach slow electrons first through the dipole moment. The electrons would then cross potential energy surfaces in to a valence state.

Previous experiments (Desfrançois et al., 1999; Hammer et al., 2003, 1999; Gutsev and Adamowicz, 1995; Jr. et al., 1967; Lide, 1994; Defrançois et al., 1994) concerning the relationship between the dipole moment of organic molecules and the dipole-bound electron affinity result in the curve

$$EA_{dipole} = 0.0074\mu_{dip}^{5.3799}. \tag{3.15}$$

A visual compairson of dipole moment versus electron affinity for several organic molecules is given in Figure 3.10. Because pNA lies on the high end of this chart, it is likely to be an indicator of electron attachment to high dipole moments.

Additionally, we used the collision induced dissociation of the deprotonated pNA anions to investigate bonding within the molecule as well as introduce Bayesian methods to overcome inconsistencies in current modeling techniques. We find that with a complex model such as that given by the Armentrout group, instabilities in partial derivatives and inter-parameter correlation can be accounted for, at least partially, by a thorough Bayesian modeling.
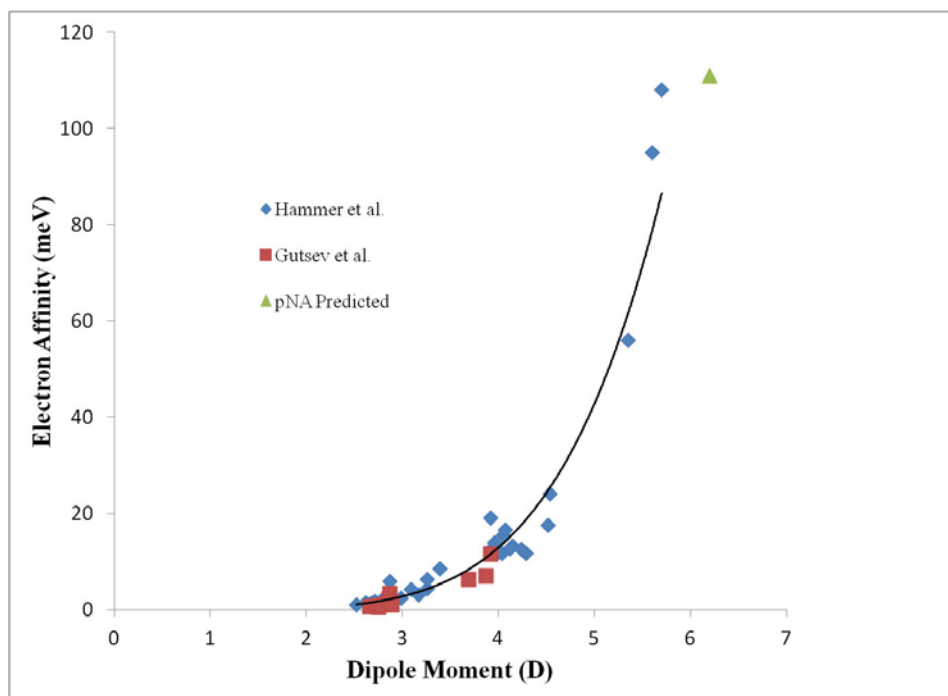
Figure 3.10: Dipole moment vs. electron affinity for several organic molecules.

Chapter 4

Multi-photon Ionization of TDAE

Although equations 2.11 and 2.12 provide a method to scan pass energies using an applied voltage on a plate to accelerate or decelerate charged particles, the radius of the pass surface must be empirically measured before the exact hemisphere voltages can be known. Furthermore, the existence of contact potentials between each of the analyzer components may affect the pass on each run. Initially the instrument was calibrated by using photoelectrons produced from the resonantly enhanced multi-photon ionization (REMPI) of Xenon. A basic introduction to multi-photon ionization (MPI) and REMPI is provided below.

4.1 Multi-photon Ionization and Resonantly Enhanced Multi-photon Ionization

A photoionization process can be defined by the excitation of an electron from a bound state of an atom or molecule into an unbounded continuum of states through the absorption of a photon. Quantum theory dictates that bound states of electrons take discrete energies; this can be shown mathematically through the solution of the Schrödinger Equation with the application of appropriate boundary conditions. In contrast, unbounded states exist in a continuum.

The formalism for multi-photon ionization developed here utilizes the interaction between light and atoms (rather than molecules) as a simple starting point; note that generalization to a molecule simply requires an expansion of the atomic Hamiltonian to include other nuclei. On the scale of atomic physics, a nucleus is treated as a stationary, central charge surrounded by N electrons. The Hamiltonian is then given by the sum of the electron kinetic energies, electrostatic attractive potentials between the electrons and the nucleus, and the repulsive potentials from the interaction between electrons:

$$\hat{H}_A = \sum_{i=1}^{N} \left(\frac{\hat{\mathbf{p}}_i^2}{2\mu} + \frac{e^2}{|\mathbf{r}_i|} \right) - 2 \sum_{i=1}^{N} \sum_{j>i} \frac{e^2}{|\mathbf{r}_i - \mathbf{r}_j|} \tag{4.1}$$

where μ is the reduced mass and $\mathbf{r}_i$ and $\mathbf{p}_i$ are the position and momentum of the ith electron respectively.

Light is often described classically with a continuous plane wave, but a complete description of an electromagnetic wave interacting with an atom or molecule requires the field to be discretized. This is done by first noting that energy in an electromagnetic field is quantized as photons. Instead of focusing on the total energy stored in the field, focus is given to the number of photons n_λ of a given mode, λ. This paradigm is referred to as *Second Quantization*. To do so, first consider how the presence of an electromagnetic field affects states of an atom. Light is typically treated as an instantaneous constant field defined by the magnetic vector potential $\mathbf{A}$ and the electric scalar potential Φ:

$$\mathbf{E} = -\nabla\Phi - \frac{1}{c}\frac{\partial \mathbf{A}}{\partial t} \tag{4.2}$$

$$\mathbf{B} = \nabla \times \mathbf{A} \tag{4.3}$$

where c is the speed of light in vacuum, $c = 2.9979 \times 10^8$ m/s. Given any three-dimensional space, a plane electromagnetic wave can be defined with a polarization (direction of the electric field) π_λ perpendicular propagation direction $\mathbf{k}_\lambda$ such that $\pi_\lambda \cdot \mathbf{k}_\lambda = 0$.

The vector potential can then be expanded as a superposition of plane waves

$$\mathbf{A}(\mathbf{r}, t) = \sum_\lambda (q_\lambda \mathbf{A}_\lambda e^{-i\omega t} + q_\lambda^* \mathbf{A}_\lambda^* e^{i\omega t}). \tag{4.4}$$

Plugging this into equations 4.2 and 4.3 give that

$$\mathbf{E} = \frac{i}{c} \sum_\lambda \omega_\lambda (q_\lambda \mathbf{A}_\lambda e^{-i\omega t} + q_\lambda^* \mathbf{A}_\lambda^* e^{i\omega t}) \tag{4.5}$$

$$\mathbf{B} = i \sum_\lambda \mathbf{k}_\lambda \times q_\lambda \mathbf{A}_\lambda e^{-i\omega t} + q_\lambda^* \mathbf{A}_\lambda^* e^{i\omega t}).$$

The total energy in the field is then given by

$$\epsilon = \frac{1}{8\pi} \int_{L^3} d^3\mathbf{r}(\mathbf{E}^2 + \mathbf{B}^2) = \frac{1}{2\pi c^3} \sum_\lambda \omega_\lambda^2 q_\lambda^* q_\lambda \tag{4.6}$$

In order to describe the interaction of an atom with light, a total Hamiltonian which contains information about the atom and the light is used. Incorporating these fields into the Hamiltonian changes the kinetic and potential energies as:

$$\hat{T} \rightarrow \hat{T}' = \sum_{i=1}^{N} \frac{(\hat{\mathbf{p}}_i + \frac{e}{c}\mathbf{A}(\mathbf{r}_i, t))^2}{2\mu} \tag{4.7}$$

$$\hat{V} \rightarrow \hat{V}' = \sum_{i=1}^{N} -e\Phi(\mathbf{r_i}, t) + \hat{V} \tag{4.8}$$

It is easily seen that the eigenstates of the total Hamiltonian may not be the same as those of the atom-only Hamiltonian, $\hat{H}_A$. Expanding the resulting Hamiltonian results in two identifiable parts: One Hamiltonian which consists of the independent components associated with the target atom and the field $\hat{H}_0$ and one Hamiltonian associated with the interaction

between the atom and the field $\hat{W}$ given by

$$\hat{H}_0 = \sum_{i=1}^{N} \frac{\hat{\mathbf{p}}_i^2}{2\mu} + \frac{e^2}{2\mu c^2} \sum_{i=1}^{N} \mathbf{A}(\mathbf{r}_i, t)^2 - e \sum_{i=1}^{N} \Phi(\mathbf{r}_i, t) + \hat{V} \tag{4.9}$$

$$\hat{W} = \frac{e}{2\mu c} \sum_{i=1}^{N} [\hat{\mathbf{p}}_i \cdot \mathbf{A}(\mathbf{r}_i, t) + \mathbf{A}(\mathbf{r}, t) \cdot \hat{\mathbf{p}}_i]. \tag{4.10}$$

such that $\hat{H} = \hat{H}_0 + \hat{W}$.

This can then be treated with perturbation theory where $\hat{W}$ is taken to be a perturbation. Doing so will result in a photoionization cross-section of

$$\sigma_{ph}(E) = 4\pi^2 \frac{e^2}{c} \omega_\lambda |\pi_\lambda \cdot \mathbf{r}_{fi}|^2 \tag{4.11}$$

where π_λ is the light polarization (Friedrich, 2006). In the case of multiphoton absorption from a laser, one can again use perturbation theory to arrive at a ionization probability proportional to the intensity of the light source to the power of the ionization order. In other words, the ionization for an n photon process is given by

$$P(n) \propto I^n. \tag{4.12}$$

In practice, a photoelectron spectrum (or in this case the spectrum of a cation) will often show three prominent features: A peak corresponding to vertical ionization, a peak corresponding to adiabatic ionization, and several peaks in between corresponding to Franck-Condon overlap of vibrationally excited states of the out-going cation. Thus, in a series of peaks plotted as the intensity of an electron or ion signal versus the energy of the electron or ion, the location of the highest energy peak is interpreted as the adiabatic IP. The position of the maximum peak is interpreted as the vertical ionization potential because vertical ionization has the largest Franck-Condon overlap and is therefore the most probable event.

Any additional peaks in a PES may be attributed to ionization from an excited state of the neutral or ionization of the ground state of the neutral resulting in an excited state of

the cation. These are so called "hot-bands." The amplitude of hot-band peaks are variable and depend directly on the Franck-Condon overlap of the intial and final states.

Supplementary information can be gained from photoelectron spectroscopy if the polarization of incident light is controlled. In a hemispherical energy analyzer the relatively small acceptance solid angle located directly below the ionization region defines an axis. Light incident perpendicularly then defines a plane of interaction. The polarization can then be parallel to this plane (vertical), perpendicular (horizontal), or some linear combintation of the two (at some angle θ relative to the plane of interaction).

The amplitude of a photoelectron peak will change with the polarization. This change can then be used to directly measure the order of the ionization N (that is, the number of photons used to ionize) (Cooper and Zare, 1968):

$$I = \frac{\sigma_{tot}}{4\pi} \sum_{n=0}^{N} a_n cos^{2n}\theta. \tag{4.13}$$

Also, if the ionization is of first order, the *Anisotropy Parameter*, β, may be defined as

$$I = \frac{\sigma_{tot}}{4\pi}[1 + \beta P_2(\cos\theta)] \tag{4.14}$$

where σ_{tot} is the total ionization cross-section and $P_2(\cos\theta) = \frac{3}{2}\cos^2\theta - \frac{1}{2}$ is the second order Legendre Polynomial. The distribution formed by the rotation of light's polarization is called the *Photoangular Distribution* (PAD).

4.2 REMPI of Xenon

In order to calibrate the instrument, photoelectrons resulting from the resonantly enhanced multi-photon ionization of Xenon were used. In contrast to direct multi-photon ionization (MPI), REMPI allows for an effective reduction in the order of the ionization process due to a coupling of a portion of the photons involved in the process to a well-defined excited

state. This process has been thoroughly outlined in Xenon (Compton et al., 1980; Miller and Compton, 1982).

In this instance a 3+2 ionization process was used to produce photoelectrons. In atomic states, the energy spacing between spin states allows for the resolution of the fine structure. Utilizing 440.88 nm allows for the probing of the 6s state of Xenon with three photons. Subsequent ionization occurs through two different 2p states ($2p_{3/2}$ and $2p_{1/2}$) of the xenon cation. These states are separated by 1.306 eV with energies of 0.66 eV and 1.966 eV for the $2p_{3/2}$ and $2p_{1/2}$ states respectively. Given this well documented energy spread, the photoelectron spectrum may then be used to calibrate the instrument for electrons which may lie between these two values.

4.3   Multi-Photon Ionization of TDAE

The study of low ionization potential (IP) molecules has grown in recent decades due to the discovery of a series of different applications in research and industry. Because the energy required to strip an electron from a molecule is low, an abundance of charge can be loacalized efficiently through the application of relatively low laser intensities to such molecules. This is seen no more clearly than in the field of plasmonics in which the creation of high charge densities (between 10^{11} and 10^{13} charges per cm^3) is directly utilized. Low IP molecules can be used to generate such plasmas when illuminated with UV (laser) light (Woodwort et al., 1985; Anderson, 1981; Zhang and Scharer, 1993; Kelly et al., 2002).

Low IP molecules have also been implemented in ultraviolet photomultiplier tubes. Again, the UV light will directly ionize such molecules, creating a free charge which can then be used to create a measurable signal. This technique is used widely in medical fields (x-rays, etc.). Additionally, low IP molecules can be utilized in organic electronics due to their ability to lower the work function of metals (Linderr et al., 2008).

The IP of most organic compounds is in the range of 7 to 12 eV (Mirsaleh-Kohan et al., 2011). On the contrary, a few organic molecules have been shown to violate this; of particular
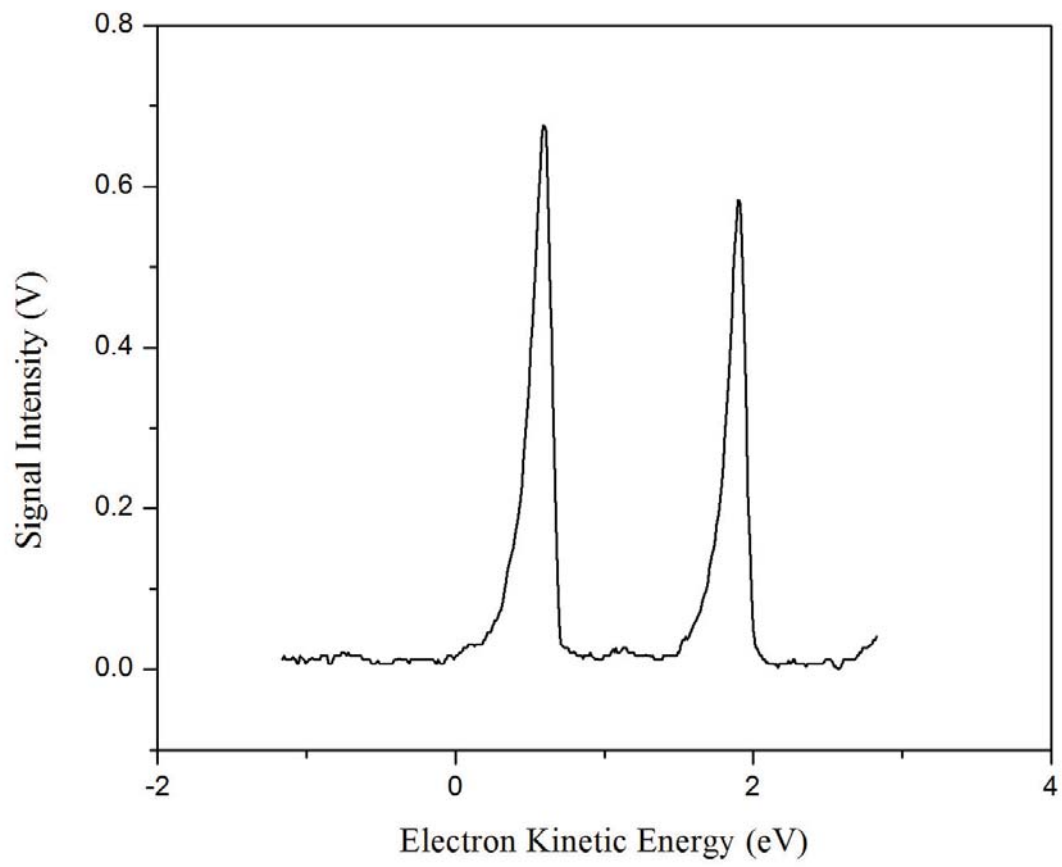
Figure 4.1: Photoelectron spectrum of Xenon resulting in peaks at 0.66 eV and 1.966 eV.

interest is tetrakis(dimethylamino)ethylene which has one of the lowest gas-phase adiabatic IPs for a molecule between 5.2 eV and 5.4 eV 4.2.

The first measurement of the ionization potential of TDAE was performed in 1971 by Cetinkaya *et al.* (Centinkaya et al., 1971). This was done using a single-photon ionization with a far UV, He(I) lamp. The resultant photoionization showed several peaks corresponding to further ionization processes (excitation and ionization). Because high energy photons were implemented in this study, this value is taken to be the vertical ionization potential.

Less than a year after this measurement, Nakato *et al.* measured the appearance spectrum of TDAE$^+$ cations under different photon energies (Nakato et al., 1972). In the case of appearance spectroscopy, the onset of cation signal is interpreted as the adiabatic IP. In addition, the vertical IP can be garnered from the data as a maximum of the derivative of the interaction cross-section with respect to photon energy. In this way a measurement of 5.36 eV and 6.11 eV for the adiabatic and vertical IP of TDAE were recorded. The quantum defect (difference between the two IPs) is then given approximately by 0.7 eV which is indicative of a large geometry change during the ionization process. This notion is seconded by the slow onset of the cation signal which would suggest poor Franck-Condon overlap between the ground state of the neutral molecule and the ground state of the cation. A slow onset may also be due to ionization of excited neutral molecules whose states are poorly populated, creating an underestimate of the adiabatic IP. In TDAE this was ruled out later through the use of a variety of seed gasses in the sample introduction process as each separate gas would give rise to a different appearance spectrum (Mirsaleh-Kohan et al., 2011).

Another interesting characteristic of TDAE is the production of chemilumiscence when reacted with oxygen. This was first shown by Pruett *et al.* who recorded the first synthesis of the molecule (Pruett et al., 1950). This reaction results in the production of excited states of tetramethyloxamide and tetramethylurea which subsequently fluoresce (Wiberg and Bulcher, 1964). This particular reaction is not typical of many ethylene derivatives, but may be attributed to the strong electron-donor characteristic of TDAE (Wiberg and Bulcher,
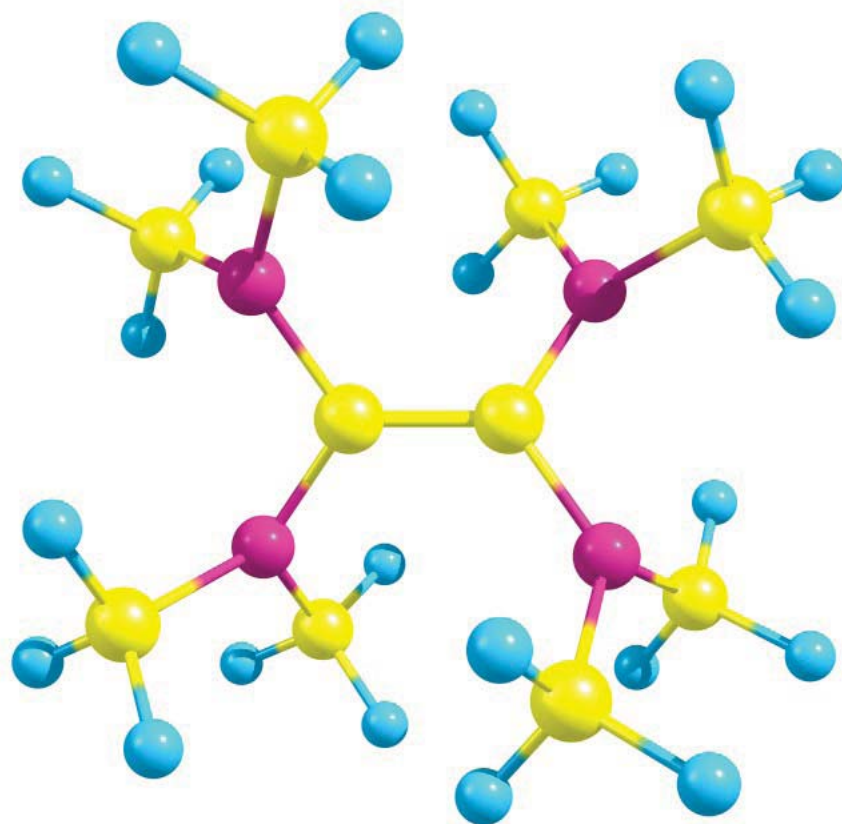
Figure 4.2: Molecular structure of tetrakis(dimethylamino)ethylene.

1962). Following this observation, the absorption spectrum of TDAE was investigated using light between 170 nm and 300 nm (Hori et al., 1968). This absorption spectrum showed an unusually large and broad absorption spectrum, peaked at 190 nm. In addition, the emission spectrum was recorded which was peaked at 480 nm. The large energy difference between the peak of the absorption spectrum (6.53 eV) and the emission spectrum (2.58 eV) is unusual for any molecule. Nevertheless, the authors attributed this emission to fluorescence due to a time scale on the order of 20 to 30 ns. Typically this derives from the existence of an intermediate state with a charge-transfer (CT) characteristic. Given that the geometry of the CT state is greatly distorted in comparison to the ground state of the molecule, the energy deficit goes in to the severing and rearrangement of bonds.

A femtosecond pump-probe study of TDAE has shown that there is a more complicated dynamic than just the excistence of a CT state, a dark zwitterionic (Z) state also exists within the molecule (Soep et al., 2001). This state is a doubly excited intermediate which lies slightly above the CT state in energy. The potential energy surfaces of these two states are joined via conical intersection which in turn leads to very short state occupation lifetimes ($\sim$ 300 fs). Such intersetctions have been implemented succesfully in the study of non-adiabatic coupling of excited state wave functions (Jortner et al., 1969). An electron "traveling" on such an intersection will relax by geometry change and is thus radiationless.

The origin of these two states lies in the degenerate positions of the free electrons bound to the four nitrogen atoms. The combination of which produces a superposition of two resonant structures. The energy degeneracy is then broken by considering the resonant structures in phase (Z state) and out of phase (CT state). The CT state is strongly distorted in comparison to the ground state of TDAE due to the disruption of the ethylene bond. Free rotation of the two sides of the molecule result in a twisted excited state.

Photoexcitation of the TDAE molecule can then be described on three time scales: An initial excitation to a excited state which is a super position of the molecule's Rydberg series and the $\pi\pi^*$ valence band. This decays to the Z state rapidly ($\sim$ 300 fs). The Z state then degrades to the CT state within picoseconds via the aforementioned conical intersections. The molecule then fluoresces on the nanosecond time scale to return to the ground state.
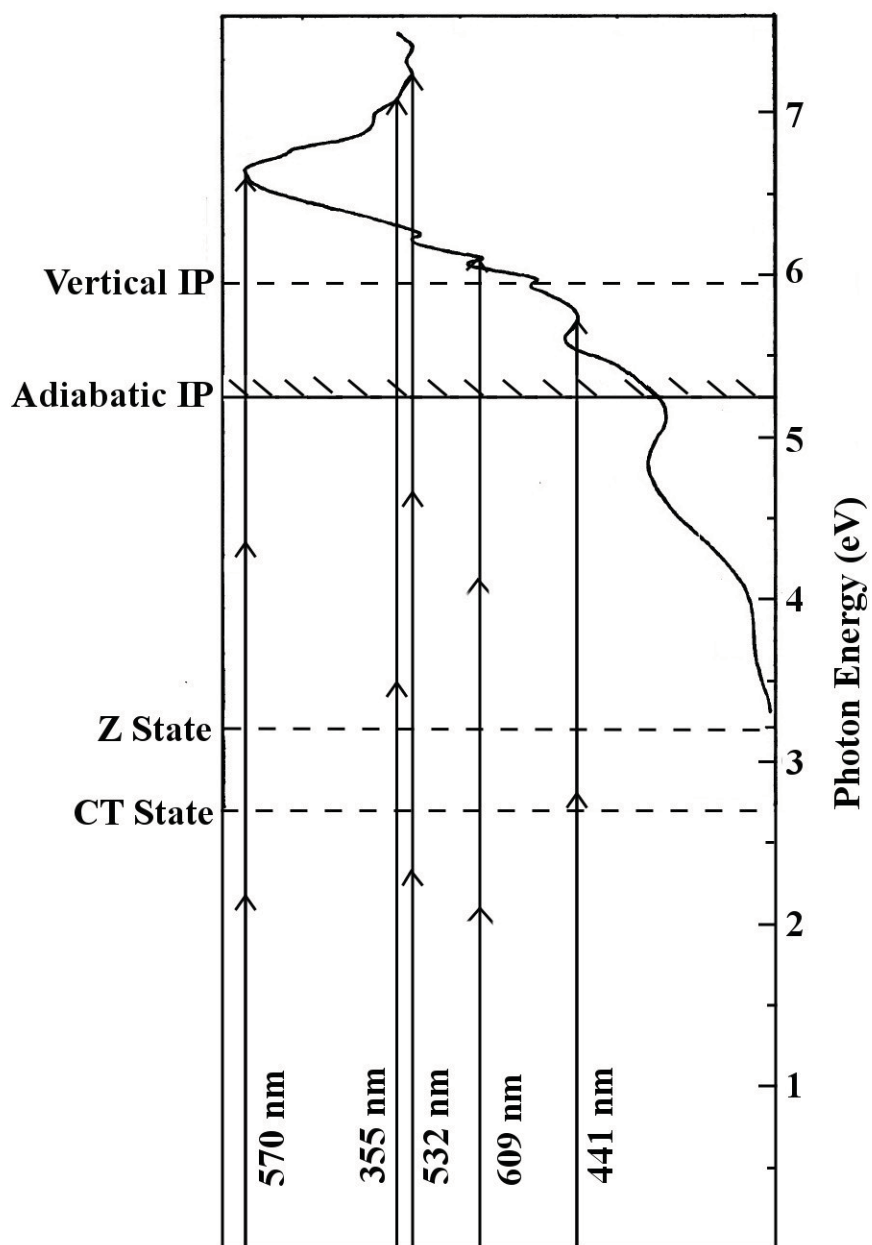
Figure 4.3: Absorption curve of TDAE with several photon wavelengths superimposed on the curve.

In order to explore transient states in tetrakis, laser light at 355 nm (3.49 eV), 440.88 nm (2.81 eV), 532 nm (2.33 eV), 570 nm (2.18 eV), and 609 nm (2.04 eV). Each of these wavelengths were generated either as a harmonic of an Nd:YAG laser (Continuum Powerlite Precision 9000), or as the output of a pumped dye laser (Quantaray PDL-1E). These wavelengths were chosen to comprehensively explore the absorption curve as well as characterize each of the transient states (Figure 4.3).

Ionization was carried out with 440.88 nm light immediately following the intrument calibration with xenon. Ionization was also carried out with 355 nm laser light, generated as the third harmonic of the Nd:YAG laser as well as 570 nm and 609 nm light produced from pumping a dye laser with the second harmonic of the Nd:YAG laser (532 nm). These wavelengths were chosen in order to comprehensively characterize the absorption curve given multiple photon absorption. In the case of the ionization of TDAE with 355 nm and 440.88 nm light, the molecule is ionized in a 1+1 photon process with an initial one photon excitation to a mixed transient state prior to a relaxation through the Z state to the CT state. Electrons are then ejected from this charge transfer fluorescent state.

Utilizing 440.88 nm light results in two peaks; one peak arises as auto-ionization while the other peak is due to adiabatic ionization from the CT state (Figure 4.4). The first of these peaks is centered at 0 eV while the latter is centered at 0.3 eV. Ionization with 355 nm light produces two peaks as well. Again, one is attributed to auto-ionization, centered at 0 eV while the other peak is centered at 1.0 eV (Figure 4.5). Although a direct two photon ionization from the ground state using 440.88 nm light should result in electrons produced with 0.3 eV kinetic energy, a difference of 0.7 eV between the ionizing peaks gives strong evidence for the 1+1 ionizing scheme. Further evidence is presented in the PADs under each ionizing wavelength.

The PADs of TDAE under illumination with both wavelengths were recorded using a double Fresnel rhomb to rotate the polarization of light in steps of 10 degrees. Because the collected data was noisy, each PAD is an average over four scans from 0 to 180 degrees. Both the ionizing peak and the thermal peak were investigated here under ionization with each wavelength. The ionizaing peak PAD of TDAE using both wavelengths give strong evidence
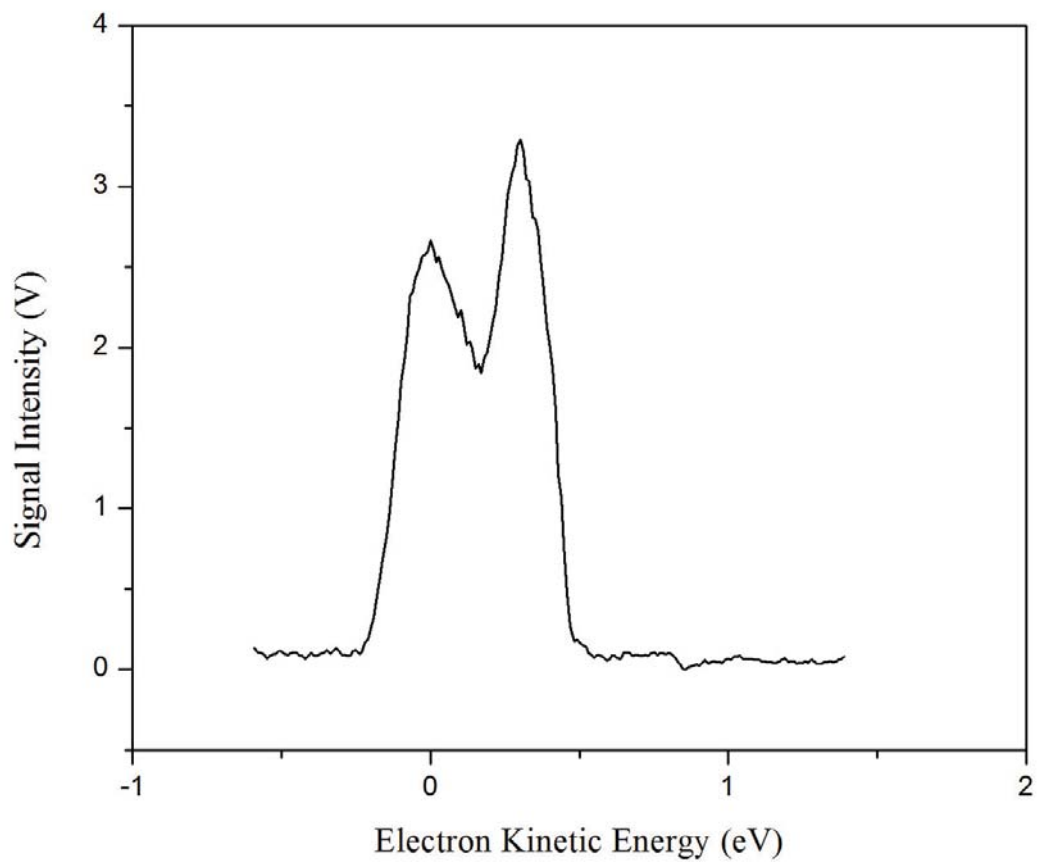
Figure 4.4: Photoelectron spectrum of TDAE using 441 nm light. Signal is peaked at ~ 0 eV and 0.3 eV.
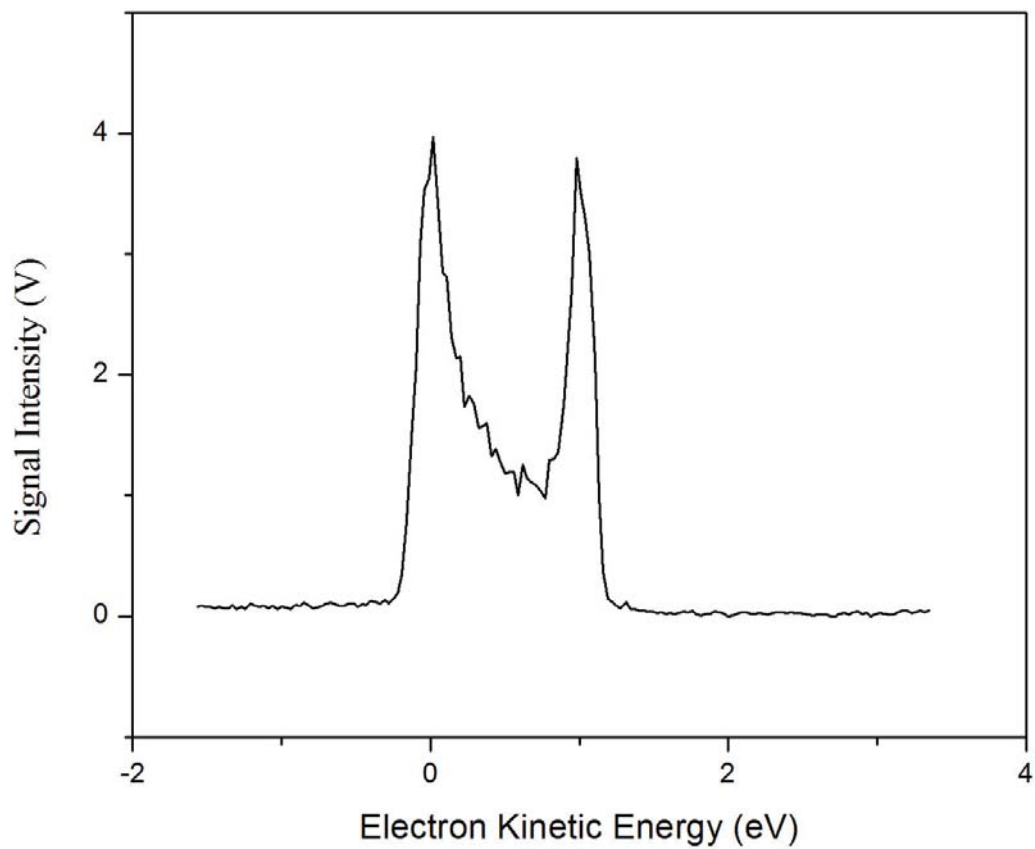
Figure 4.5: Photoelectron spectrum of TDAE using 355 nm light. Signal is peaked at ~ 0 eV and 1.0 eV.
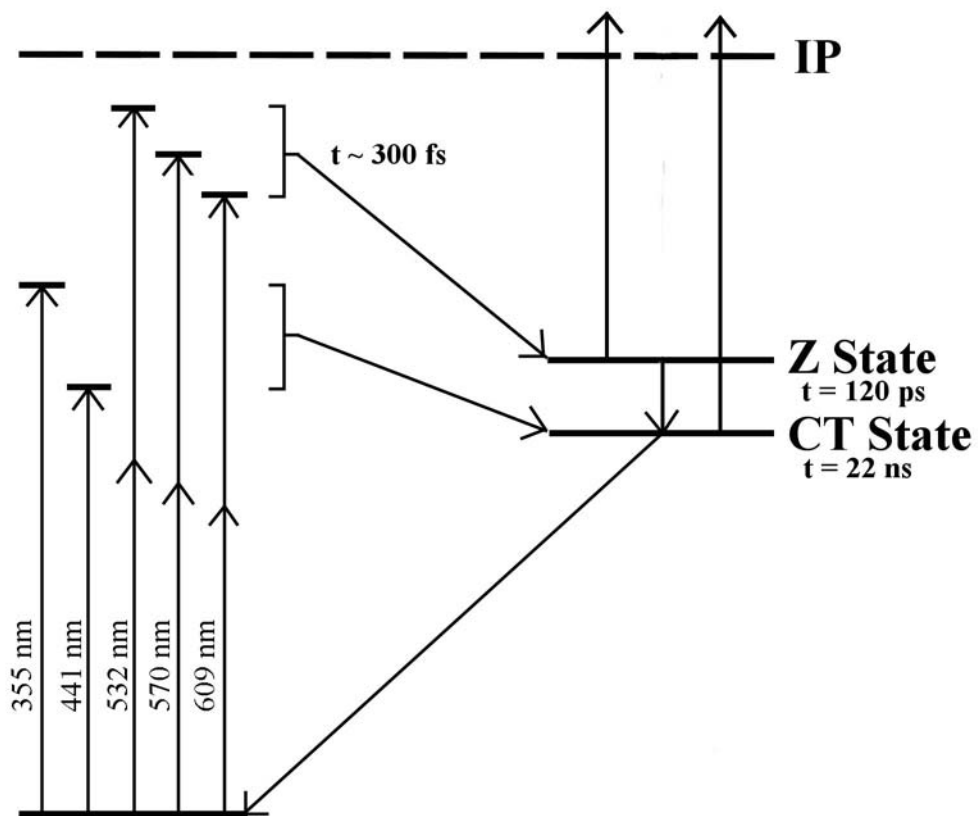
Figure 4.6: Energy level diagram with transient state lifetimes.

for one-photon ionization. In order to asses the order of ionizaition, each PAD was fit using simple linear regression (Table 4.1).

Note that in each case there is a very slight drift in amplitude through the angle (the signal should be precisely the same at 0 degrees and 180 degrees). This is likely due to imperfections in the optics and alignment. For example, if the laser light is not normally incident on the Fresnel rhomb, the laser power at 0 degrees and 180 degrees will be different. The effect of such a drift can be quantified by including a linear term in the regression, that is,

$$I = \frac{\sigma_{tot}}{4\pi} (b\theta + \sum_{n=1}^{N} a_n \cos^n \theta).$$

In each case this parameter is slightly significant and does not change the conclusion. One noticeable effect upon inclusion of this linear term is an increase of the significance of the sinusoidal terms. The coefficient of the second order ionization (a_4) is slightly significant in each case but does not change the fit visibly (Tables 4.2 and 4.3).

Table 4.1: Photo-angular distributions at different laser wavelengths.

Wavelength (nm)	Peak Location (eV)	β	R^2
441	~ 0	0.11	0.948
	0.3 eV	0.61	0.988
355	~ 0	0.03	0.899
	1.0	0.24	0.993
609	~ 0	0.49	0.975
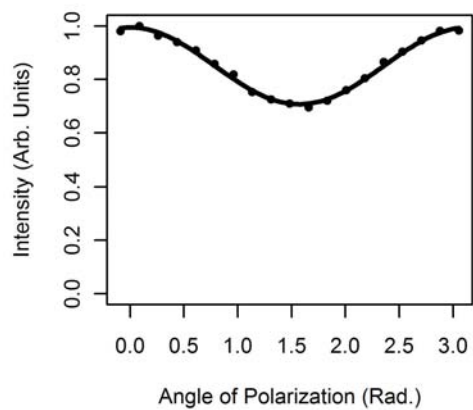
(a) PAD of ionizing peak
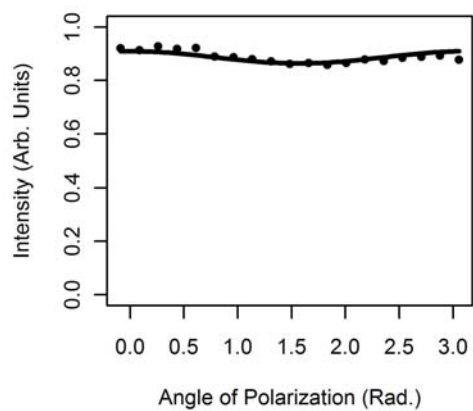
(b) PAD of thermal peak

Figure 4.7: Photo-angular distributions using 355 nm light.
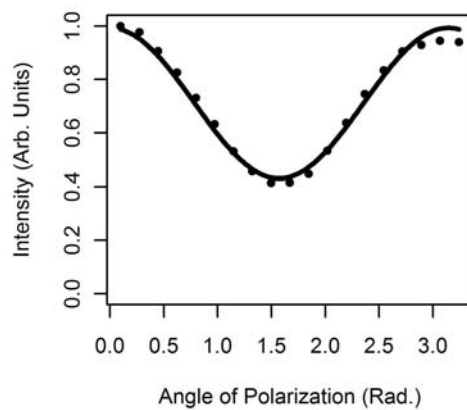
(a) PAD of ionizing peak
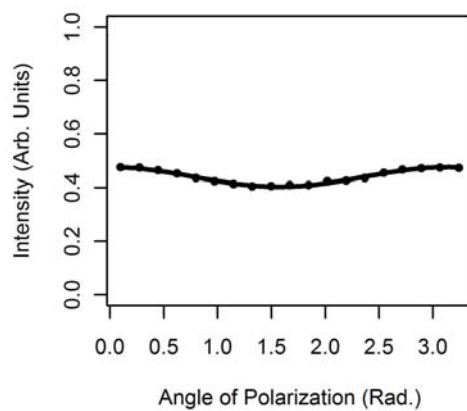
(b) PAD of thermal peak

Figure 4.8: Photo-angular distributions using 441 nm light.

Table 4.2: Different fits to photo-angular distributions of the ionizing peak using 441 nm laser light.

	Model	SSE	p-value
1 Photon Model	$12.69 + 16.59 \cos^2 \theta$	0.7483	$< 2e - 16$
With Linear Addition	$13.37 - 0.46\theta + 16.75 \cos^2 \theta$	0.6045	$< 2e - 16$
2 Photon Model	$11.89 + 22.8476 \cos^2 \theta - 6.13 \cos^4 \theta$	0.4880	$8.35e - 12$

Table 4.3: Different fits to photo-angular distributions of the ionizing peak using 335 nm laser light.

	Model	SSE	p-value
1 Photon Model	$37.62 + 15.30 \cos^2 \theta$	0.4895	$< 2e - 16$
With Linear Addition	$37.53 + 0.06\theta + 15.32 \cos^2 \theta$	0.5012	$< 2e - 16$
2 Photon Model	$31.17 + 18.89 \cos^2 \theta - 3.51 \cos^4 \theta$	0.3704	$2.22e - 12$

Photoionization with 609 nm (2.04 eV) light produced a single peak at approximately 0 eV. In the case of the two previous wavelengths, one would be led to believe that this peak is attributed only to an auto-ionizing state. Upon closer inspection there is a reproducible dip in the spectrum which would suggest that there are likely two ionization channels which largely overlap at this energy. This ascertion may be exemplified by the PAD which shows an unusually strong anisotropy ($\beta = 0.49$) again with only a one photon character.

Located approximately 2 eV below the ionization limit of TDAE is the zwitterionic state; the energy surplus would then result in 40 meV electrons. Because the typical FWHM of the photoelectron peaks is above 100 meV, these peaks cannot be distinguished. Another likely candidate for this peak arises from a three photon vertical ionization of TDAE which has a measured vertical IP between 5.95 eV and 6.11 eV (Centinkaya et al., 1971; Nakato et al., 1972). In this case the electrons would have kinetic energies between 0.01 eV and
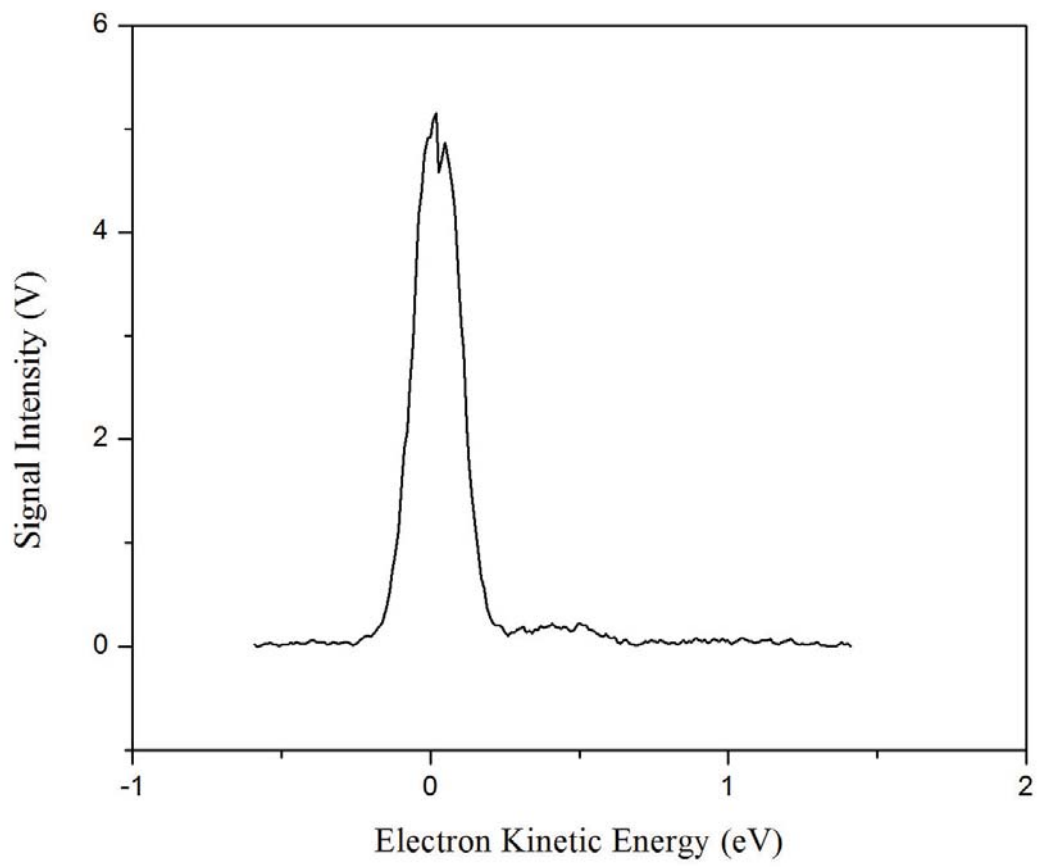
Figure 4.9: Photoelectron spectrum of TDAE using 609 nm light.
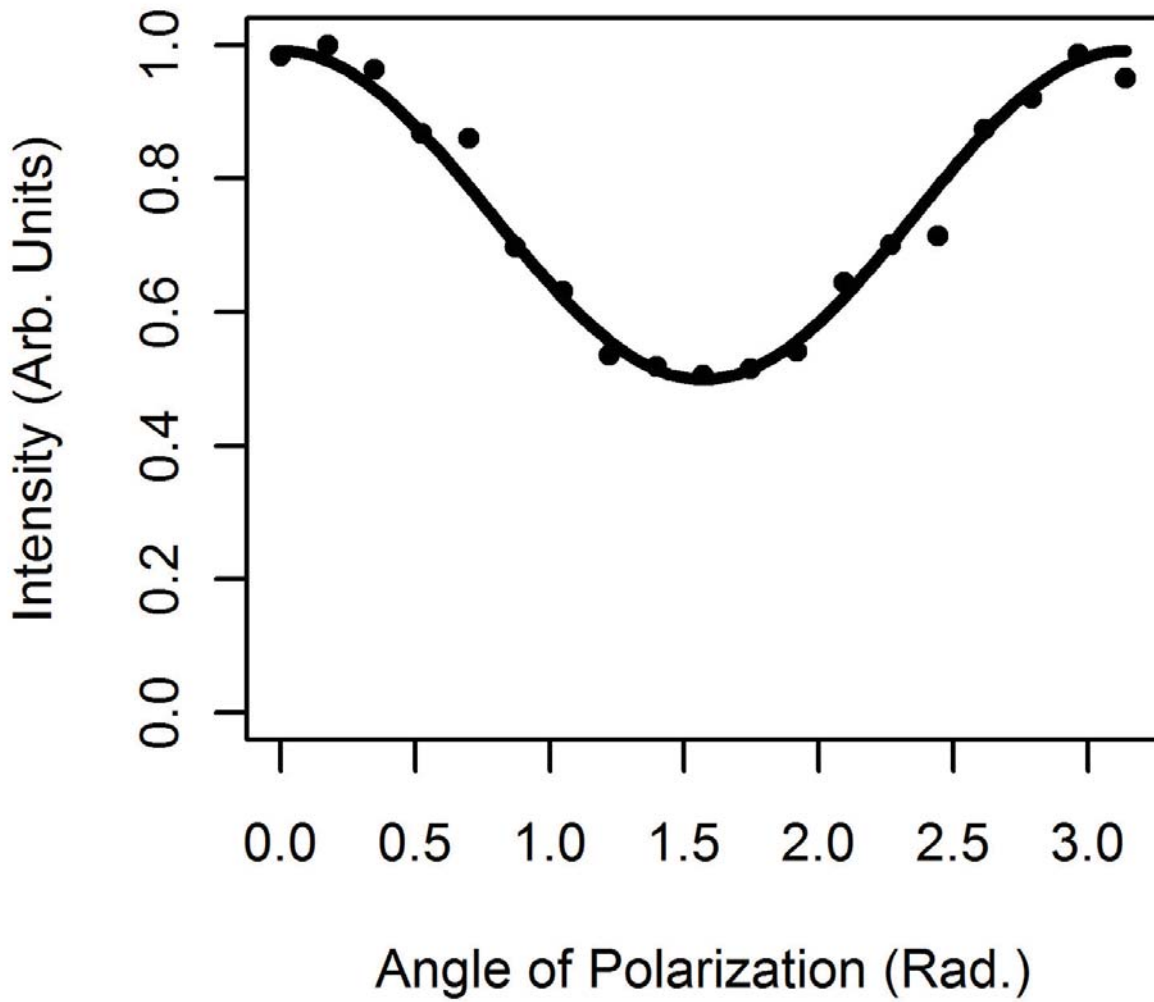
Figure 4.10: PAD of TDAE using 609 nm light.

0.17 eV. The former of these two cases is more likely due to the doubly excited nature of the zwitterionic state (thus, there is a two-photon requirement to reach the state).

570 nm light was used to ionize tetrakis(dimethylamino)ethylene because a three photon excitation would match the 190 nm absorption maximum. This wavelength provided a substantial increase in the photoelectron signal as well as the appearance of an additional peak in comparison to the other wavelengths used to study the molecule. The apparent peak positions are located at 0.2 eV and 0.7 eV. In addition, the low energy (0.2 eV) peak is skewed towards zero kinetic energy which would suggest an overlap with the thermal peak. In all other cases the thermal peak is the larger (even if only slightly) of the two available channels. Thus, ionization with 570 nm provides a unique situation in which one of the other channels of ionization are overwhelmingly stronger.

Due to the significant increase in photoelectron signal, a 1 mm aperture had to be used to reduce the incident photon flux. The laser power was reduced by incrasing the q-switch delay time as well. Only with both of these adjustments was the signal lowered enough to prevent a saturation of the DAQ board. In reducing the power, two additional peaks vanished from the spectrum located at 1.13 eV and 1.70 eV. It is assumed that these peaks may be due to a coupling electronic and vibrationally excited states of the molecule given the equal energy spacing.

The location of the Z state and the CT state are 3.2 and 2.7 eV above the ground state, respectively. Therefore initial excitation using 570 nm would require two photons to reach an excited state which could then decay to one of these states. In this case the excited state quickly degrades to the zwitterionic state which can then intercept a third photon and ionize. This is the perceived path resulting in the first of the photoelectron peaks, 0.175 eV.

The second of the two peaks is likely due to the three photon vertical ionization of the TDAE molecule. Given an electron energy of 0.7 eV, this would place the vertical IP at 5.89 ± 0.1 eV in good agreement with theory and previously measured vertical IPs of TDAE (Centinkaya et al., 1971; Nakato et al., 1972).
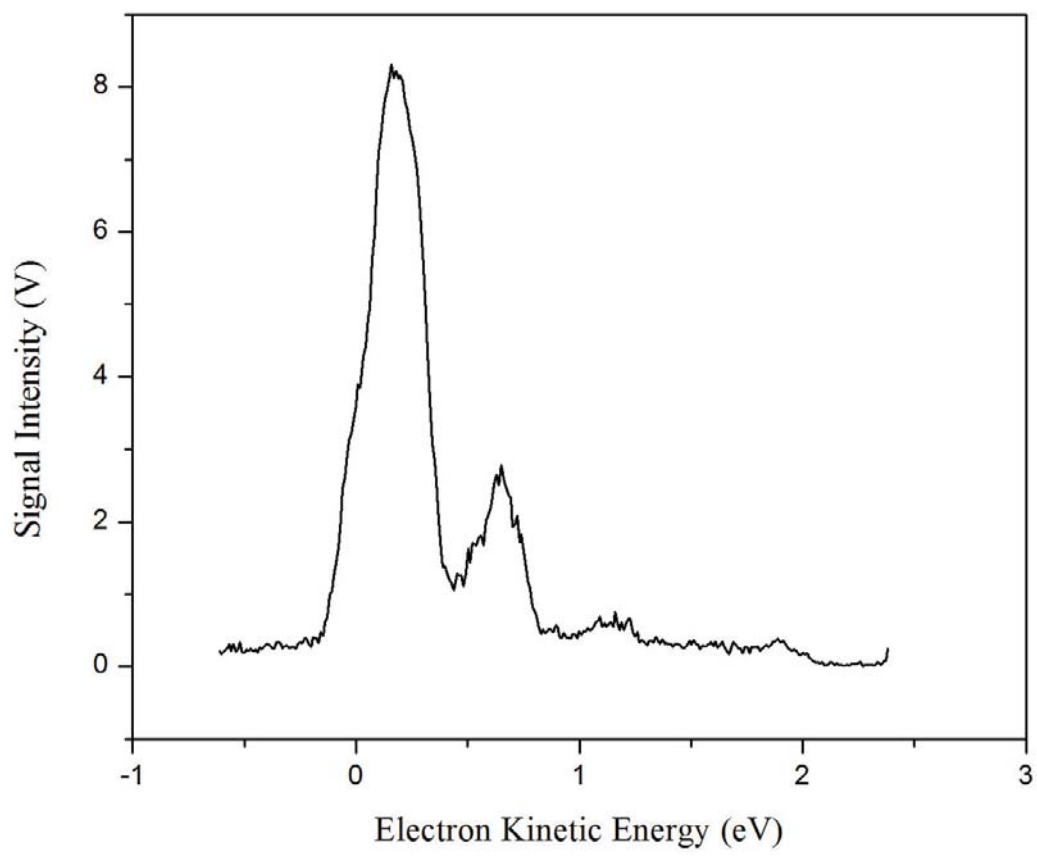
Figure 4.11: Photoelectron spectrum of TDAE using 570 nm light.
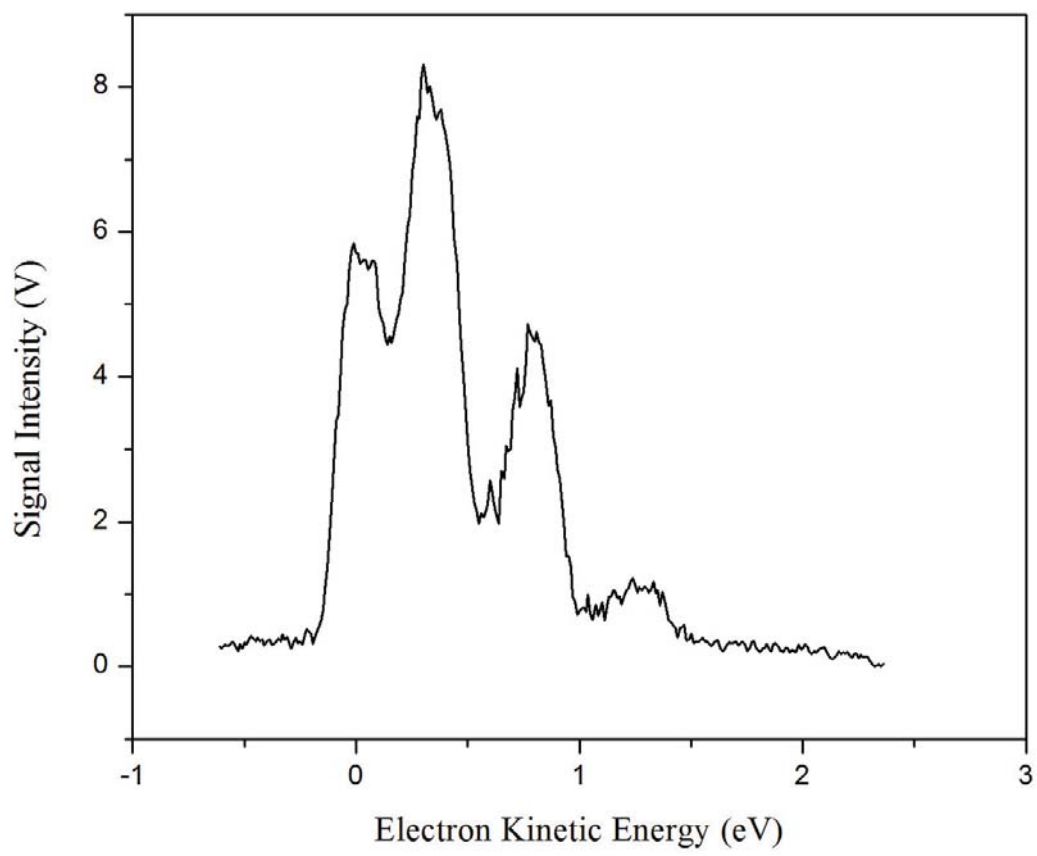
Figure 4.12: Photoelectron spectrum of TDAE using 532 nm light.

4.4 Conclusion

From this data it is apparent that the CT state lies approximately 2.5 eV below the ionization potential, just below the doubly excited Z state which is approximately 2 eV below the ionization potential. Thus, the Z state is 3.2 eV above the ground state while the CT state is 2.7 eV above the ground state. The fluorescence spectrum is peaked at 480 nm (2.58 eV) which corresponds directly to the CT state as expected.

It is important to note that all of the wavelengths used in this study except 570 nm produced peaks at $\sim$0 eV which must be attributed to an auto-ionizing state. Although the presence of this peak is expected due to the skew of the low energy peak, its presence is severely muted. In sharp contrast to these results, it has been shown that the auto-ionizing peak can be attenuated through the use of femtosecond lasers (Gloaguen et al., 2005). The authors use a pump-probe technique to produce photoelectron spectra. By using a single 266 nm (4.10 eV) pump photon and two 800 nm (1.55 eV) probe photons, the auto-ionizing peak is the largest of all of the peaks recorded. Furthermore, modulation of the time between pump and probe show that this low energy peak vanishes after about 300 fs. If, on the other hand, a pump of a single 266 nm photon is used in turn with a probe of a single 400 nm photon, the auto-ionizing peak drops dramatically in intensity.

One cause is particularly intuitive: The loss of an electron during a predissociation process, i.e.

$$\text{M} + \text{h}\nu \rightarrow \text{M}^* \rightarrow \text{N} + (\text{M} - \text{N}) + e^- \tag{4.15}$$
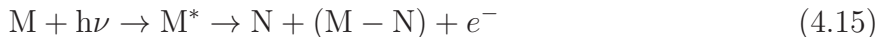
in which case either the N or (M-N) fragment is positively charged. TDAE is known to fragment under photoillumination (Mirsaleh-Kohan et al., 2011). Yatsuhashi *et al.* have shown that photo-fragmentation of TDAE can be prevented in the case of femtosecond laser illumination with 800 nm light (Yatsuhashi et al., 2006). This is due in part to two mechanisms: The choice of wavelength should be off resonant with a particular fragmentation and the laser pulses are suitably short so as to not introduce the molecule of interest to long-lived electromagnetic fields. Therefore, it may be possible that the energy input of a 266 nm

photon and a 400 nm photon simultaneously then mutes the dissociation process which in turn reduces the intensity of the low energy photoelectron signal.

Here, a less intuitive cause is presented: Photoexcitation of the four lone pair electrons of Nitrogen results in a quadruply degenerate electronic state. By using Rydberg Fingerprint Spectroscopy, photoelectron signal from TDAE indicates that ionization occurs from these lone pairs (Gosselin and Weber, 2005). This may be characterized in turn through the use of a superposition of two resonance structures. As described above, the degeneracy of these states is broken rapidly ($\sim$ 300 fs) and quickly decays to the Z state. Prior to this decay, the absorption of photons results in a collective excitation of the Nitrogen lone pair electrons and the $\pi\pi^*$ system of the ethylene bond. The result of this absorption channel is a near-continuity of states which auto-ionize as well as the strong resonance structure peaked at 190 nm (Figure 4.3).

Theoretical predictions of collective excitations were made throughout the twentieth century, but were met with considerable skepticism until the 1960's. Although such excitations were widely considered a theoretical tool, Nicolaides and Beck provided an empirical test of their existence: "transitions at a particular energy (which) seem to have an unusually large probability" (Nicolaides and Beck, 1976). While the authors use this markedly reserved language, the mathematics provide a simple explanation to the unusually large transition probability. A similar phenomenon has been widely observed in Nuclear Physics in which 'giant resonances' may be measured due to a collective oscillation of the protons in a nucleus against the neutrons in the presence of a strong electromagnetic field.

A simple example of collective excitations due to correlated electron systems has been demonstrated in super-cooled Rubidium systems (Gaetan et al., 2009). In this case two Rubidium atoms are pumped to Rydberg states before being placed at specific proximities using optical tweezers. The atoms are then subjected to a specific wavelength which results in independent ionization. At internuclear distances of 10 μm the system shows no correlation while an internuclear separation of 4 μm provides an apparent signal difference. The change in signal may be explained directly by Pauli's Exclusion Principle: If the atoms are spaced closely enough to 'communicate,' the fermionic nature of the electrons prevents

the occupation of the same state. The result then is a splitting of the states which prevents ionization at a particular photon energy. This has been called the *Rydberg Blockade of Excitation.* It is easily seen that electrons bound to a molecule will be much closer in proximity than this example.

Tetrakis(dimethylamino)ethylene provides a good example of a molecule which could show a collective excitation. The correlated eletron system of the Nitrogen long pairs allows for a strong electronic wavefunction overlap. This then provides a matching condition on which an excitation would provide an unusually large transition probability. Furthermore the photoexcitation of this correlated electron system results in a giant resonance which lies above the ionization potential. Given this energy input, the energy of any exciting photon may be spread to more than one electronic state. Also, the signal enhancement at these photon wavelengths is largely contained within the electronic excitation, i.e. there is no indication of increased dissociation.

In addition to collective excitations within TDAE, a similar phenomenon may be responsible for the lack of photoelectron signal in other highly symmetric molecules such as hexafluorides. The most apparent of these is Uranium Hexafluoride (UF_6) which shows no direct electron loss for input energies far exceeding the theoretical ionization limit of the molecule (Armstrong et al., 1994). In this case photodissociation of the molecule results in the fragments UF_i^+ for $i = 0$ to 5, but not UF_6^+.

Chapter 5

Methanolisis and the Second Electron Affinity of TCNQ

7,7,8,8-Tetracyanoquinodimethane (TCNQ) has played a major role in the study of isolated, multiply charged anions. This molecule was first popularized as an organic metal when combined with tetrathiafulvalene (TTF) to form a charge-transfer salt (Ferraris et al., 1973). Given this classification, significant interest arose in utilizing TCNQ and its compounds in the field of high-temperature superconductivity (Coleman et al., 1973). Although solutions and charge transfer salts containing TCNQ proved to be insufficient in this field, the molecule had gained its place as a good electron acceptor. This characteristic is attributed to the exceptionally large electron affinity (3.3 ± 0.3 eV) (Jin et al., 1994).

The first empirical electron affinity measurements of TCNQ were published through the Transactions of the Faraday Society as 2.83 eV (Farragher and Page, 2967). The listed value arises from a measurement of a current on a target plate resulting from negative ions passing through a conductive grid in the presence of a magnetic field. The logarithm of the ratio of the incident current of the negative ion beam to the resultant current on the plate is described by a linear relationship. The slope of this line then corresponds to the electron affinity of the molecule. Calculated electron affinities using the magnetron method have been shown to be underestimates due to the lack of accounting for excited states (Collins et al.,

1969). Despite this, Compton *et al.* reported a similar value of 2.8 ± 0.1 eV nine years later (Compton and Cooper, 1976).

The EA was further updated 20 years later to be 3.3 ± 0.3 eV using a "bracketing" technique (Jin et al., 1994). This method utilizes a competitive electron attachment to TCNQ in the presence of other compounds with known electron affinities. In this case TCNQ was bracketed between iodine (EA = 3.06 eV) and chlorine (EA = 3.66 eV). The AEA has been calculated to be between 2.14 and 4.37 eV using a plethora of levels of theory (Nielsen and Nielsen, 2003; Milían et al., 2004; Zakrewski et al., 1996).

Shortly after the first empirical measurements of the AEA, formation of TCNQ dianion states began to pique interest. In 1972 a polargraphic method method was used to infuse a surplus of electrons into a TCNQ solution after which the dianion was observed (Jonkman and Kommandeur, 1972). A year later, Ferraris *et al.* explained a drop in the Madelung energies of a TTF-TCNQ charge-transfer salt with the presence of a dianion. This explanation also accounts for an observed transition from insulator to metal (Ferraris et al., 1973).

Preliminary calculations of the second electron affinity began with an energy measurement in the "disproportionation reaction," i.e. the energy difference in the reaction

$$2\text{TCNQ}^- \rightarrow \text{TCNQ} + \text{TCNQ}^{2-}. \tag{5.1}$$
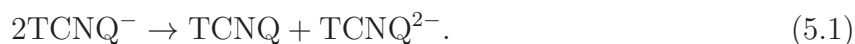
In this case the energy deficit (ED) is measured during the charge rearrangement. The second EA is then given by:

$$\text{EA}_{\text{TCNQ}^-} = \text{EA}_{\text{TCNQ}} - \text{ED}. \tag{5.2}$$

Several techniques exist to measure this energy deficit, but typically data is ascertained through cyclic voltammetry which relies on a hysteresis loop formed during a cycling of voltage differences. Values from these measurements span the range of 3.5 eV to 5.54 eV (Jonkman and Kommandeur, 1972; Jonkman et al., 1974; Johnasen, 1975). The relatively

large range reported here is likely a result of solution effects. The dianion was not studied *in vacuo* until three decades later following several experimental advances in gas phase analysis.

Nielsen and Nielsen hypothesized that the radical anion of TCNQ that is produced in ESI could be collided with an alkali beam at high energies in order to produce the dianion (Nielsen and Nielsen, 2003). This experiment was carried out by accelerating TCNQ anions to energies on the order of 50 keV. A bending magnetic was then used in order to mass select the anions prior to passing the beam through a differentially pumped chamber of neon gas or sodium vapor. Mass analyses were then carried out using a 15 cm, 180° energy analyzer. Naturally, collisions with neon resulted in a much smaller dianion signal than did collisions with sodium. This is a direct result of the availability of sodium's single $3s$ electron by the TCNQ monoanion. Due to the even mass, symmetric cleavage of the TCNQ monoanion would result in a mass peak of 102 amu; thus, the dianion signal is indistinguishable from the symmetric cleavage of the monoanion. In order to provide conclusive evidence of the existence of the dianion, isotopic TCNQ including one ^{13}C was mass selected for the charge transfer process. This resulted in a mass peak of 102.5 amu proving the existence of a stable TCNQ dianion in the gas phase.

Due to the fact that TCNQ has been shown to form long-lived dianion states *in vacuo*, experiments involving the measurement of the cross-section and the lifetime of the metastable are possible. Panja *et al.* have carried out a thorough investigation of the lifetime of dianion states using the Electrostatic Storage Ring in Aarhus (ELISA) (Panja et al., 2007). TCNQ dianions were again created by passing monoanions through a target vapor before entering an electrostatic storage ring. In contrast to direct mass analysis using a hemispherical energy analyzer, dianion products were studied by analyzing molecules within a fractional leakage from the ring. Lifetimes were then modeled using the decay rate of the relative dianion population resulting from collisional detachment caused by ambient air molecules (at about 10^{-11} torr). In the same experiment, excited state energy measurements were taken only for perfluorinated TCNQ (TCNQF$_4$) by photodetachment using an (Nd:YAG) laser.

The authors found that the rate of decay for TCNQ^{2-} and TCNQF$_4^{2-}$ were sufficiently described by three exponential terms indicating "...that in the electron transfer process, two

different electronically excited states are populated to account for the two short lifetimes" (Panja et al., 2007). Juxtaposing the unfluorinated and the perfluorinated dianions of TCNQ shows that the molecules have remarkably different decay lifetimes as well as state populations. The majority of the TCNQ dianions populate the state with the shortest decay lifetime, interpreted as an excited state. This is likely due to vibrational excitation during the collisional charge transfer process. The imparted vibrational energy may result in more dissociation in $TCNQ^{2-}$ than it does in $TCNQF_4^{2-}$.

Given this strong evidence for the existence and stability of $TCNQF_4^{2-}$ dianions, further measurements of the collisional charge exchange cross-section were performed (Ovchinnikov et al., 2006). Xenon and sodium were used as the collision target resulting in very different function forms of the cross section. Collisions with xenon generated an unstable cross section due to Rosenthal-Bobashev oscillations produced by the fine structure mixing of the adiabatic curves of xenon ($Xe_{1/2}$ and $Xe_{3/2}$). Thus, the threshold of charge transfer is delayed in xenon collisions due to preferential excitation over ionization. In sharp contrast, collisions with Sodium show an ever increasing cross section as the impact energy is decreased. By conservation of energy, the cross section must vanish at an energy equal to difference of the ionization potential of sodium and the second electron affinity of $TCNQF_4$. Because no low energy measurements were made, this threshold was not observed.

In order to produce negative ions of 7,7,8,8-tetracyanoquinodimethane (TCNQ), the laser desorption ionization (LDI) technique was used. This technique utilizes incident laser light to eject molecules resting on a surface. In addition, the stability of the anion was assessed by electro-spray ionization (ESI) mass spectrometry.

5.1   Methanolisis of TCNQ

It was proposed in 1999 that TCNQ undergoes a charge-transfer reaction reulting in the addition of a methoxide group to one of the dimethylamino branches of TCNQ (Figure 5.1) (Tanemura et al., 1999). This follows from the simultaneous addition of hydrogen to one dimethylamino branch and the addition of the methoxide group to the opposite branch. This

in turn breaks the double bonded carbon atoms in the *para*-positions reulting in a benzene ring. Upon the loss of a hydrogen atom, the (TCNQ + methoxide) molecule is then a free radical. This reaction is completely reversible.

This reaction pathway is similar to a Michael reaction in which a stable anion "undergoes conjugate addition with to α, β-unsaturated carbonyl compounds" (Carey, 2003). In this case the ethylene bond is broken in order to form a tetrahedral end with two cyano-groups and a methoxide group. These reactions are generally base catalyzed.

This reaction was proposed as a result of a shift over time of the absorption spectrum (Rabie, 2012) in addition to NMR and elemental analysis (Tanemura et al., 1999). There are two bands associated with this spectrum at 373 nm and 394 nm in ethylene and methylene chloride. The difference between these two solvents was solely intensity of signal. A solution of pure methanol produced a similar spectrum, but the peak at 373 nm began to vanish while a peak at 336 nm began to appear. As demonstrated in the absorption spectrum, the reaction reaches approximate equilibrium after 33 minutes using a solution of 4.0×10^{-6} mol per dm^3.

Methanol was first used to spot a metal plate for use in laser desorption ionization. Over the course of a week, the solution turned from a translucent yellow hue in to a dark green solution. Over the next month, the solution continued to darken and transition to blue. Thus, the reaction rate is slow and further investigation requires accelerating the reaction. In order to do so, two methanol/TCNQ solutions were prepared, each at a concentration of 0.5 mg/ml.

In order to test the theory that the replacement is a Michael reaction, a 0.5 M solution of potassium hydroxide was used to base catalyze the reaction. The final color of the solution was red. The second solution that was prepared was refluxed for 8 days in a hot sand bath at the boiling point of methanol. The solution changed color from a pale yellow to a dark green.
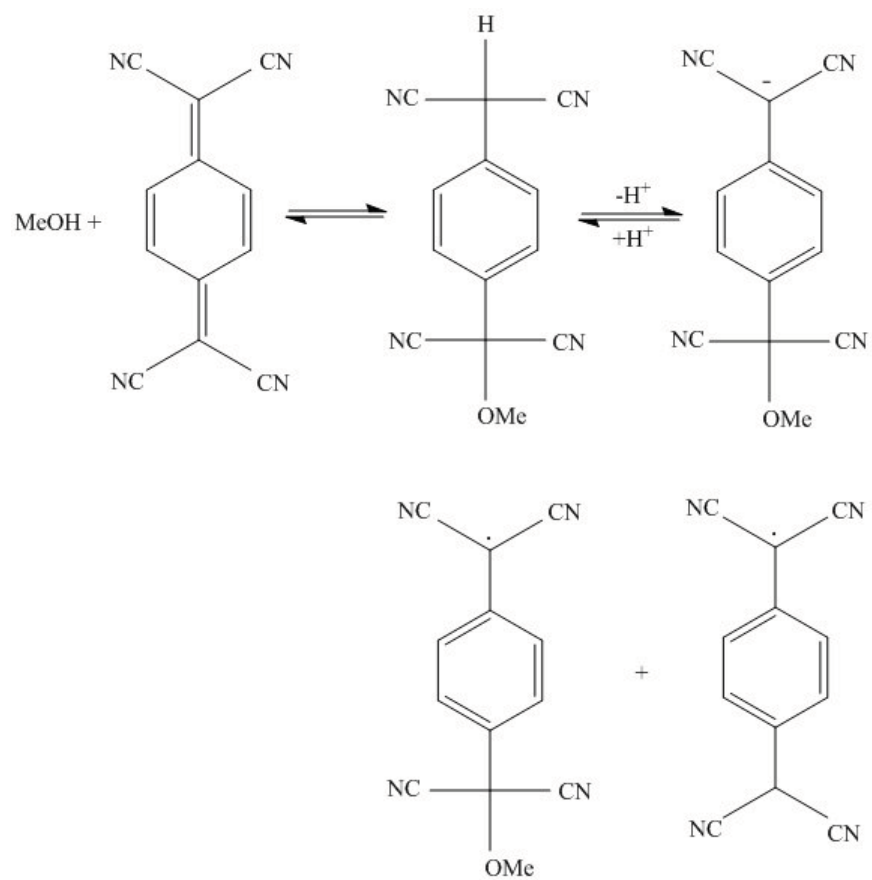
Figure 5.1: Reaction steps towards the addition of a methoxy group to TCNQ.

After the first solution reflux was finished, the solution was neutralized using 12 M hydrochloric acid. This caused potassium chloride to percipitate out as

$$KOH + HCl \rightarrow H_2O + KCl.$$
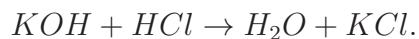
Unfortunately, use of a rotary evaporator resulted in no product. We propose that the base catalysis resulted in a different product which perciptated out with the potassium chloride. This prevented acquisition of the target product for further analysis.

The second reflux produced a green solution which needed to be further purified prior to analysis. TCNQ is a yellow-orange crystal and the addition a methanol produces a blue product. In order to isolate this product, the solution was run through a meter long silica gel column over the course of three days. The active phase used in the separation was chosen to be chloroform due to TCNQ's solubility. The first band that was extracted was a yellow band corresponding to pure TCNQ.

The blue product preferentially attached to the acid washed sand at the top of the column. Therefore, the product was run through the column using a mixture of methanol and chloroform. In order to prevent the formation of bubbles in the silica gel which would hinder solution movement, the concentration of methanol was increased in steps of 0.5% by volume. It should be noted that the product only moved through the column with the addition of methanol, but this movement left streaks of yellow and green indicating the reversibility and the potential existence impurities in the sample.

5.1.1 Instrumental Analysis of Product

In order to mass analyze the sample, ESI-TOF-MS were implemented. First, the sample produced from the yellow band was analyzed using ESI-TOFMS to assure that the sample was pure TCNQ (204 AMU, Figure 5.2). It is important to note that any methanol that the TCNQ comes in contact with will react with the molecule. This is especially important when cleaning the instrument prior to analysis of the blue sample. If pure methanol is used

to clean the sample line to the instrument, that solvent will react with the residual TCNQ in the line and give a false positive for the presence of methoxide-TCNQ (235 AMU).

After the initial introduction of methanol, the simple methoxide addition can be seen in the mass spectrum (Figure 5.3). It is believed that this indicates the presence of a free radical anion which must be highly reactive. The presence of a dominant 242 AMU peak would seem to indicate that (TCNQ + MeO) is not the final stage of the reaction, but simply an intermediate. Mass analysis of the methanol solution produces a dominant peak at 242 AMU with residual TCNQ as an impurity. The collision-induced dissociation of the 242 AMU product resulted in peaks at 215, 190, and 166 AMU in addition to any parent which was not fully dissociated.

The exact identity of the 242 AMU molecule remains a mystery, although the CID may give some hints. The lack of a parent 204 AMU peak in the collision-induced dissociation demonstrates that the final product is likely not a simple functional group addition. The 215 AMU fragment indicates a loss of 27 AMU which is most likely HCN. Given these two pieces of information, it would seem that the final product would involve the attachment of more than one methoxide group while also losing one or more of the cyano groups.

5.2 Theory of Collisional Charge Transfer

The theory of collisional charge transfer begins with a series of approximations concerning the quantum states and kinetics of the charge transfer partners; this paradigm is called Landau-Zener Theory. The charge transfer process involving molecules A and B are modeled as a transition between two states: The first state is given by the agglomeration of the wave functions of A^- and B while the second state is composed of the wavefunctions A^{2-} and B^+. No entanglement is assumed and therefore the total wavefunctions are simple sums of the two independent wavefunctions. The Hamiltonian describing the motion of each of these states includes an interaction potential which depends solely on the internuclear distance between the two species, R_C.
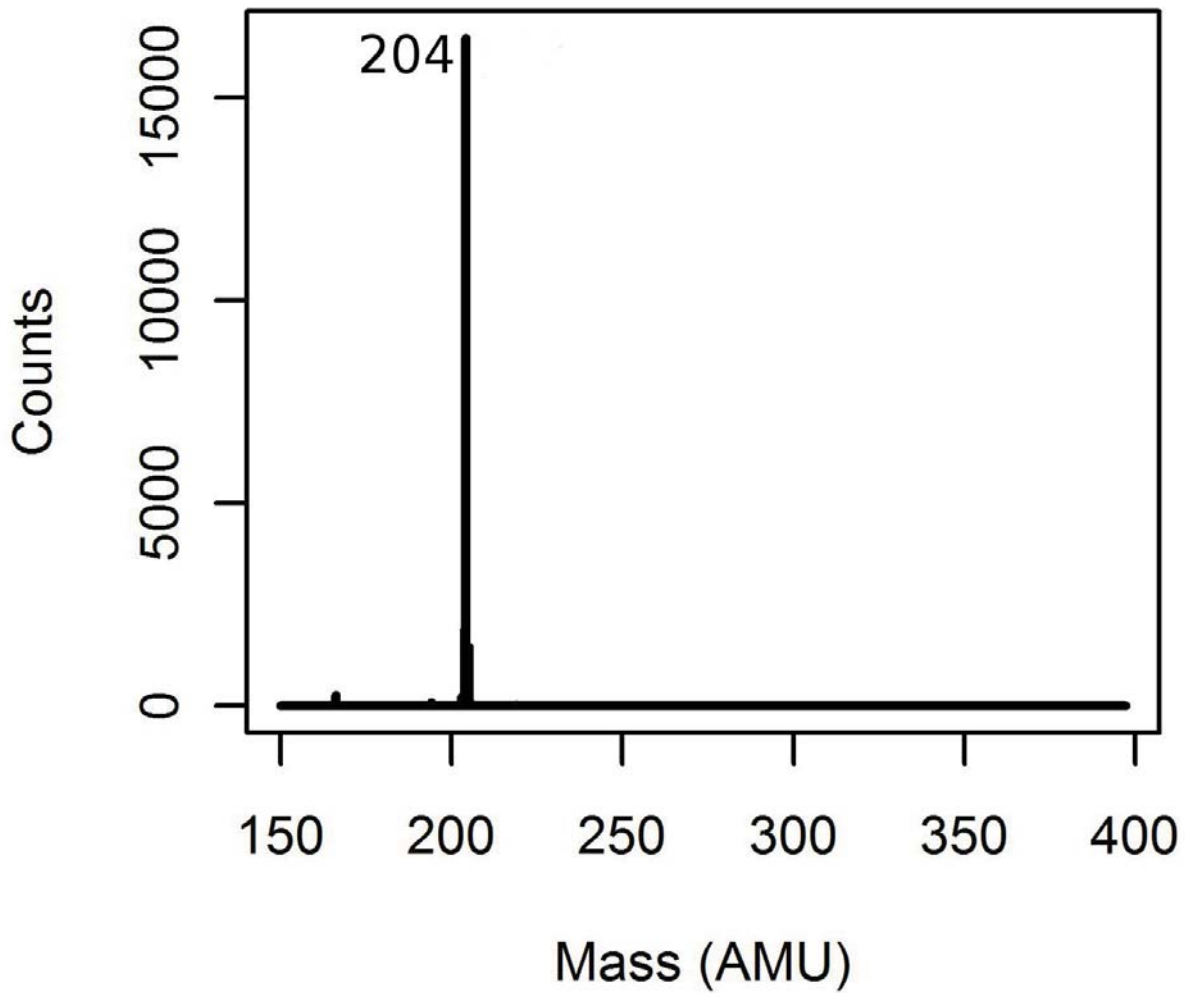
Figure 5.2: Mass spectrum of TCNQ in acetonitrile, purified through column chromatography.
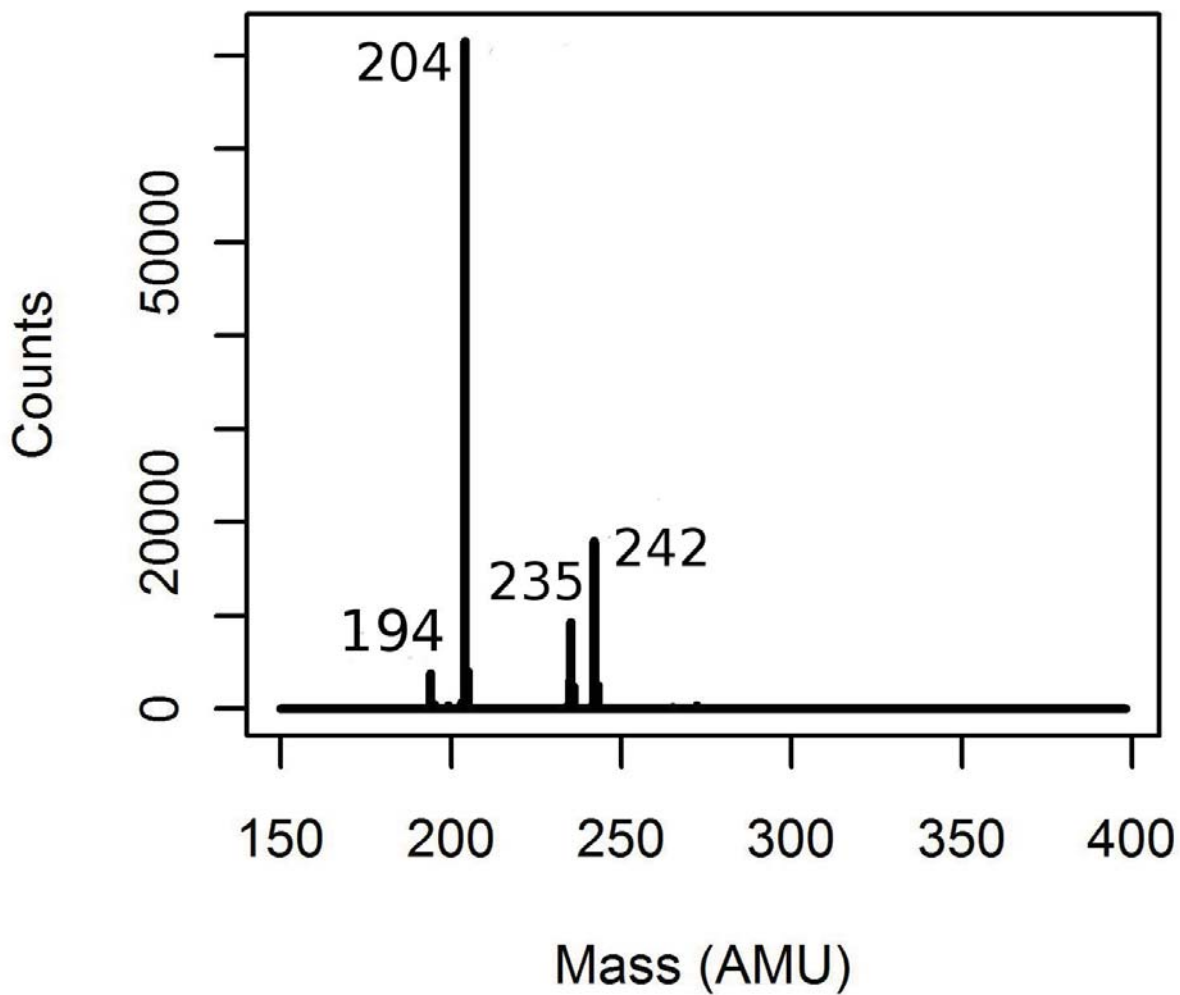
Figure 5.3: Mass spectrum of TCNQ in methanol after ~30 minutes.
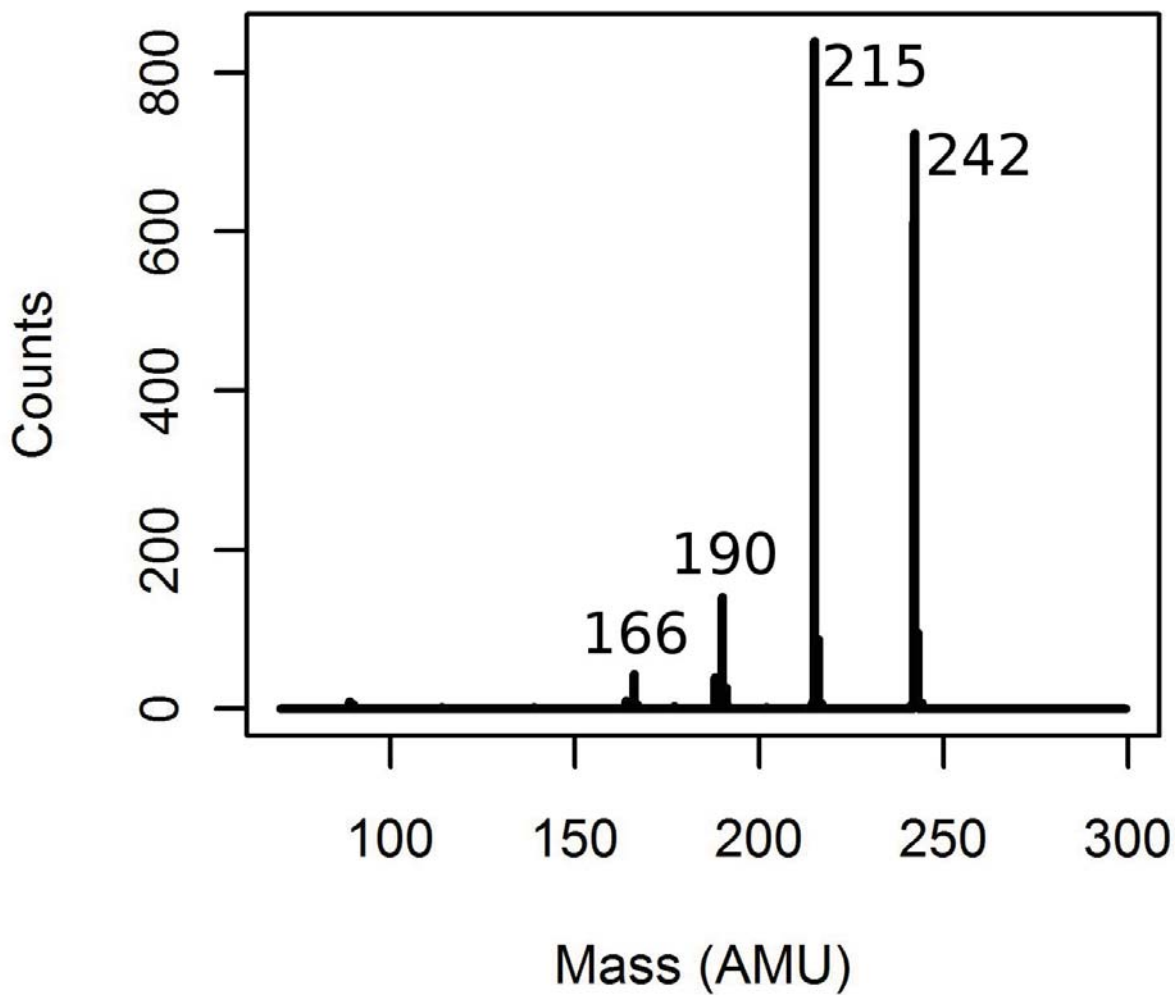
Figure 5.4: Collision induced dissociation of TCNQ+MeO 242 mass peak.

The first of these states is described by an essentially flat potential curve due to the lack of a Coulomb force. A more detailed estimation of the interaction potential involves a dipole interaction ($V \propto r^{-3}$) arising from an induced molecular polarization of the collision target within the electric field of the A$^-$ monoanion. As the internuclear separation approaches zero, the interaction of the two species will be dominated by the strong repulsion of the nuclei. The second of these states will have a strong repulsion at very small internuclear distance as before, but the majority of the interaction curve is described by the Coulomb attraction between the positive target and negative projectile.

Given these two states as the starting point, two important approximations must be implemented in order to drastically simplify the following formalism. These two approximations are labeled the Born-Oppenheimer Approximation and the Adiabatic Approximation. Under the former approximation, the motion of the electrons is assumed to be independent of the motion of the nueclons (protons and neutrons). This arises from the large mass difference between the electrons and the nucleons which means that the respective motion will occur on different time scales. Thus, the electrons will move in the electric field of the nuclei and the nuclei will move in the electric field of the electrons. This gives rise to separability of the electronic and nuclear motion in one Schrödinger equation. The Adiabatic Approximation on the other hand simplifies the nuclear motion by assuming that there is no nuclear coupling, i.e. the nuclei are at an optimal geometry and therefore their geometry do not affect each other. This approximation is tangible to the problem at hand because the concern lies with the electronic motion which is much faster than the motion of the nuclei. Thus, the electromagnetic field generated by the electrons is an average force field over the electron trajectory when considering the nuclei.

The wave functions of the first state are given by

$$\Psi(\vec{r}) = \phi(\vec{r})\psi(\vec{r}) \tag{5.3}$$

where there ϕ describe the nuclear motion in the electric field of each electron and the ψ are the electronic wave functions. The electronic wave functions are also known as *adiabatic*

functions with corresponding *adiabatic potentials* as eigenvalues. This term refers to the fact that the eigenvalues correspond to potentials of the nuclear motion.

In a charge exchange process we consider only the electronic wave functions as the molecular symmetry does not change between the neutral and monoanion (or the monoanion and the dianion). As will be shown, the symmetry of the electronic orbitals dictates that no two electronic wavefunctions may overlap. The two adiabatic potential curves will then approach each other without crossing; the point of closest proximity is called the *avoided crossing*. Our interest therefore lies in the behavior of the wave function about the avoided crossing. At this point the eigenvalues are nearly degenerate and are solutions of the Schrödinger Equation given by

$$(\frac{\hbar^2}{2\mu}\nabla^2 + V)|\phi> = E|\phi> . \tag{5.4}$$

Spatially perturbing the Hamiltonian results in

$$H(R) \approx H(R_C) + W(R) \tag{5.5}$$

for $W(R) = (R - R_C)\frac{\partial}{\partial R}H|_{R=R_C}$. Any wavefunction in the electron's Hilbert Space may be expanded by a linear combination of the individual wavefunctions on either side of the avoided crossing:

$$\Phi = a\phi_1 + b\phi_2. \tag{5.6}$$

Plugging this into the Schrödinger Equation yields two equations:

$$
\begin{aligned}
<\phi_1|H(R_C) + W(R) - E|\Phi> &= a(U_1 + V_{11} - E) + b(V_{12}) = 0 \\
<\phi_2|H(R_C) + W(R) - E|\Phi> &= a(V_{21}) + b(U_2 + V_{22} - E) = 0
\end{aligned}
\tag{5.7}
$$

A non-trivial solution will only exist in the case of a vanishing determinant. Applying this constraint leads to two energies which must be degenerate; this in turn leads to the

implication that

$$(U_1 - U_2 + U_{11} - U_{22}) = V_{12} = 0. \tag{5.8}$$

The degeneracy condition hinges on the fact that both of these equations may be satisfied simultaneously. Because there is only one degree of freedom to vary, namely r, only one of these equations may be solved. If the two wavefunctions are of different symmetries, the cross-term will vanish at the crossing. On the other hand, if the symmetries are the same, crossing is no longer degenerate and it is therefore "avoided." This is generally the case for charge transfer.

In order to describe the transition, one must use the previous wave functions to solve the time-dependent Schrödinger Equation:

$$\frac{i}{\hbar}\frac{\partial}{\partial t}|\Phi> = (H(R_C) + W(R))|\Phi> \tag{5.9}$$

resulting in

$$i\frac{\partial a}{\partial t} = a(U_1 - V_{11}) + bV \tag{5.10}$$

$$i\frac{\partial b}{\partial t} = b(U_2 - V_{22}) + aV \tag{5.11}$$

for $V = V_{12} = V_{21}^*$. Applying the spatial perturbation to the eigenvalues gives

$$U_1 - V_{11} \approx U_C + F_1(R_C - R) \tag{5.12}$$

$$U_2 - V_{22} \approx U_C + F_2(R_C - R) \tag{5.13}$$

where $F_i(R_C - R)$ is the gradient of the adiabatic curve evaluated at the avoided crossing, namely $F_i(R_C - R) = \frac{\partial(U_i - V_{ii})}{\partial R}$. The constant term associated with U_C is dealt with by including a complex exponential phase:

$$a'(t) = a(t)\exp(-iU_C t) \tag{5.14}$$

$$b'(t) = b(t)\exp(-iU_C t). \tag{5.15}$$

102

Finally we make use of the semi-classical approximation that the nuclei will folllow a classical trajectory thus implying that the velocity can be written as the time derivative of the internuclear separation ($\frac{\partial}{\partial t} = v\frac{\partial}{\partial \xi}$). This results in the following system of partial differential equations:

$$iv\frac{\partial a'(t)}{\partial \xi} = F_1(R_C - R)a' + b'V \tag{5.16}$$

$$iv\frac{\partial b'(t)}{\partial \xi} = a'V + F_2(R_C - R)b'. \tag{5.17}$$

Solving these equations and taking the magnitude gives the result

$$|b'|^2 = \exp(\frac{-2\pi V^2}{v|F_1 - F_2|}) = 1 - |a'|^2. \tag{5.18}$$

The term $|b'|^2$ is associated with the probability that the collision will result in a nonadiabaitc trasition. In order for charge transfer to occur, the system must go through one nonadiabatic transition and on adiabatic transition. Because the system does not discriminate between the order of these transitions, the total probability of transition is given by

$$P = 2|b'|^2|a'|^2 \tag{5.19}$$

thus giving the cross-section in its familiar form as

$$\sigma = \pi R_C^2 P = 2\pi R_C^2 \exp(-Q/v)(1 - \exp(-Q/v)) \tag{5.20}$$

where

$$Q = \frac{2\pi V^2}{|F_1 - F_2|} = \pi(\frac{\delta}{\Delta E})^2 \tag{5.21}$$

for the adiabatic splitting δ and energy deficit $\Delta E = IP_{target} - EA_{projectile}$.

5.3 Analysis of the Charge-Transfer Cross-Section

The collisional charge transfer cross-section can be modeled through the Beer-Lambert Law as

$$I = I_0 e^{-nl\sigma} \tag{5.22}$$

for initial intensity I_0, transmitted intensity I, number density n, path length l, and cross-section σ. The number of dianions formed via collisional chrage transfer is then given by

$$I_0 - I = I_0(1 - e^{-nl\sigma}) \approx I_0 nl\sigma \tag{5.23}$$

where a first order Taylor expansion has been used under the assumption that the charge transfer process occurs in a small percentage of cases.

Cross-sections for higher energy collisions have been acquired for TCNQ and perfluorinated TCNQ ($TCNQF_4$) using xenon and sodium. Collisions of TCNQ and $TCNQF_4$ with xenon were shown to preferentially excite electronic states in either molecule resulting in a delayed threshold for ionization. As stated above, it has been shown that collisions with xenon result in a deviation from the ideal Landau-Zener cross-section due to the $Xe_{1/2}$ and $Xe_{3/2}$ fine structure states. Due to the close proximity in energy of these two states, the cross-section will reflect contributions from both states.

The cross-section model that was fit is given by the Landau-Zener formula with an additive errors,

$$\sigma_j = 2\pi R_c^2 e^{-Q/v_j}(1 - e^{-Q/v_j}) + \epsilon_j \tag{5.24}$$

where the ϵ_j are assumed to be identically, independentally Normally distributed with mean 0 and precision τ, $Q = \pi(\delta/\Delta E)^2$, v is the impact velocity, and R_c and δ are the interatomic and potential curve separations at the avoided crossing, respectively. Note that this sees a maximum at $v_m = Q/\ln(2)$. The cross-section for charge transfer in the case of $TCNQF_4$ collisions with sodium result in an exponentially decreasing tail. There is a lack of data points in the low energy region to resolve a maximum. The expected threshold for charge transfer is given by the ionization potential of sodium (5.14 eV) minus the electron affinity

of TCNQF$_4$ ($\sim$ 0.6 eV) which is larger than the maximum energy extrapolated from this data, $E_m = \frac{1}{2}Mv_m^2 \approx 2.2$ eV. Thus, low energy data is needed to properly model the electron affinity of the perfluorinated TCNQ.

For the parent ion, the maximum energy data point can be resolved around a kinetic energy of about 8 keV in the lab frame (Figure 5.5). In atomic units this corresponds to a velocity of 3.972×10^{-4} a.u. or $\frac{\delta}{\Delta E} = 9.36 \times 10^{-3}$. For TCNQF$_4$ the potential surface separation is given through the WKB approximation as $\delta \approx 0.057$ eV (Ovchinnikov et al., 2006). Utilizing this separation for TCNQ results in a point estimate of $\Delta E = 6.088$ eV which is larger than the IP of sodium; thus, the electron affinity of TCNQ$^-$ is predicted to be negative. Because the dianion has been shown to be stable, either this separation does not apply to TCNQ or there is a resonance which provides stability in the dianion.

For a more in-depth analysis of the cross-section non-linear modeling was implemented. In this case fitting was carried out using four different methods: A maximum likelihood grid search, the Discrete Approximation, Marquardt-Levenburg non-linear regression, and Bayesian non-linear modeling using a Markov Chain Monte Carlo simulation. Results are summarized in Table 5.1.

Table 5.1: Different fits to collisional charge-transfer cross-section.

Method	R_C^2	Q	Sum Squares Error
Grid Search	0.0156	0.8780	0.0470
Discrete Approximation	0.0102	1.0605	0.1316
Marquardt-Levenburg	0.0157	0.8740	0.0470
Bayesian MCMC	0.0156	0.8755	0.0471

The maximum likelihood grid search was performed over a grid with boundaries given by $0.00001 \leq Q \leq 0.2$ and $0.2 \leq R_C^2 \leq 2.0$. The grid points were spaced by 0.002 for Q and 0.04 for R_C^2. Although the solution gave an excellent fit to the data, the grid's discrete
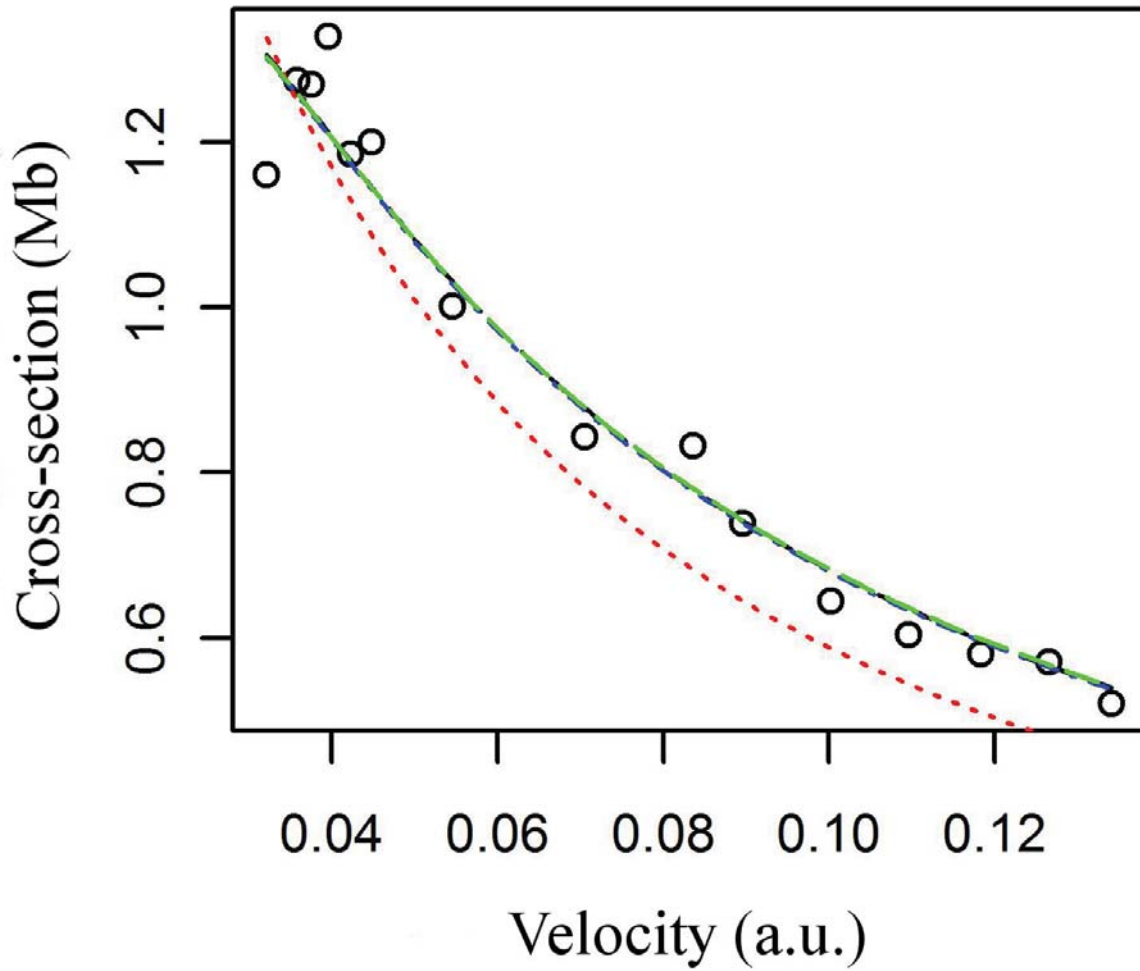
Figure 5.5: Modeling the collision-charge transfer cross-section. The grid-search minimum error curve is given in black, the Marquardt-Levenburg curve is given in blue, the Bayesian MCMC curve is given in green, and the red curve is the Discrete Approximation to the posterior distribution.

values do not allow for an absolute maximum; the solutions are only as precise as the grid. Therefore, continuing with the Frequentist methods, the Marquardt-Levenburg was utilized. This result is a maximum likelihood solution resulting from a constrained, iterative stepping procedure. Note that the parameter values obtained using this technique are very close to those values given by the grid search indicating that the grid was sufficiently fine.

To supplement these fits the Discrete Approximation was utilized as a Bayesian equivalent to a grid search. This method calculates the posterior probability distribution at each of the grid points. The final value is then the posterior-weighted average over the grid. The downside to this technique is that it is often more sensitive to the boundary size and step size than the Frequentist grid search. Therefore, this solution is supplemented with a Bayesian MCMC. In order to do so a Metropolis-Hastings sampling is used for the Q parameter while R_C^2 and precision are Gibbs sampled.

In the Landau-Zener theory Q and R_C^2 must be positive, thus the prior probability distributions used in the fitting procedure are

$$
\begin{aligned}
Q &\sim \Gamma(0.05, 1.00) \\
R_C^2 &\sim Exp(0.80)
\end{aligned}
\tag{5.25}
$$

where the parameter values for the priors are arbitrarily chosen from the grid search. The choice of an exponential distribution for the R_C^2 is partially motivated by the ability to then use Gibbs sampling. This can be seen in the resultant posterior distribution

$$
\begin{aligned}
Q|\sigma, v, R_C^2, \tau &\sim A\frac{\Gamma(1.05)}{\Gamma(0.05)\Gamma(1.00)} \times \prod_{i=1}^{N} \sqrt{\frac{\tau}{2\pi}} \exp[\frac{-\tau}{2}(\sigma_i - \hat{\sigma}_i)^2] \\
R_C^2|\sigma, v, Q, \tau &\sim truncN(-\frac{1}{0.8} + \tau\sum_{i=1}^{N}(\sigma_i\hat{\sigma}_i), \tau SSE)
\end{aligned}
\tag{5.26}
$$

where A is a normalization constant τ is the precision, and SSE is the sum squares error, $SSE = \sum_{i=1}^{N}(\sigma_i - \hat{\sigma}_i)^2$. Just as in the case of pNA, the prior probability distribution for the

precision is chosen to be a conjugate prior, namely a gamma distribution:

$$\tau \sim \Gamma(10, 2) \tag{5.27}$$

where the parameters are chosen arbitrarily. The posterior is then given by

$$\tau | \sigma, v, Q, R_C^2 \sim \Gamma(10 + \frac{N}{2}, 2 + \frac{SSE}{2}). \tag{5.28}$$

Using these posterior distributions we find that the fit is almost identical to that found by the Marquardt-Levenburg. On the surface then, the Bayesian technique was overkill. That is to say, the computational complexity rendered this method unecessarily difficult to implement. Nevertheless, more information can be garnered from the Bayesian fit than from a Frequentist fit because the posterior distrubions have been established. This means that in addition to the parameter estimates given by the mean, the median, variance, and 95% confidence intervals may be ascertained from this information.

Again, in this model we see that there is some inter-parameter correlation (Figure 5.6). For the purpose of comparison, a similar plot of the SSE versus the parameters is included for the simple linear regression model $y = mx + b$ (Figure 5.7). In this case data were simulated using

$$y = 23x + 5 + \epsilon$$

for normally distributed errors, $\epsilon \sim N(0, 25)$. Note that a similar ridge line can be observed in the case of linear regression. The inter-parameter correlations for linear regression have been studied in detail (Myers, 1986).

5.4   Conclusion

The analysis of 7,7,8,8-Tetracyanoquinodimethane was carried out to illuminate character-istics of MCAs, specifically to identify stabilizing characters involved in the attachment of multiple excess charges. Solution-based techniques to study the TCNQ molecule proved
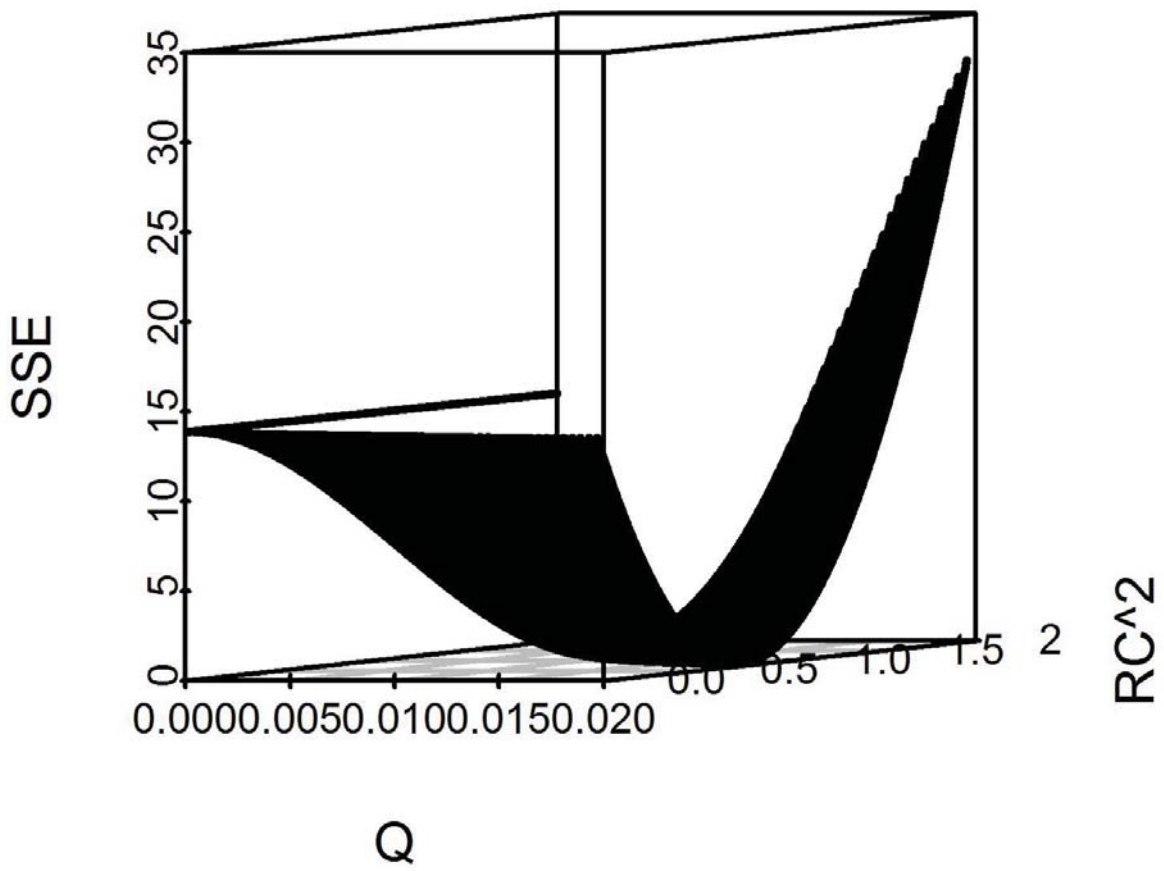
Figure 5.6: The model SSE versus each of the two parameters. Notice how a ridge forms indicating some inter-parameter correlation.
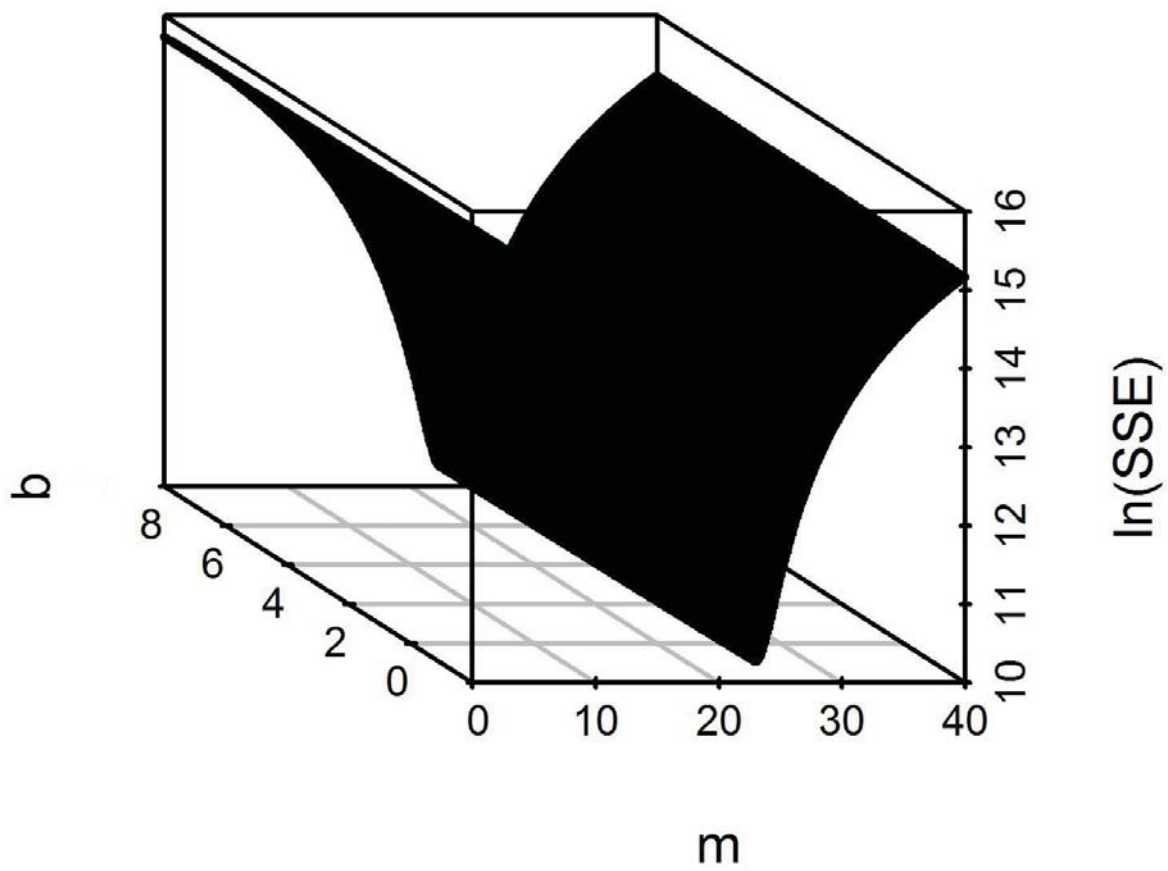
Figure 5.7: The logarithm of the model SSE versus each of the two parameters for linear regression. Notice how a ridge forms indicating some inter-parameter correlation.

to be complicated by it's reaction with many solvents. Although methanolisis of TCNQ was demonstrated here, similar reactions are expected in other solvents such as ethanol and tetrahydrofuran.

At high collisional energy, TCNQ has been shown to contain some information about the second electron affinity. While a point estimate of the energy seems consistent with calculation, Bayesian and Frequentist modeling of the collisional charge transfer cross section are expected to give an overestimate. For this reason, low-energy collisional data is highly anticipated; this would provide a more direct observation of the threshold for charge transfer as well as more evidence for a robust modeling. In the case of the modeling outlined above, although Bayesian methods give the same result as other techniques, the utility of this new technique is not futile. The posterior probability distribution obtained in this analysis can be used as a prior in a further analysis. Additionally, the parameter standard error may be reduced as a result of using estimators biased by the prior.

Chapter 6

Conclusion

While experimental investigations of molecular electronic states remains a technical challenge, this work outlines several techniques designed to acquire and subsequently process such information. Herein we present the experimental investigation of extraordinary electronic states of molecules through three specific examples: Photoionization and collision induced dissociation of pNA, photoionization of TDAE, and collisional charge transfer of TCNQ with sodium. In the case of pNA, photoelectron spectrscopy was used to investigate the possibility of dipole-bound negative ion states. We speculate that the lack of dipole-bound negative ion signal at low binding energy may be indicative of a "doorway state" in which the electron may bind first to the dipole moment and then fall into a valence-bound state. Similar observations were shown in other large dipole moment molecules such as nitroethane, nitromethane, and nitrobenzene (Stokes et al., 2008; Compton et al., 1996; Desfrançois et al., 1999). As more data are taken and other molecules investigated with dipole moments on the order of pNA (6.2 Debye), we hope to see a functional relationship between dipole moment and dipole-bound electron affinity.

Collisional data of pNA with argon were acquired with the intention to explore charge-transfer. Due to a preference for dissociation, collision induced dissociation experiments were carried out to examine intra-molecular bonding and transition states. Molecules of pNA fragment through the loss of NO via a transition state and NO_2^- as a result of direct

cleavage. We find that current modeling techniques are inadequate to accurately describe the cross-section curve due in a large part to the instability of numerical estimates to the partial derivatives. In order to address these issues, we implement a Bayesian algorithm to perform a non-linear regression which results in a smaller sum of squares error in comparison to the more traditional Marquardt-Levenburg stepping algorithm.

The photoelectron spectra of TDAE presented in this thesis gives strong evidence for the existence of collective excitations on a small, symmetric molecule. These excitations are conceptually similar to those seen in nuclear physics as well as collective oscillations in the plasma of metals (surface plamsons). Experimentally, the presence of a collective excitation in small molecules is indicated by the presence of multiple transition channels whose overlap results in an unually large probability of transition. TDAE was viewed as a potential source for collective excitations due to a strong absorption maximum about 1.0 eV above the adiabatic IP. An ES-101 hemispherical energy analyzer was modified for injection of target gas-phase molecules perpendicularly to a focused laser for the purpose of performing multiphoton ionization of TDAE.

Photon wavelengths of 441 nm and 355 nm were used to probe a charge-transfer states believed to be responsible for fluoresence in TDAE. 609 nm photons were then used to probe the doubly-excited zwitterionic state. These two states have been named the CT and Z state, respectively. Finally, photons of 570 nm (for which three photons are resonant with the absorption spectrum maximum) and 532 nm produce intense MP photoelectron signal which indicate ionization from a variety of different states. Additionally, approximately zero-energy electrons are ejected at all wavelengths. Due the presence of multiple ionization peaks in the 570 nm spectrum, an absorption maximum above the adiabatic IP, and the presence of an auto-ionizing state we propose that a collective excitation may bepartially responsible for MPI in TDAE.

In addition to investigating electron stability versus photodetachment, it is possible to elucidate stability in the presence of additional charges. To do so, we attempted to measure the second electron affinity of TCNQ. It has been shown that dianions of TCNQ are stable and possess excited states. In order to acquire the binding energy, we first used solution

113

based techniques to form the TCNQ dianion. Through this we find that charge-transfer salts preferentially form dication-(anion)$_2$ salts and interpretation of solution based methods are often convoluted by analyte molecules reacting with the solution, as in the case of methanolisis.

Modifications to the hemispherical electron energy analyzer were made to produce and analyze dianions. Although laser desorption ionization of TCNQ samples were shown to produce TCNQ anion signal with sufficient intensity, the signal remained below detectable levels within the energy analyzer. Nevertheless, high-energy collisional charge-transfer data were analyzed theoretically using Landau-Zener theory. A point estimate of -0.95 eV was provided from the maximum of charge-transfer. Further non-linear modeling was carried out with Bayesian and frequentist methods.

Given the acquisition of low-energy collisional data, an improved estimate of the second electron affinity may be attainable. Rather than purge the data taken at higher energy, we propose that the use of Bayesian methods would provide a robust analysis due to the use of previous information to form an informative prior on the model parameters.

Through these three experiments we hope to expand the field of Chemical Physics and enhance future analyses of extraordinary electronic states. In the case of dipole-bound anions, further comprehension of electronic binding may elucidate electron mobility characteristics in solids given the transfer of an electron from one molecule to the next through dipole-bound states. Collective excitations, which are familiar to other fields of physics, may be responsible for lack of direct photoionization and the formation of super-excited states in highly symmetric molecules. Measurement of second electron affinities may contain information about universal stability mechanisms in molecules. Finally, we find that Bayesian methods provide a novel statistical method for the analysis of Chemical Physics data although computational expense reserves these methods for more complex models.

114

Bibliography

Amicangelo, J. C. and Armentrout, P. B. (2001). Relative and absolute bond dissociation energies of sodium cation complexes determined using competititve collision-induced dissociation experiments. *Int. J. Mass Spectrom.*, 212:301. 6, 45, 48, 54

Anderson, D. F. (1981). A photoionization detector for the detection of xenon light. *IEEE Trans. Nucl. Sci.*, page 842. 67

Armentrout, P. B. (2007). Statistical modeling of sequential collision-induced dissociation thresholds. *J. Chem. Phys.*, 126:234302. 6, 48, 54

Armentrout, P. B., Ervin, K. M., and Rodgers, M. T. (2008). Statistical rate theory and kinetic energy-resolved ion chemistry: Theory and applications. *J. Phys. Chem. A*, 112:10071. 5, 45, 48, 54

Armstrong, D. P., Harkins, D. A., Compton, R. N., and Ding, D. (1994). Multiphoton ionization of uranium hexafluoride. *J. Chem. Phys.*, 100:28. 6, 9, 88

Beyer, T. and Swinehart, D. F. (1971). Algorithm 448: Number of multiply-restricted partitions. *Commun. ACM*, 16:379. 48

Carey, F. A. (2003). *Organic Chemistry.* McGraw Hill. 93

Carwford, O. H. and Garrett, W. R. (1977). Electron affinities of polar molecules. *J. Chem. Phys.*, 66:4968. 40

Centinkaya, B., Kind, G. H., Krishnamurthy, S. S., Lappert, M. F., and Pedley, J. B. (1971). Photoelectron spectra of electron-rich olefins and an isostructural boron compound. olefins of exceptionally low first ionization potential. *Chem. Commun.*, 21:1370. 69, 80, 83

116

Cheng, L.-T., Tam, W., Stevenson, S. H., Meredith, G. R., Rikken, G., and Marder, S. R. (1991). Experimental investigations of organic molecular nonlinear optical polarizabilities. 1. methods and results on benzene and stilbene derivatives. *J. Phys. Chem.*, 95:10631. 42

Clark, J. S. (2005). Why environmental scientists are becoming bayesians. *Ecology Letters*, 8:2. 21

Coleman, L. B., Cohen, M. J., Sandman, D. J., Yamaguchi, F. G., Garito, A. F., and Heeger, A. J. (1973). Superconducting fluctuations and the peirels instability in an organic solid. *Solid State Commun.*, 12:1125. 89

Collins, P. M., Christophorou, L. G., Chaney, E. L., and Carter, J. G. (1969). Energy dependence of the electron attachment cross section and the transient negative ion lifetime for *p*-benzoquinone and 1,4-naphtoquinone. *Chem. Phys. Lett.*, 4:10. 89

Compton, R. N. and Cooper, C. D. (1976). Negative ion properties of tetracyanoquinodimethane:electron affinity and compound states. *J. Chem. Phys.*, 66:10. 90

Compton, R. N., Jr., H. S. C., Defrancois, C., Hendricks, J. H., Lyapustina, S. A., and Bowen, K. (1996). On the binding of electrons to nitromethane: Dipole and valence bound anions. *J. Chem. Phys.*, 105:3472. 5, 43, 112

Compton, R. N., Miller, J. C., Carter, A. E., and Kruit, P. (1980). Resonantly enhanced multiphoton ionization of xenon: Photoelectron energy analysis. *Chem. Phys. Lett.*, 71:12345. 67

Cooper, J. and Zare, R. N. (1968). Angular distribution of photoelectrons. *J. Chem. Phys.*, 48:942. 66

Cordiner, M. A. and Sarre, P. J. (2007). The ch2cn- molecule: carrier of the λ8037 diffuse interstellar band? *Astron. Astrophys.*, 472:537. 9

Crawford, O. H. (1971). Negative ions of polar molecules. *Mol. Phys.*, 20:585. 40

Dalleska, N. F., Honma, K., Sunderlin, L. S., and Armentrout, P. B. (1994). Solvation of tranisition metal ions by water. sequential binding energies of m+(h2o)x (x=1-4) for m=ti to cu determined by collision-induced dissociation. *J. Am. Chem. Soc.*, 116:3519. 5, 45, 48, 54

Defrançois, C., Abdoul-Carmine, H., Khelifa, N., and Schermann, J. P. (1994). From 1/r to 1/r2 potentials: Electron exchange between rydberg atoms and polar molecules. *Phys. Rev. Lett.*, 73:2436. 4, 60

Desfrançois, C., Périquet, V., Lyapustina, S. A., Lippa, T. P., Robinson, D. W., Bowen, K. H., Nonaka, H., and Compton, R. N. (1999). Electron binding to valence and multipole states of molecules: Nitrobenzene, para- and meta-dinitrobenzenes. *J. Chem. Phys.*, 111:4569. 5, 43, 60, 112

DeTuri, V. F. and Ervin, K. M. (1998). Competitice threshold collision-induced dissociation: Gas-phase acidities and bond dissociation energies for a series of alcohols. *J. Phys. Chem. A*, 103:6911. 5, 48, 54

Do, K., Klein, T. P., Pommerening, C. A., and Sunderlin, L. S. (1997). A new flowing afterglow-guided ion beam tandem mass spectrometer. applications to the thermochemistry of polyiodide ions. *J. Am. Soc. Mass Spectrom.*, 8:688. 47

Donley, E. A., Claussen, N. R., Cornish, S. L., Roberts, J. L., Cornell, E. A., and Wieman, C. E. (2001). Dynamics of collapsin and exploding bose-einstein condesates. *Nature*, 412:295. 7

Donley, E. A., Claussen, N. R., Thompson, S. T., and Wieman, C. E. (2002). Atom-molecule coherence in a bose-einstein condensate. *Nature*, 417:529. 7

Dreuw, A. and Cederbaum, L. S. (2002). Multiply charged anions in the gas phase. *Chem. Rev.*, 102:181. 6

Ervin, K. M. (1999). Orientation effects in the direct cl- + ch3cl sn2 reaction at elevated collision energies: hard-ovid line-of-centers collision model. *Int. J. Mass Spectrom.*, 185:343. 5, 48, 54

Ervin, K. M. and Armentrout, P. B. (1985). Translational energy dependence of ar+ + xy, arx+ + y (xy = h2, d2, hd) from thermal to 30 ev c.m. *J. Chem. Phys.*, 83:166. 5, 48, 54

Farragher, A. L. and Page, F. M. (2967). Experimental determination of electron affinites. *Trans. of the Faraday Soc.*, 63:14. 89

Fermi, E. and Teller, E. (1947). The capture of negative mesotrons in matter. *Phys. Rev.*, 72:399. 40

Ferraris, J., Cowan, D. O., Walatka, V., and Perlstein, J. H. (1973). Electron transfer in a new highly conducting donor-acceptor complex. *J. Am. Chem. Soc.*, 95:948. 89, 90

Friedrich, H. (2006). *Theoretical Atomic Physics*. Springer. 65

Gaetan, A., Miroschnychenko, Y., Wilk, T., Chotia, A., Viteau, M., Comparat, D., Pillet, P., Browaeys, A., and Grangier, P. (2009). Observation of collective excitation of two individual atoms in the rydberg blockade regime. *Nature Physics*, 5:115. 87

Garrett, W. R. (1970). Critical binding of an electron to a nonstationary electric dipole. *Chem. Phys. Lett.*, 5:393. 40

Garrett, W. R. (1971). Critical binding of an electron to a rotationally excited dipolar system. *Phys. Rev. A*, 3:961. 40

Garrett, W. R. (1972). Low-energy electron-scattering by polar-molecules. *Mol. Phys.*, 24:465. 40

Garrett, W. R. (1978). Thermally stable negative ions of polar molecules. *J. Chem. Phys.*, 69:2621. 40

Garrett, W. R. (1979a). Comment on ab initio ground state potential energy surfaces for anions of polar molecules. *Chem. Phys. Lett.*, 62:325. 40

Garrett, W. R. (1979b). Permanent and induced dipole requirements in ab initio calculations of electron affinities of polar molecules. *J. Chem. Phys.*, 71:651. 40

Garrett, W. R. (1980). Critical binding of electron-dipole rotor systems; electronically excited states. *J. Chem. Phys.*, 73:5721. 40

Garrett, W. R. (1982). Excited states of polar negative ions. *J. Chem. Phys.*, 77:3666. 40

Gloaguen, E., Mestdagh, J.-M., Poisson, L., Lepetit, F., Visticot, J.-P., Soep, B., Coroiu, M., Eppink, A. T. J. B., and Parker, D. H. (2005). Experimental evidence for ultrafast electronic relaxation in molecules, mediated by diffuse states. *J. Am. Chem. Soc.*, 127:16529. 86

Gosselin, J. L. and Weber, P. M. (2005). Rydberg fingerprint spectrscopy: A new spectroscopic tool with local and global structural sensitivity. *J. Phys. Chem. A*, 109:4899. 87

Gutsev, G. L. and Adamowicz, L. (1995). Relationship between the dipole moments and the electron affinities for some polar organic molecules. *Chem. Phys. Lett.*, 235:377. 60

Hafner, H., Simpson, J. A., and Kuyatt, C. E. (1968). Comparison of the spherical deflector and the cylindrical mirror analyzers. *Rev. Sci. Instrum.*, 39:33. 32

Hammer, N. I., Diri, K., Jordan, K. D., Defrançois, C., and Compton, R. N. (2003). Dipole-bound anions of carbonyl, nitrile, and sulfoxide containing molecules. *J. Chem. Phys.*, 119:3650. 4, 60

Hammer, N. I., Hinde, R. J., Compton, R. N., Diri, K., Jordan, K. D., Radisic, D., Stokes, S. T., and Bowen, K. H. (1999). Dipole bound anions of highly polar molecules: Ethylene carbonate and vinylene carbonate. *J. Chem. Phys.*, 120:685. 4, 60

Hoops, A. A., Gascooke, J. R., Faulhaber, A. E., Kautzman, K. E., and Neumark, D. M. (2004). Two- and three-body photodissociation of gas phase i3-. *J. Chem. Phys.*, 120:7901. 47

Hori, M., Kimura, K., and Tsubomura, H. (1968). Electronic spectrum and the chemiluminescence of tetrakis(dimethylamino)ethylene (tdae). *Spectrochimica Acta, Part A*, 24:1397. 6, 71

Iceman, C. and Armentrout, P. B. (2003). Collision-induced dissocation and theoretical studies of k+ complexes with ammonia: a test of theory for potassium ions. *Int. J. Mass Spectrom.*, 222:329. 5, 48, 54

Jin, C., Haufler, R. E., Hettich, R. L., Barshick, C. M., Compton, R. N., Puretzky, A. A., Dem'yanenko, A. V., and Tuniman, A. A. (1994). Synthesis and characterization of molybdenum carbide clusters monc4n (n=1 to 4). *Science*, 263:68. 89, 90

Johnasen, H. (1975). Ab initio calculation of the electronic structure of tcnq and its ions. *Int. J. Quantum Chem.*, 9:459. 90

Jonkman, H. T., der Velde, G. A. V., and Nieuwport, W. C. (1974). Ab initio scf mo calculations of ionization energies and charge distributions of tcnq [tetracyanoquinodimethe] and its mono- and divalent anions. *Chem. Phys. Lett.*, 25:62. 90

Jonkman, H. T. and Kommandeur, J. (1972). The uvspectra and their calculation of tcnq and its mono- and di-valent anion. *Chem. Phys. Lett.*, 15:4. 90

Jortner, J., Rice, S. A., and Hochstrasser, R. M. (1969). Radiationless transitions in photochemistry. *Adv. Photochem.*, 7:149. 71

Jr., R. D. N., Jr., D. R. L., and Maryott, A. A. (1967). *Selected Values of Electric Dipole Moments for molecules in the Gas Phase*. NSRD-NBS. 60

Kawski, A., Kukliński, B., and Bojarski, P. (2006). Excited s1 state dipole moments of nitrobenzene and p-nitroaniline from thermochromic effect on electronic absorption spectra. *Chem. Phys.*, 330:307. 42

Kelly, K. L., Scharer, J. E., Paller, E. S., and Ding, G. (2002). Laser ionization and radio frequency sustainment of high-pressure seeded plasmas. *J. Appl. Phys.*, 92:698. 67

Khan, F. A., Clemmer, D. E., Schultz, R. H., and Armentrout, P. B. (1993). Sequential bond energies of chromium carbonyls (cr(co)x+, x=1-6). *J. Phys. Chem.*, 97:7978. 45

Klots, C. E. (1996). Some properties of microcanonical rate constants. *Int. Rev. Phys. Chem.*, 15:205. 48

Koizumi, H. and Armentrout, P. B. (2003). The kinetic energy dependence of assocation reactions. a new thermokinetic method for large systems. *J. Chem. Phys.*, 119:12819. 5, 48, 54

Koizumi, H., Muntean, F., and Armentrout, P. B. (2004). Reaction of cu+ with dimethoxyethane: Competition between association and multiple dissociation channels. *J. Chem. Phys.*, 120:756. 5, 48, 54

Kuyatt, C. E. and Simpson, J. A. (1967). Electron monochromator design. *Rev. Sci. Instrum.*, 38:103. 31

Lide, D. R. (1994). *CRC Handbook of Chemistry and Physics*. CRC Press. 60

Lifshitz, C., Wu, R. L. C., Tiernan, T. O., and Terwilliger, D. T. (1977). Negative ion-molecule reactions of ozone and their implications on the thermochemistry of o3-. *J. Chem. Phys.*, 68:247. 49

Linderr, L., Unge, M., Osikowicz, W., Stafstrom, S., Salaneck, W., Crispin, X., and de Jong, M. (2008). Integer charge transfer at the tetraski(dimethylamino)ethylene/au interface. *Appl. Phys. Lett.*, 92:163302. 67

Lynden-Bell, R. M., Kosloff, R., Ruhman, S., Danovich, D., and Vala, J. (1998). Does solvation cause symmetry breaking in the i3- ion in aqueous solution? *J. Chem. Phys.*, 109:9928. 45, 47

Milían, B., Pou-Amérigo, R., Viruela, R., and Ortí, E. (2004). A theoretical study of neutral and reduced tetracyano-*p*-quinodimethane (tcnq). *J. Mo. Structure*, 709:97. 90

Miller, J. C. and Compton, R. N. (1982). Third-harmonic generation and multiphoton ionization in rare gases. *Phys. Rev. A*, 25:2056. 67

Mirsaleh-Kohan, N., D.Robertson, W., Lambert, J., Compton, R. N., Krasnokutski, S. A., and Yang, D.-S. (2011). Ionic and vibrational properties of an ultra-low ionization potential molecule: Tetrakis(dimethylamino)ethylene. *Int. J. Mass Spectrom.*, 304:57. 67, 69, 86

Muntean, F. and Armentrout, P. B. (2001). Guided ion beam study of collision-induced dissociation dynamics: integral and differential cross sections. *J. Chem. Phys.*, 115:1213. 45

Myers, R. H. (1986). *Classical and modern regression with applications.* Duxbury Classic Series. 52, 108

Nakato, Y., Ozaki, M., and Tsubomura, H. (1972). Ionization energies and rydberg states of tetraaminoethylenes. *Bull. Chem. Soc. Japan*, 45:1299. 69, 80, 83

Nalley, S. J., Compton, R. N., Schweinler, H. C., and Anderson, V. E. (1973). Molecular electron affinities from collisional ionization of cesium. i. nitric oxide, nitrogen dioxide, and nitrous oxide. *J. Chem. Phys.*, 59:4125. 49

Narancic, S., Bach, A., and Chen, P. (2007). Simple fitting of energy-resolved reactive cross sections in threshold collision-induced dissocation (t-cid) experiments. *J. Phys. Chem. A*, 111:7006. 49, 50

Nicolaides, C. A. and Beck, D. R. (1976). On collective excitations in atoms and molecules. *J. Phys. B*, 9:L259. 6, 87

Nielsen, S. B. and Nielsen, M. B. (2003). Experimental evidence for the 7,7,8,8-tetracyano-*p*-quinodimethane (tcnq). *J. Chem. Phys.*, 199:19. 90, 91

Ovchinnikov, S. Y., Macek, J., Tuinman, A. A., Steill, J. D., Compton, R. N., Hvelplund, P., Holm, A. I. S., Nielsen, S. B., and Nielsen, M. B. (2006). Quantum phase interference effects in anion to dianion charge-exchange collisions. *Phys. Rev. A*, 73:064704. 92, 105

Panja, S., Kadhane, U., Andersen, J. U., Holm, A. I. S., Hvelplund, P., Kirketerp, M.-B. S., Nielsen, S. B., Stochkel, K., Compton, R. N., Forster, J. S., Kilsa, K., and Nielsen, M. B. (2007). Dianions of 7,7,8,8-tetracyano-*p*-quinodimethane: Information on excited states from lifetime measurements in an electrostatic storage ring and optical absorption spectroscopy. *J. Chem. Phys.*, 127:124301. 91, 92

Papajak, E. and Truhlar, D. G. (2010). Efficient diffuse basis sets for density functional theory. *J. Chem. Theor. Comp.*, 6:597. 42

Pruett, R. L., Barr, J. T., Rapp, K. E., Bahner, C. T., Gibson, J. D., and Lafferty, R. H. (1950). Reactions of polyfluoro olefins. ii. reactions with primary and secondary amines. *J. Am. Chem. Soc.*, 72:3646. 69

Purcell, E. M. (1953). The focusing of charged particles by a spherical condenser. *Phys. Rev.*, 54:818. 27

Rabie, U. (2012). Methanolisis of 7,7,8,8-tetracyanoquinodimethane: A consequence of an initial charge transfer complexation. *Bull. Korean Chem. Soc.*, 33:3448. 93

Roberts, J. L., Claussen, N. R., Cornish, S. L., Donley, E. A., Cornell, E. A., and Wieman, C. E. (2001). Controlled collapse of a bose-einstein condensate. *Phys. Rev. Lett.*, 86:4211. 7

Rodgers, M. T., Ervin, K. M., and Armentrout, P. B. (1997). Statistical modeling of collision-induced dissociation thresholds. *J. Chem. Phys.*, 106:4499. 5, 45, 48, 54

Sarre, P. J. (2000). The diffuse interstellar bands. a dipole-bound state hypothesis. *Mon. Not. R. Astron. Soc.*, 313:L14. 9

Schroder, D. and Schwarz, H. (1999). Generation, stability, and reactivity of small, multiply charged ions in the gas phase. *J. Chem. Phys.*, 103:7358. 6

Schultz, R. H., Crellin, K. C., and Armentrout, P. B. (1991). Sequential bond energies of iron carbonyl fe(co)x+ (x=1-5): systematic effects on collision-induced dissociation measurements. *J. Am. Chem. Soc.*, 113:8590. 5, 48, 54

Seber, G. A. F. and Wild, C. J. (1989). *Nonlinear Regression.* Wiley series in probability and mathematical statistics. 13, 15

Smith, B. H., Buonaugurio, A., Chen, J., Collins, E., Bowen, K. H., Compton, R. N., and Sommerfeld, T. (2013). Negative ions of p-nitroaniline: photodetachment, collisions, and *Ab Initio* calculations. *J. Chem. Phys.*, 138:234304. 5

Soep, B., Mestdagh, J. M., Sorgues, S., and Visticot, J. P. (2001). Femtosecond to nanosecond relaxation time scales in electronically excited tetrakis(dimethylamino)ethylene: Identification of the intermediates. *Eur. Phys. J. D*, 14:191. 71

Soscún, H., Castellano, O., Bermúdez, Y., Toro, C., Cubilln, N., Hinchliffe, A., and Phu, X. N. (2006). B3lyp study of the dipole moment and the static dipole (hyper)polarizabilities of para-nitroaniline in gas phase. *Int. J. Quant. Chem.*, 106:1130. 42

Stokes, S. T., Bowen, K. H., Sommerfeld, T., Ard, S., Mirsaleh-Kohan, N., Steill, J. D., and Compton, R. N. (2008). Negative ions of nitroethane and its clusters. *J. Chem. Phys.*, 129:064308. 5, 43, 112

Su, T. (1994). Parameterization of kinetic energy dependencies of ion-polar molecule collision rate constants by trajectory calculations. *J. Chem. Phys.*, 100:4703. 5, 48, 54

Tanemura, K., Nishida, Y., Suzuki, T., Satsumabayashi, K., and Horaguchi, T. (1999). Cleavage of protexting groups catalyzed by π-acceptors. *J. Chem. Research (S)*, page 40. 92, 93

Tao, J., Perdew, J. P., Staroverov, V. N., and Scuseria, G. E. (2003). Climbind the density functional ladder: Nonempirical meta-generalized gradient approximation designed for molecules and solids. *Phys. Rev. Lett.*, 91:146401. 42

Wang, L.-S., Ding, C.-F., Wang, X.-B., and Nicholas, J. B. (1998). Probing the potential barriers and intramolecular electrostatic interactions in free doubly charged anions. *Phys. Rev. Lett.*, 81:13. 6

Wannberg, B., Gelius, U., and Siegbahn, K. (1974). Design parameters in electron spectrometry. *Journal of Physics E*, 7:149. 32

Wannberg, B. and Skollermo, A. (1977). Computer optimizations of retarding lens systems for esca spectrometers. *J. Elec Spec and Related Phenomena*, 10:45. 33

Webe, M. E., Elking, J. L., and Armentrout, P. B. (1986). Kinetic energy dependence of aluminum (1+) + molecular oxygen, oxaluminum(1+) + atomic oxygen. *J. Chem. Phys.*, 84:1521. 5, 48, 54

Weigend, F. and Ahlrichs, R. (2005). Balanced basis sets of split valence, triple zeta valence and quadruple zeta valence quality for h to rn: Design and assessment of accuracy. *Phys. Chem. Chem. Phys.*, 7:3297. 42

Wiberg, N. and Bulcher, J. W. (1962). Tetrakis(dimethylamino)ethylene: A strong electron donor. *Angew. Chem.*, 74:490. 69

Wiberg, N. and Bulcher, J. W. (1964). Tetrakis(dimethylamino)ethylene. iii. *Z. Naturforsch.*, 19b:5. 69

Woodwort, J. R., Green, T. A., and Frost, C. A. (1985). Ionization of organic molecules with ultraviolet lasers: A technique for generating large, well-defined ionized volumes. *J. Appl. Phys.*, 57:1648. 67

Yatsuhashi, T., Obayashi, T., Tanaka, M., Murakami, M., and Nakashima, N. (2006). Femtosecond laser ionization of organic amine with very low ionization potentials: Relatively small suppressed ionization features. *J. Phys. Chem. A*, 110:7763. 86

Zakrewski, V. G., Dolgounitcheva, O., and Ortiz, J. V. (1996). Electron binding energies of tcnq and tcne. *J. Chem. Phys*, 105:14. 90

Zhang, Y. S. and Scharer, J. E. (1993). Plasma generation in an organic molecular gas by an ultraviolet laser pulse. *J. Appl. Phys.*, 73:4779. 67

Appendix

Appendix

R Code

Collision Induced Dissociation Cross-Section

```
library(msm)
library(scatterplot3d)
library(rgl)


##  The function being fit is a typical line-of-centers cross-section
## where a fudge factor exponent is used to model empirical data.
## This is a piecewise function with three fit parameters, a scaling
## coefficient, a threshold energy, and the aforementioned exponent.
## Then, the cross-section is convoluted over
## a Normal distribution.

#f_expr <- function(x, params){
#
# y <- ((x-params[2]) > 0) * (x-params[2])
# params[1]/x*y^params[3]
#
#}
```

```
##  This f_expr is used to fit the convoluted data.  Note that
## Tiernan's convolution integral is actually done in the lab frame
## and so I had to transform the integral to do the fit in the Center
## of Mass frame.
## Calculations are slow.


f_expr <- function(x2, params){

vals <- rep(0, length(x2))
S <- 0.3
a <- 39.944/(380.7*8.6173*10^(-5)*298.15)
m <- 39.944/(39.944+380.7)
for(i in 1:length(x2)){
integrand <- function(x){dnorm(x2[i], x,
m*sqrt(S^2+4*x/(m*a))/sqrt(2))*params[1]/x*(x-params[2])^params[3]}
vals[i] <- integrate(integrand, lower=params[2], upper=Inf)$value
}
vals


}



##  This calculates the log-posterior which is then sampled through
## the MCMC. I've chosen to use the log of the posterior because it
## will take exceptionally small values, below the limits of R.  Note
## that the 'Weighted' fitting appears to give the results which
## are most consistent with CRUNCH or nls when including the weights
## exp(-x^2).
```

```
log_post <- function(data, params, priors){

N <- length(data[,1])


## -N/2*log(2*pi*0.5^2) -
1/(2*0.5^2)*sum((data[,2]-f_expr(data[,1], params))^2) +
## log(dnorm(params[1], priors[1,1], priors[1,2])) +
## log(dnorm(params[2], priors[2,1], priors[2,2])) +
## log(dnorm(params[3], priors[3,1], priors[3,2]))


##Weighted
## -N/2*log(2*pi*0.25^2) - 1/(2*0.25^2)*sum((data[,2]-f_expr(data[,1],
 params))^2*exp(-data[,1]^2)) +
## log(dnorm(params[1], priors[1,1], priors[1,2])) +
## log(dnorm(params[2], priors[2,1], priors[2,2])) +
## log(dnorm(params[3], priors[3,1], priors[3,2]))


##Weighted 2
## sigmasq <- 0.5^2/exp(-(data[,1]^2)
## -1/2*sum(log(2*pi*sigmasq)) - 1/2*sum((data[,2]-f_expr(data[,1],
 params))^2/sigmasq) +
## log(dnorm(params[1], priors[1,1], priors[1,2])) +
## log(dnorm(params[2], priors[2,1], priors[2,2])) +
## log(dnorm(params[3], priors[3,1], priors[3,2]))


##Weighted 3
## -N/2*log(2*pi*0.25^2) -
1/(2*0.25^2)*sum((data[,2]-f_expr(data[,1],params))^2*exp(-data[,1]^2)) +
```

```
## log(dgamma(params[1], priors[1,1]*0.1, 0.1)) +
## log(dgamma(params[2], priors[2,1]*0.1, 0.1)) +
## log(dgamma(params[3], priors[3,1]*0.1, 0.1))


##Weighted 4
## sigmasq <- 0.25^2/exp(-data[,1]^2)
## -1/2*sum(log(2*pi*sigmasq)) -
1/2*sum((data[,2]-f_expr(data[,1],params))^2/sigmasq) +
## log(dgamma(params[1], priors[1,1]*0.1, 0.1)) +
## log(dgamma(params[2], priors[2,1]*0.1, 0.1)) +
## log(dgamma(params[3], priors[3,1]*0.1, 0.1))


##Weighted 5
-1/2*sum(log(2*pi*exp(-data[,1]^2)/params[4])) -
 params[4]/2*sum((data[,2]-f_expr(data[,1], params))^2*exp(-data[,1]^2)) +
# dgamma(params[1], shape=0.1, scale=100, log=TRUE) +
dgamma(params[2], shape=0.1, scale=100, log=TRUE) +
dgamma(params[3], shape=0.1, scale=100, log=TRUE)




}


##  This function simply runs the iterative MCMC to sample the posterior.
## The final fit parameters are then the average over the sample less
## the burn.in period.
```

```
fitter <- function(data, priors, num.iter){


burn.in <- round(num.iter/25)

samps <- matrix(0, num.iter, 5)

samps[1,] <- c(priors[, 1], 0.5, -1E7)

tuning <- c(1, 0.05, 0.25)


for(i in 2:num.iter){


samps[i,] <- samps[i-1,]


beans <- f_expr(data[,1], samps[i,])/samps[i,1]

mean1 <- (-0.1/samps[i,4]+sum(data[,2]*beans*exp(-data[,1]^2)))

/(sum(beans^2*exp(-data[,1]^2)))

var1 <- 1/(samps[i,4]*sum(beans*exp(-data[,1]^2)))

samps[i,1] <- rnorm(1, mean1, sqrt(var1))


for(j in 2:3){


if(j==2){samps[i,5] <- log_post(data, samps[i,], priors)}


new <- samps[i, ]

new[j] <- rtnorm(1, samps[i,j], tuning[j], lower=0, upper=Inf)

new[5] <- log_post(data, new[1:4], priors)


u <- runif(1)

rat <- dtnorm(samps[i,j], new[j], 1.0)/dtnorm(new[j], samps[i,j], 1.0)

if(log(u) < new[5] - samps[i,5] + log(rat)){samps[i,] <- new}
```

```
}


shapesigma=length(data[,1])/2
    scalesigma=.5*sum((data[,2]-f_expr(data[,1], samps[i,1:3]))^2
  *exp(-data[,1]^2))
        sigma=rgamma(1,shape= shapesigma,scale=1/scalesigma)
        samps[i,4]=sigma


}


## apply(samps[-(1:burn.in),], 2, mean)[1:3]


N <- num.iter-burn.in
apply(samps[seq(burn.in, N, 30),], 2, mean)[1:4]
 #  Attempting to deal with auto-correlation


}


grids <- function(data, priors){

sigma_vals <- seq(7.0, 20.0, 0.5)
E_vals <- seq(0.6, 1.5, 0.05)
n_vals <- seq(1.0, 2.3, 0.05)
N <- length(sigma_vals)*length(E_vals)*length(n_vals)
beans <- 1


samps <- matrix(0, length(sigma_vals)*length(E_vals)*length(n_vals), 4)


for(i in sigma_vals){
```

```
for(j in E_vals){
for(k in n_vals){samps[beans, 1:3] <- c(sigma_vals[i], E_vals[j], n_vals[k])
beans <- beans+1}
}
}


for(loops in 1:N){samps[loops, 4] <- log_post(data, samps[loops, 1:3], priors)}
samps



}


## These are the prior means and standard deviations
## (dnorm uses sd's isntead of variances).


priors <- cbind(c(10, 1.1, 1.5), c(300, 300, 300))


##Unadjusted Energy
energy <-
c(0.284877474,0.332357053,0.379836631,0.42731621,0.474795789,0.522275368,
0.569754947,0.617234526,0.664714105,0.712193684,0.759673263,0.807152842,
0.854632421,0.902112,0.949591579,0.997071158,1.044550736,1.092030315,
1.139509894,1.186989473,1.234469052,1.281948631,1.32942821,1.376907789,
1.424387368,1.471866947,1.519346526,1.566826105,1.614305684,1.661785263,
1.709264842,1.75674442,1.804223999,1.851703578,1.899183157,1.946662736,
1.994142315,2.041621894,2.089101473,2.136581052,2.184060631,2.23154021,
2.279019789,2.326499368,2.373978947,2.421458525,2.468938104,2.516417683)


##Adujusted Energy (for later thermal corrections)
```

```
energy2 <- c(0.5594277176,0.6039832981,0.6488856692,0.6940873403,0.7395464501,
0.7852269208,0.8310968300,0.8771357529,0.9233229764,0.9696356190,1.016059988,
1.062584146,1.109191764,1.155881385,1.202633171,1.249446933,1.296313252,
1.343230286,1.390188620,1.437184889,1.484216512,1.531281237,1.578375811,
1.625489138,1.672626699,1.719784802,1.766974796,1.814172429,1.861375599,
1.908615016,1.955856536,2.003106397,2.050378220,2.097659678,2.144935994,
2.192246522,2.239548654,2.286862327,2.334175591,2.381512707,2.428841436,
2.476175278,2.523527446,2.570879397,2.618241975,2.665601160,2.712961974,
2.760326198)


XSectionR <-
c(0,0,0,0.222691341,0.312847818,0.372806444,0.477835645,0.654118536,
0.844084713,1.181251625,1.534837567,1.866143092,2.431945881,3.052661403,
4.095970308,5.517380082,6.676102028,8.611373188,10.48470445,12.58106413,
15.76682783,18.1784481,21.27782955,25.07699535,28.53801593,32.48988813,
37.4040081,40.20908419,45.25825336,49.12880167,54.40134261,57.67218474,
62.20306329,65.05774414,67.71377623,70.98478852,73.41890941,76.55278113,
80.03012161,81.61782573,83.37123148,85.03681695,86.80709099,88.36848933,
89.66486775,90.57093919,91.8175225,92.98162025)
data <- cbind(energy, XSectionR)
data[,2] <- data[,2]/10  #  I rescale the data to make fitting work better.
data <- data[-c(44, 45, 46, 47, 48),]  #  Cleaving some of the data to make
the fitting work more like CRUNCH.


vals <- fitter(data, priors, 10000)
plot(data)


curve(f_expr(x, vals), add=T)
```

```
##  As a comparison I fit and plot using the nls non-linear regression function.


x <- data[,1]
y <- data[,2]
vals2 <- nls(y ~ f_expr(x, c(a,b,c)), start=list(a=vals[1], b=vals[2],
 c=vals[3]), weights=exp(-data[,1]^2))
curve(f_expr(x, coef(vals2)), add=T)



XSection3 <-
c(0.0,0.0,0.0,0.05875360499,0.09580206163,0.1293376514,0.1843123905,
0.2763686183,0.3859607317,0.5788088453,0.7993334501,1.025864469,1.402937483,
1.838771771,2.565041954,3.578728605,4.470453200,5.935813941,7.420539809,
9.121880934,11.68750610,13.75180037,16.40022640,19.66445631,22.73732369,
26.26950226,30.65746703,33.37531718,38.00915649,41.71147064,46.65815465,
49.93208309,54.33022057,57.29123389,60.08812763,63.44252371,66.05780013,
69.30916291,72.88242666,74.73649251,76.73480461,78.64521696,80.64547298,
82.44435339,83.98696983,85.15292503,86.62820963,88.01615231)
data2 <- cbind(energy, XSection3)
data2[,2] <- data2[,2]/10
data2 <- data2[-c(44, 45, 46, 47, 48),]


##The 'unconvoluted cross-section' given by CRUNCH
XSection4 <-
c(0,0,0,0,0,0,0,0,0,0,0,0,0,0,0,0,0,0.0056017351,0.15918793,0.40009210,
0.68847316,1.0073350,1.3466953,1.7000045,2.0627029,2.4315021,2.8039724,
3.1782917,3.5530750,3.9272634,4.3000440,4.6707909,5.0390262,5.4043831,
5.7665849,6.1254258,6.4807550,6.8324693,7.1804987,7.5248029,7.8653647,
8.2021824,8.5352798,8.8646774)
```

```
data3 <- cbind(energy[1:length(XSection4)], XSection4)
plot(data)
points(data3)
```

Landau-Zener Cross-Section

```
library(Hmisc)
library(msm)


m <- 204.19/(6.022*10^(23)*9.11*10^(-28)) #Mass of TCNQ per molecule
x <- (5.2377,6.5056,7.1396,7.9396,9.0521,10.1434,15.1094,25.2226,35.4112,
40.6188,50.8678,60.8451,70.8979,81.0866,91.0941)*1000/27.2107
y <- c(1.1598, 1.2747, 1.2699, 1.3283, 1.1853, 1.2003, 1.0012, 0.8429, 0.8324,
 0.7382, 0.6438, 0.6036, 0.5799, 0.5703, 0.5199)
v <- sqrt(2*x/m) #Corresponding velocity in the Lab frame
vars <- c(0.1035, 0.0895, 0.0876, 0.0195, 0.1931, 0.0873, 0.0458, 0.0192,
 0.0146, 0.0192, 0.1692, 0.0873, 0.0327, 0.1340, 0.0911)/2
#var <- 0.03


##  The Landau-Zener model for the collisional charge transfer cross-section.


#f_expr <- function(Q, R, v){2*pi*R^2*exp(-Q/v)*(1-exp(-Q/v))}
f_expr <- function(Q, R, v){2*pi*R*exp(-Q/v)*(1-exp(-Q/v))}


##  A function which calculates the log-likelihood
```

```
log_likes <- function(x, y, params){

N <- length(x)
-N/2*log(2*pi/params[3]) - params[3]/2
*sum((y-f_expr(params[1], params[2], x))^2)

}


##  A function which evaluates the posterior.  The prior distributions that are
## are gamma(1,beta) for R and a truncated normal distribution for the Q
## parameter.  This allows us to constrain the parameters to positive values
## through the distributions.

log_post <- function(x, y, params){

beta <- 0.9
return(log_likes(x, y, params)
   + log(dgamma(params[2], 1, 1/beta))
   + log(dtnorm(params[1], mean=1.6, sd = 1, lower=0))
   + log(dgamma(params[3], 1, 1/0.17)))

}


##  The first fit is simply a grid-search for the parameters.


Qvals <- seq(0.00001, 0.01, by=0.0002)
Rvals <- seq(0.01, 2.0, by=0.002)
```

```
sols <- matrix(0, length(Qvals)*length(Rvals), 3)
looper <- 1


for(i in Qvals){
for(j in Rvals){ sols[looper,] <- c(i, j, sum((y-f_expr(i, j, v))^2))
    looper <- looper+1}
}


best_sol <- which(sols[,3] == min(sols[,3]))
sols[best_sol,]
curve(f_expr(sols[best_sol,1], sols[best_sol,2], x), add=TRUE)



##  The second fit uses the Discrete Approximation.  This is simply
## a posterior-weighted grid search.

Qvals <- seq(0.00001, 0.01, by=0.0002)
Rvals <- seq(0.01, 2.0, by=0.002)


sols2 <- matrix(0, length(Qvals)*length(Rvals), 3)
looper <- 1


for(i in Qvals){
for(j in Rvals){sols2[looper,] <- c(i, j, exp(log_likes(v, y, c(i,j,0.25))))
    looper <- looper+1}
}


best_sol2 <- c(sum(sols2[,3]*sols2[,1])/sum(sols2[,3]),
```

```
  sum(sols2[,3]*sols2[,2])/sum(sols2[,3]))
best_sol2
curve(f_expr(best_sol2[1], best_sol2[2], x), add=TRUE, col="red")



##  Finally We have a fully Bayesian fit using the Gibbs sampler for the R
## parameter and the Metropolis-Hastings algorithm for the Q parameter.
## This is done using the truncated normal distribution to take
## the random steps in order to keep the parameter positive.


n.iter <- 10000
burn.in <- 250


sols3 <- matrix(0, n.iter, 4)
sols3[1,-4] <- sols[best_sol,-4]
sols3[1,4] <- log_post(x, y, sols[best_sol,])


R_prior <- sols[best_sol,2]
Chi_prior <- 1/sum((y-f_expr(sols[best_sol,1], sols[best_sol,2], v))^2)
sols3[1,3] <- Chi_prior




for(i in 2:n.iter){

sols3[i,] <- sols3[i-1,]
prop <- sols3[i,]
prop[1] <- rtnorm(1, sols3[i,1], 0.5, lower=0, upper=Inf)
prop[4] <- log_post(v, y, prop[-4])
```

```
u <- log(runif(1))
if(u < (prop[4] - sols3[i,4] - dtnorm(prop[1], sols3[i,1], 0.5) +
  dtnorm(sols3[i, 1], prop[1], 0.5))){sols3[i,] <- prop}


R_b <- sols3[i,3]*sum(f_expr(sols3[i,1], 1, v)^2)
R_a <- (-1/R_prior + sols3[i,3]*sum(y*f_expr(sols3[i,1], 1, v)))/(R_b)
R_b <- 1/sqrt(R_b)
sols3[i,2] <- rtnorm(1, R_a, R_b, lower=0, upper=Inf)
# sols3[i,2] <- rnorm(1, R_a, R_b)


SSE <- sum((y-f_expr(sols3[i,1], sols3[i,2], v))^2)
N <- length(y)
sols3[i,3] <- rgamma(1, N/2 + Chi_prior, 1+1/2*SSE)




}


best_sol3 <- apply(sols3[-(1:burn.in),], 2, mean)
best_sol3[4] <- sum((y-f_expr(best_sol3[1], best_sol3[2], v))^2)
best_sol3
curve(f_expr(best_sol3[1], best_sol3[2], x), add=TRUE, col="blue")
```

```
##Plotting the function


jpeg(filename = "CrossSection.jpg", height=6.9, width=6.9, units="cm",
 pointsize=8, res=600)
plot(v, y, xlab="Lab Frame Energy (eV)", ylab="Cross-section (Mb)")
curve(f_expr(sols[best_sol,1], sols[best_sol,2], x), add=TRUE)
curve(f_expr(best_sol2[1], best_sol2[2], x), add=TRUE, col="red")
curve(f_expr(best_sol3[1], best_sol3[2], x), add=TRUE, col="blue")
dev.off()
```

Gaussian Code for Optimized Energy and Vibrational Frequencies

```
                                      A2      118.91674
p-Nitroaniline                        B3        1.40226
B3LYP/6-311+G*                        A3      122.22483
                                      D3      359.97438
                                      B4        1.37614
Deprotonated p-Nitroaniline Neutral   A4      118.93480
B3LYP/6-311+G*                        D4        0.02562
                                      B5        1.43498
C                                     A5      121.18939
C    1 B1                             D5      359.97438
C    2 B2 1 A2                        B6        1.47196
C    3 B3 2 A3 1 D3                   A6      118.98826
C    4 B4 3 A4 2 D4                   D6      180.02562
C    1 B5 2 A5 3 D5                   B7        1.33185
N    3 B6 2 A6 1 D6                   A7      117.73701
N    6 B7 1 A7 2 D7                   D7      179.97438
O    7 B8 3 A8 2 D8                   B8        1.22584
O    7 B9 3 A9 2 D9                   A8      117.63025
H    1 B10 2 A10 3 D10                D8      359.97438
H    2 B11 1 A11 3 D11                B9        1.22642
H    4 B12 3 A12 2 D12                A9      117.63099
H    5 B13 4 A13 3 D13                D9      180.02562
H    8 B14 6 A14 1 D14                B10       1.08359
Variables:                            A10     121.28897
B1        1.37645                      D10     180.02562
B2        1.40150                      B11       1.08176
```

```
A11        121.67989
D11        179.97438
B12          1.08191
A12        119.34890
D12        179.97438
B13          1.08574
A13        120.02063
D13        180.02562
B14          1.02422
A14        110.07314
D14        180.02562


Deprotonated p-Nitroaniline Anion
B3LYP/6-311+G*

C
C    1 B1
C    2 B2 1 A2
C    3 B3 2 A3 1 D3
C    4 B4 3 A4 2 D4
C    1 B5 2 A5 3 D5
N    3 B6 2 A6 1 D6
N    6 B7 1 A7 2 D7
O    7 B8 3 A8 2 D8
O    7 B9 3 A9 2 D9
H    1 B10 2 A10 3 D10
H    2 B11 1 A11 3 D11
H    4 B12 3 A12 2 D12
H    5 B13 4 A13 3 D13
H    8 B14 6 A14 1 D14
Variables:
B1          1.36553
B2          1.42112
A2        120.90638
B3          1.41709
A3        118.59203
D3        359.97438
B4          1.36776
A4        120.76604
D4          0.02562
B5          1.45309
A5        122.58247
D5          0.02562
B6          1.40170
A6        120.80997
D6        180.02562
B7          1.31466
A7        119.83420
D7        180.02562
B8          1.25591
A8        119.35982
D8          0.02562
B9          1.25661
```

```
A9         119.43183
D9         179.97438
B10          1.08597
A10        120.62203
D10        179.97438
B11          1.08338
A11        120.88698
D11        180.02562
B12          1.08358
A12        118.29039
D12        180.02562
B13          1.08901
A13        119.59261
D13        179.97438
B14          1.02379
A14        109.17844
D14        179.97438


p-Nitroaniline   Anion without HNO
B3LYP/6-311+G*

H
C    1 B1
C    2 B2 1 A2
H    3 B3 2 A3 1 D3
C    3 B4 2 A4 1 D4
C    5 B5 3 A5 2 D5
H    6 B6 5 A6 3 D6
C    6 B7 5 A7 3 D7
H    8 B8 6 A8 5 D8
C    8 B9 6 A9 5 D9
N    10 B10 8 A10 6 D10
H    11 B11 10 A11 8 D11
O    5 B12 3 A12 2 D12
Variables:
B1          1.08988
B2          1.37375
A2        119.78193
B3          1.08714
A3        120.69770
D3          0.02562
B4          1.44784
A4        122.63416
D4        180.02562
B5          1.44986
A5        114.31246
D5        359.97438
B6          1.08709
A6        116.53505
D6        180.02562
B7          1.37093
A7        122.85378
D7          0.02562
```

```
B8          1.08681          B8          1.40015
A8        120.76114          A8        118.34457
D8        179.97438          D8          0.25523
B9          1.44082          B9          1.20616
A9        122.60143          A9        110.32086
D9        359.97438          D9        180.02562
B10         1.33749          B10         1.08642
A10       119.72300          A10       119.89463
D10       179.97438          D10       180.02562
B11         1.02346          B11         1.08397
A11       108.45707          A11       119.92080
D11       179.97438          D11       179.97438
B12         1.26741          B12         1.08747
A12       122.81756          A12       118.62491
D12       180.02562          D12       179.97438
                             B13         1.08909
p-Nitroaniline NO loss Rearrangement   A13   119.24139
B3LYP/6-311+G*               D13       179.97438
                             B14         1.02388
C                            A14       108.90553
C    1 B1                    D14         0.02562
C    2 B2 1 A2
C    3 B3 2 A3 1 D3
C    4 B4 3 A4 2 D4          p-Nitroaniline Neutral with HNO2
C    5 B5 4 A5 3 D5          B3LYP/6-311+G*
O    3 B6 2 A6 1 D6
N    6 B7 5 A7 4 D7          C
N    7 B8 3 A8 2 D8          C    1 B1
O    9 B9 7 A9 3 D9          C    2 B2 1 A2
H    1 B10 2 A10 3 D10       C    3 B3 2 A3 1 D3
H    2 B11 1 A11 3 D11       C    4 B4 3 A4 2 D4
H    4 B12 3 A12 2 D12       C    5 B5 4 A5 3 D5
H    5 B13 4 A13 3 D13       N    6 B6 5 A6 4 D6
H    8 B14 6 A14 5 D14       H    1 B7 2 A7 3 D7
Variables:                   H    2 B8 1 A8 3 D8
B1          1.37921          H    4 B9 3 A9 2 D9
B2          1.40580          H    7 B10 6 A10 5 D10
A2        120.12303          H    7 B11 6 A11 5 D11
B3          1.39972          Variables:
A3        119.22477          B1          1.40226
D3          0.02562          B2          1.36902
B4          1.38243          A2        113.54144
A4        120.88611          B3          1.34755
D4        359.97438          A3        148.10091
B5          1.44670          D3          0.65063
A5        122.53810          B4          1.35135
D5        359.97438          A4         85.42620
B6          1.39258          D4          0.02562
A6        125.02062          B5          1.37951
D6        180.02562          A5        147.58443
B7          1.32771          D5        359.32852
A7        126.40483          B6          1.41236
D7        180.02562          A6        123.27075
                             D6        183.84493
```

145

```
B7         1.08942          H   13 B34 3 A34 1 D34
A7       124.03537          H   14 B35 3 A35 1 D35
D7       178.67917          H   14 B36 3 A36 1 D36
B8         1.08413          H   14 B37 3 A37 1 D37
A8       123.70510          Variables:
D8       180.61515          B1         1.36745
B9         1.08378          B2         1.41347
A9       137.61454          A2       123.66701
D9       180.44743          B3         1.41347
B10        1.01014          A3       123.66701
A10      113.14345          D3       328.54321
D10      341.10968          B4         1.41347
B11        1.01127          A4       123.66701
A11      113.86389          D4       148.54321
D11      214.07736          B5         1.41347
                            A5       123.66701
TDAE Neutral                D5       179.97438
B3LYP/6-311+G*              B6         1.45367
                            A6       119.88817
C                           D6       122.64704
C   1 B1                    B7         1.44702
N   1 B2 2 A2               A7       120.67733
N   2 B3 1 A3 3 D3          D7       323.91192
N   2 B4 1 A4 3 D4          B8         1.45367
N   1 B5 2 A5 3 D5          A8       119.88817
C   5 B6 2 A6 1 D6          D8       122.64704
C   5 B7 2 A7 1 D7          B9         1.44702
C   4 B8 2 A8 1 D8          A9       120.67733
C   4 B9 2 A9 1 D9          D9       323.91192
C   6 B10 1 A10 2 D10       B10        1.44702
C   6 B11 1 A11 2 D11       A10      120.67733
C   3 B12 1 A12 2 D12       D10      323.91192
C   3 B13 1 A13 2 D13       B11        1.45367
H   7 B14 5 A14 2 D14       A11      119.88817
H   7 B15 5 A15 2 D15       D11      122.64704
H   7 B16 5 A16 2 D16       B12        1.45367
H   8 B17 5 A17 2 D17       A12      119.88817
H   8 B18 5 A18 2 D18       D12      122.64704
H   8 B19 5 A19 2 D19       B13        1.44702
H   9 B20 4 A20 2 D20       A13      120.67733
H   9 B21 4 A21 2 D21       D13      323.91192
H   9 B22 4 A22 2 D22       B14        1.09043
H   10 B23 4 A23 2 D23      A14      109.01522
H   10 B24 4 A24 2 D24      D14       28.09252
H   10 B25 4 A25 2 D25      B15        1.10189
H   11 B26 6 A26 1 D26      A15      113.13330
H   11 B27 6 A27 1 D27      D15      267.36043
H   11 B28 6 A28 1 D28      B16        1.09598
H   12 B29 6 A29 1 D29      A16      110.14664
H   12 B30 6 A30 1 D30      D16      146.75372
H   12 B31 6 A31 1 D31      B17        1.09176
H   13 B32 3 A32 1 D32      A17      109.43810
H   13 B33 3 A33 1 D33      D17      329.14782
```

```
B18        1.10022          D35        329.14782
A18      114.30042          B36          1.10022
D18       90.29289          A36        114.30042
B19        1.09717          D36         90.29289
A19      109.35960          B37          1.09717
D19      210.51180          A37        109.35960
B20        1.09043          D37        210.51180
A20      109.01522
D20       28.09252          TDAE Cation
B21        1.10189          B3LYP/6-311+G*
A21      113.13330
D21      267.36043          C
B22        1.09598          C    1 B1
A22      110.14664          N    1 B2 2 A2
D22      146.75372          N    2 B3 1 A3 3 D3
B23        1.09176          N    2 B4 1 A4 3 D4
A23      109.43810          N    1 B5 2 A5 3 D5
D23      329.14782          C    5 B6 2 A6 1 D6
B24        1.10022          C    5 B7 2 A7 1 D7
A24      114.30042          C    4 B8 2 A8 1 D8
D24       90.29289          C    4 B9 2 A9 1 D9
B25        1.09717          C    6 B10 1 A10 2 D10
A25      109.35960          C    6 B11 1 A11 2 D11
D25      210.51180          C    3 B12 1 A12 2 D12
B26        1.09176          C    3 B13 1 A13 2 D13
A26      109.43810          H    7 B14 5 A14 2 D14
D26      329.14782          H    7 B15 5 A15 2 D15
B27        1.09717          H    7 B16 5 A16 2 D16
A27      109.35960          H    8 B17 5 A17 2 D17
D27      210.51180          H    8 B18 5 A18 2 D18
B28        1.10022          H    8 B19 5 A19 2 D19
A28      114.30042          H    9 B20 4 A20 2 D20
D28       90.29289          H    9 B21 4 A21 2 D21
B29        1.09043          H    9 B22 4 A22 2 D22
A29      109.01522          H   10 B23 4 A23 2 D23
D29       28.09252          H   10 B24 4 A24 2 D24
B30        1.09598          H   10 B25 4 A25 2 D25
A30      110.14664          H   11 B26 6 A26 1 D26
D30      146.75372          H   11 B27 6 A27 1 D27
B31        1.10189          H   11 B28 6 A28 1 D28
A31      113.13330          H   12 B29 6 A29 1 D29
D31      267.36043          H   12 B30 6 A30 1 D30
B32        1.09043          H   12 B31 6 A31 1 D31
A32      109.01522          H   13 B32 3 A32 1 D32
D32       28.09252          H   13 B33 3 A33 1 D33
B33        1.10189          H   13 B34 3 A34 1 D34
A33      113.13330          H   14 B35 3 A35 1 D35
D33      267.36043          H   14 B36 3 A36 1 D36
B34        1.09598          H   14 B37 3 A37 1 D37
A34      110.14664          Variables:
D34      146.75372          B1         1.42885
B35        1.09176          B2         1.37100
A35      109.43810          A2       120.83216
```

B3	1.37101	D20	350.64096
A3	120.83290	B21	1.09461
D3	143.09565	A21	109.42432
B4	1.37101	D21	231.51165
A4	120.83246	B22	1.09482
D4	323.09406	A22	111.49855
B5	1.37100	D22	112.24012
A5	120.83161	B23	1.08815
D5	179.97438	A23	110.17867
B6	1.46066	D23	349.05450
A6	122.44700	B24	1.09473
D6	324.46557	A24	111.93484
B7	1.46298	D24	110.48853
A7	122.22829	B25	1.09423
D7	143.34459	A25	109.10895
B8	1.46066	D25	229.95243
A8	122.44737	B26	1.08780
D8	324.46204	A26	110.38638
B9	1.46298	D26	350.65207
A9	122.22813	B27	1.09459
D9	143.34124	A27	109.41718
B10	1.46081	D27	231.52655
A10	122.44184	B28	1.09479
D10	324.43570	A28	111.49564
B11	1.46292	D28	112.25522
A11	122.23073	B29	1.08817
D11	143.35110	A29	110.18024
B12	1.46292	D29	349.03965
A12	122.23057	B30	1.09473
D12	143.34855	A30	111.93693
B13	1.46082	D30	110.46861
A13	122.44220	B31	1.09423
D13	324.43241	A31	109.11188
B14	1.08780	D31	229.94398
A14	110.39198	B32	1.08817
D14	350.64167	A32	110.18016
B15	1.09461	D32	349.03922
A15	109.42445	B33	1.09423
D15	231.51223	A33	109.11192
B16	1.09482	D33	229.94356
A16	111.49841	B34	1.09473
D16	112.24059	A34	111.93689
B17	1.08815	D34	110.46822
A17	110.17880	B35	1.08780
D17	349.05461	A35	110.38662
B18	1.09473	D35	350.65202
A18	111.93496	B36	1.09479
D18	110.48868	A36	111.49560
B19	1.09424	D36	112.25533
A19	109.10892	B37	1.09459
D19	229.95247	A37	109.41699
B20	1.08780	D37	231.52648
A20	110.39207		

```
TDAE Dication                      D5        179.97438
B3LYP/6-311+G*                     B6          1.47992
                                   A6        122.52523
C                                  D6        340.13719
C    1 B1                          B7          1.48156
N    1 B2 2 A2                     A7        124.31352
N    2 B3 1 A3 3 D3                D7        157.29159
N    2 B4 1 A4 3 D4                B8          1.47992
N    1 B5 2 A5 3 D5                A8        122.52528
C    5 B6 2 A6 1 D6                D8        340.13724
C    5 B7 2 A7 1 D7                B9          1.48156
C    4 B8 2 A8 1 D8                A9        124.31353
C    4 B9 2 A9 1 D9                D9        157.29159
C    6 B10 1 A10 2 D10             B10         1.47992
C    6 B11 1 A11 2 D11             A10       122.52524
C    3 B12 1 A12 2 D12             D10       340.13737
C    3 B13 1 A13 2 D13             B11         1.48156
H    7 B14 5 A14 2 D14             A11       124.31345
H    7 B15 5 A15 2 D15             D11       157.29218
H    7 B16 5 A16 2 D16             B12         1.48156
H    8 B17 5 A17 2 D17             A12       124.31331
H    8 B18 5 A18 2 D18             D12       157.29204
H    8 B19 5 A19 2 D19             B13         1.47992
H    9 B20 4 A20 2 D20             A13       122.52534
H    9 B21 4 A21 2 D21             D13       340.13723
H    9 B22 4 A22 2 D22             B14         1.08702
H    10 B23 4 A23 2 D23            A14       111.68415
H    10 B24 4 A24 2 D24            D14       350.57329
H    10 B25 4 A25 2 D25            B15         1.09176
H    11 B26 6 A26 1 D26            A15       108.32808
H    11 B27 6 A27 1 D27            D15       231.53379
H    11 B28 6 A28 1 D28            B16         1.09160
H    12 B29 6 A29 1 D29            A16       109.90152
H    12 B30 6 A30 1 D30            D16       112.96237
H    12 B31 6 A31 1 D31            B17         1.08590
H    13 B32 3 A32 1 D32            A17       110.80049
H    13 B33 3 A33 1 D33            D17       340.63238
H    13 B34 3 A34 1 D34            B18         1.09095
H    14 B35 3 A35 1 D35            A18       111.58741
H    14 B36 3 A36 1 D36            D18       104.10513
H    14 B37 3 A37 1 D37            B19         1.09097
Variables:                        A19       106.97729
B1          1.53406               D19       222.48059
B2          1.32933               B20         1.08702
A2        117.11791               A20       111.68410
B3          1.32933               D20       350.57317
A3        117.11776               B21         1.09176
D3        112.06474               A21       108.32803
B4          1.32933               D21       231.53370
A4        117.11769               B22         1.09160
D4        292.06471               A22       109.90153
B5          1.32933               D22       112.96232
A5        117.11785               B23         1.08590
```

149

A23	110.80041	D31	222.48094
D23	340.63236	B32	1.08590
B24	1.09095	A32	110.80051
A24	111.58745	D32	340.63271
D24	104.10510	B33	1.09097
B25	1.09097	A33	106.97733
A25	106.97736	D33	222.48086
D25	222.48061	B34	1.09095
B26	1.08702	A34	111.58725
A26	111.68403	D34	104.10531
D26	350.57391	B35	1.08702
B27	1.09176	A35	111.68406
A27	108.32801	D35	350.57380
D27	231.53446	B36	1.09160
B28	1.09160	A36	109.90163
A28	109.90160	D36	112.96301
D28	112.96308	B37	1.09176
B29	1.08590	A37	108.32801
A29	110.80047	D37	231.53434
D29	340.63282		
B30	1.09095		
A30	111.58735		
D30	104.10540		
B31	1.09097		
A31	106.97742		

Vita

Byron Smith was born in Roanoke, Virginia on May 19, 1987. He attended public high school in Blacksburg, Virginia and graduated in 2005. He went on to graduate from the University of Toronto with an Honours Bachelor of Science in Physics (Condensed Matter). Byron then chose to pursue a PhD in Chemical Physics and Master's Degree in Statistics under the guide of Dr. Robert Compton. The doctoral degree was recieved December 2013.